

**Theoretical analysis, design and fabrication of supermirrors for
hard X-ray telescopes**

Youwei Yao

Ux Lab, Nagoya University

Contents

1	Introduction	1
1.1	X-ray observation with telescopes	1
1.2	Soft X-ray telescopes	5
1.3	Hard X-ray telescopes with multilayer coating	14
2	Theoretical study of the X-ray multilayer	20
2.1	Basic principles	20
2.1.1	Calculation of the reflectivity -- Parratt's recurrence	20
2.1.2	Interfacial roughness	23
2.1.3	Design of a multilayer structure	24
2.1.3.1	Block structure supermirror (K. Yamashita's concept).....	24
2.1.3.2	Power law structure supermirror (K. Joenson's empirical equation) ..	27
2.1.3.3	Depth graded structure supermirror (Igor's theory).....	29
2.2	Theoretical study of the block structure supermirror.....	35
2.2.1	Simplification of Igor's theory.....	35
2.2.2	Theoretical analysis of the periodical multilayer.....	37
2.2.3	Theoretical analysis of the combined blocks.....	45
2.3	Applications of the simplified Igor's theory	50
2.3.1	Design of the Block structure supermirrors.....	50
2.3.1.1	Design rules and advantage of present theoretical approach	50
2.3.1.2	Relationships with the empirical rules of block-structure	55
2.3.2	Design of the side lobe suppressed multilayer mirrors	56
2.3.2.1	Relations between Window function and side lobes.....	56
2.3.2.2	Gaussian distribution to suppress side lobes of reflectivity profile	58
3	Numerical design of the Supermirrors	62
3.1	Introduction – Goal of the design	62
3.2	Basic principles of the optimization processes	64
3.2.1	Optimization strategy	64
3.2.2	Merit function.....	65

3.2.3	Optimization Algorithm	66
3.2.3.1	Obtaining initial structure (Simplex algorithm).....	66
3.2.3.2	Reducing the ripples (Pattern Search algorithm)	73
3.3	Design examples.....	80
3.3.1	Broaden angular bandwidth supermirror.....	80
3.3.2	Broaden energy bandwidth supermirror.....	82
3.4	Comparison between presented design and previous design	87
4	Fabrication of the supermirror structures	89
4.1	Fabrication processes.....	89
4.1.1	Deposition system	89
4.1.2	X-ray measurement system.....	91
4.1.3	Calibration and thickness controlling	93
4.2	Fabrication and testing results	97
4.2.1	Broad angular bandwidth supermirror.....	97
4.2.2	Broad energy bandwidth supermirror.....	101
4.2.3	Side lobe suppressed multilayer mirror	105
5	Discussion and Summary	107
5.1	Summary of results.....	107
5.2	Re-construction of layered structure	108
5.3	Density issue.....	113
5.4	Future work	116
6	Appendices	118
6.1	Calculation of reflectivity -- Matrix Algorithm (Abeles matrix formalism).....	118

Chapter 1

Introduction

1.1 X-ray observation with telescopes

For thousands of years, the beautiful sky in a dark night always arouses our curiosities. The constellations rising, and the moon crossing the sky, with their ever changing phases and conjunctions, from everlasting to everlasting question our understanding of the cosmos we live in. As one of the oldest science, the length of the astronomical observation history is as long as that of human history. (The history of astronomical observation is intertwined in the map of human history) In ancient days, the only way to observe the sky was by the naked eyes. Due to the lack of information and technology, the observation method was only confined to the measurement of star position and the determination the calendar, essentially for agriculture. Therefore, human being's understanding of the cosmos system was limited to "geocentric theory". Our knowledge and idea was dominated by such theory for a long time until the era, a great scientist fabricated the first astronomical telescope in the history of human being (1609), and pointed it to the sky. His name is Galileo Galilei. Galileo's telescope is a refracting optical one. Although the magnification was only 30X, it was the first time for the people to acquire the ability to observe various new celestial objects such as the Jupiter's satellites. Since then, the importance of the instrument has been realized. Optical telescopes were developed larger and more dedicated to explore the dark sky and, thus significantly extending the range of our knowledge.

In 1895, Roentgen discovered "X-rays". A lot of work has revealed that the X-rays can be diffracted by a crystal (Von Laue, 1912) and reflected by a polished surface (Compton, 1923) with a very small incident angle ($<1\text{deg}$). Since people realized the reflection with very small angle requires different optics from conventional one, the term "grazing incidence reflection optics" was introduced at that time. In 1948, Baez successfully attempted to focus an X-ray beam by grazing incidence reflection optics, which was the first X-ray imaging system. Just four years later, H. Wolter proposed the use of two-reflection based on conical optics for X-ray microscopes. In 1960, R. Giacconi and B. Rossi proposed the use of grazing incidence focusing optics for X-ray telescopes, which was just two years before they discovered the first extra-solar X-ray source in the sky – Sco-X1, by employing a Geiger counter on a sound rocket flight. This great event has initiated the historical stage of X-ray astronomy. The astronomical observations have been extended to X-ray band. Such innovation definitely revolutionized our view of the Universe. 51 years have passed since Giacconi's work in 1962. A series of X-ray flight missions have been performed as pioneer work to accumulate new knowledge and broaden our understanding, as are listed in Table 1.1. The X-ray astronomy has been grown up as a major astronomical research discipline.

In early days, X-ray observations were restricted to get temporal and spectral behavior of X-ray stars with detectors without imaging capability. The sensitivity of such simple systems was limited by non-X-ray background, so that bright X-ray binaries in our Galaxy were the major targets of UHURU satellite launched in 1970. In order to improve the sensitivity and to obtain spatial information of the diffuse sources, such as supernova remnants and cluster of galaxies, X-ray

telescopes had been developed. Einstein satellite in 1979 was equipped with X-ray telescope for the first time to observe X-ray images. On the focal plane, various imaging detectors and small devices for spectroscopy were placed. It expanded the accessible distance of the Universe toward outside of our Galaxy. X-ray spectroscopy revealed the physics of hot plasmas as hot as 10^7 degrees. However, such X-ray imaging observations were limited below 2-4 keV, because focusing X-ray optics is relatively easier to achieve in soft X-ray band due to the fact that low energy photons can be reflected at larger grazing angles with polished surfaces. The upper bound around 2-4 keV was raised to 10 keV by ASCA satellite with the nested thin foil mirrors innovated by Serlemitsos. The Iron K-line features between 6 and 7 keV were well examined with X-ray CCD camera on the focal point for the first time.

In recent years, researchers have realized that hard X-rays over 10keV from celestial objects may play a crucially important role in diagnosing physical processes in the universe, because hard X-ray emission is mostly produced by high energy phenomena such as synchrotron radiation of high energy particles with magnetic field, or gravitational energy release in the strong gravity of compact objects, such as massive black holes. Moreover, X-rays can penetrate absorbing material around these objects as well as the emission lines of some nucleons may exist in the hard X-ray band, which is critical for diagnosing the physical process. As a well known example, the emission line around 78keV from Ti^{44} is a vital clue for understanding the evolution of Supernova Remnants. Table 1.2 shows the major scientific prospects in hard X-ray band.

In order to understand physical processes mentioned above, hard X-ray telescopes which covering 10-100keV is under development. Since the critical angle of total reflection is in inverse proportion to the energy of incident X-rays, the conventional X-ray mirrors with a polished surface may significantly reduce the throughput of the telescope and is thus no longer applicable. In 1992, F. E. Christensen firstly introduced a mirror with supermirror coating, which revealed an innovation for X-ray telescopes. The supermirror is a layered structure with heavy and light materials with high contrast of optical constants, which can reflect the X-rays by means of Bragg reflection at a selected wave band with fixed grazing angles. Since the grazing angle and corresponding wave band are decided by the thickness distribution of the structures and layer materials, a well designed supermirror can provide a broad response at large grazing angles (~ 0.3 deg), which has never been achieved by a conventional mirror. The first test mirror with supermirror coating was produced and the X-ray image at 30keV was demonstrated. In 2001, the first hard X-ray telescope developed by Nagoya University was installed in a balloon experiment named "InFOCuS", and an X-ray image between 20-40keV was successfully obtained. Since it was a balloon experiment, the telescope could not thoroughly be prevented from the X-ray absorption by the atmosphere. Therefore, the multilayer is designed for the energy band from 20keV to 40keV with the maximum grazing angle of 0.35deg. The experiment successfully proved that supermirror is a very efficient way to enhance the telescope performance toward hard X-rays. About a year ago, "Nustar" telescope, the first hard X-ray telescope on board a satellite and equipped with full-bandwidth supermirror (1-80keV), was launched to the orbit. The satellite is expected to open up a new window to explore the universe.

In 2015, the Japanese X-ray mission "ASTRO-H" will be launched to the orbit. It will be the second hard X-ray satellite mission in history, with larger collecting area. These are the first two satellite missions of hard X-ray imaging, and then the designing and fabrication still have to be improved significantly, in full understanding of the propagation of E-M waves in the layered structure, in

optimization of the supermirror design and in fabrication of designed structure. In Chapter 2, I review the basic theory and equations of supermirror, and present my theoretical analysis of a block structure supermirror and its applications. In Chapter 3, I introduce a new design method (Numerical Approach) to improve the performance of the supermirror, especially to remove the ripple structure of the reflection profile against incident angles and X-ray energies. In Chapter 4, I present my fabrication method to realize the designed structure, and concluded the critical point which should be concerned. Finally, Chapter 5 gives conclusions and future work.

The theoretical approach described in Chapter 2 is already published in a paper entitled "The theoretical analysis of the hard X-ray block-structure supermirror" YouWei Yao, Hideyo Kunieda*, Yusuke Miyata, Hironori Matsumoto, Optics Express, Vol. 21, Issue 7, pp. 8638-8651 (2013). The new design method and fabrication of flat response supermirror are described in a submitted paper entitled "Design and fabrication of a supermirror with smooth and broad response for hard X - ray telescopes." , by Youwei Yao, Hideyo Kunieda*, Hironori Matsumoto, Keisuke Tamura and Yusuke Miyata, submitted to Applied Optics, Manuscript ID: 190519(2013).

Table 1.1: Important X-ray flight missions since 1962

1962: Discovery by Giacconi et al. of Sco-X1, the first extra-solar X-ray source
1963: Giacconi and Rossi fly the first (small) Wolter I optics to take images of Sun in X-rays
1965: Second flight of a Wolter I focusing optics (Giacconi + Lindsley)
1973: SKYLAB carry onboard two small X-ray optics for the study of the Sun
1978: Einstein, the first satellite with focusing optics entirely dedicated to X-rays
1983: EXOSAT operated (first European mission with X-ray optics aboard)
1990: ROSAT, first All Sky Survey in X-rays by means of a focusing telescope with high imaging capabilities
1993: ASCA, a multilayer focusing telescope with enhanced effective area for spectroscopic purposes
1996: BeppoSAX, a broad-band satellite with Ni electroformed replicated optics
1999: Launch of Chandra, the X-ray telescope with best angular resolution
1999: Launch of XMM-Newton, the X-ray telescope with most Effective Area
2001; Launch of InFOCuS balloon experiments(+2004)
2004: Launch of the Swift satellite devoted to the GRBs investigation (with aboard XRT)
2005: Launch of Suzaku with high throughput optics for enhanced spectroscopy studies with bolometers
2012: Launch of NuStar, the first satellite with hard X-ray optics based on multilayer coatings
2015: Launch schedule of ASTRO-H

Table 1.2: Scientific problem at 10-80keV

Cluster of Galaxies	Determine the distribution of darkmatter, investigate the origin and strength of the magnetic field inside the cluster, learn the distribution of relativistic particles, and non-thermal processes
----------------------------	---

44Ti nuclear lines in young SNR	Test the current models of both explosive nuclei synthesis and the dynamics of SN eject, investigate the exploration of other recent optically obscured SN
Galactic black holes	Looking for black hole candidates, investigate the hard X-ray properties of neutron stars and the hard X-ray tail from X-ray binaries
Cosmic ray acceleration in young SNR	Indicate the synchrotron emission from accelerated electrons
Intergalactic magnetic fields	Investigate the kinematics of AGN jets, learn the inter-galactic cosmic ray propagation, determine the structure and the evolution of classical double radio sources
Cyclotron lines	Investigate the distribution of both the strong magnetic field and accretion on X-ray pulsars
The diffuse background	Determine the origin of the bump in the hard X-ray background by direct imaging of faint AGN
Pulsar nebulae	Study how the pulsar powers the nebula
Sunyaev-Zeldovich effect	Present microwave measurements predict cluster temperatures of $\sim 15\text{keV}$, needs hard response to check
Unpredicted new discoveries	

1.2 Soft X-ray telescopes

In X-ray band, the optical constants of all the materials are close to 1, which are very different from that in optical band. Therefore, it's difficult to focus the X-rays by refractive lens with large aperture. The basic principle of this phenomenon is described as follows.

We begin from Maxwell's equation to solve the E-M wave propagating in a material:

$$\nabla \times H = \frac{\partial D}{\partial t} + J \quad (1.1)$$

$$\nabla \times E = -\frac{\partial B}{\partial t} \quad (1.2)$$

$$\nabla \cdot B = 0 \quad (1.3)$$

$$\nabla \cdot D = \rho \quad (1.4)$$

Where Eq. 1.1 is Ampère's law. H is magnetizing field. D is displacement field. J is current density. Eq. 1.2 is Faraday's law. E is electric field and B is magnetic field. Eq. 1.3 is Gauss's law for magnetism. Eq. 1.4 is Gauss's law. ρ is charge density of a material. We assume that no polarization exist there. Therefore,

$$D = \epsilon_0 E \quad (1.5)$$

$$B = \mu_0 H \quad (1.6)$$

We apply the equation

$$\nabla \times \nabla \times A = \nabla(\nabla \cdot A) - \nabla^2 A \quad (1.7)$$

to Faraday's law, then

$$\nabla \times (\nabla \times E) = \nabla \times \left(-\frac{\partial B}{\partial t}\right) \quad (1.8)$$

$$\nabla(\nabla \cdot E) - \nabla^2 E = -\mu_0 \frac{\partial}{\partial t} (\nabla \times H) \quad (1.9)$$

Apply Eq. 1.1, 1.4, 1.5 and 1.6 to Eq. 1.9, then

$$\nabla\left(\frac{\rho}{\epsilon_0}\right) - \nabla^2 E = -\mu_0 \epsilon_0 \frac{\partial}{\partial t} \left(\frac{\partial E}{\partial t} + \frac{J}{\epsilon_0}\right) \quad (1.10)$$

We assume that no gradient of charge density in the material. Therefore, the equation of E-M wave propagation can be derived as

$$\left(\frac{\partial^2}{\partial t^2} - c^2 \nabla^2\right) E(r, t) = -\frac{1}{\epsilon_0} \frac{\partial J(r, t)}{\partial t} \quad (1.11)$$

In Eq. 1.11, J(r, t) is the current density caused by the electrons which are oscillated by the incident Electrical wave.

Now we consider a single electron in the material. When it is oscillated by E-M wave, the equation of motion can be expressed as follows,

$$m \frac{d^2 x}{dt^2} + m\gamma \frac{dx}{dt} + m\omega_s^2 x = -e(E_i + v \times B_i) \quad (1.12)$$

Here m is the electron mass. X is the position of electron from origin point. γ is the damping factor with is in proportion to the velocity of the electron. ω_s is resonance frequency of a electron. The first term in the left side of the equation means the inertial force. Second term means the damping of the energy and third term means the energy storage. Term in the right side means the Lorentz force. However, the magnetic field of the E-M wave is very weak thus negligible. The motion of the electron may have the same exponential term with E-M wave, therefore Eq. 1.12 can be derived as follows,

$$m(-i\omega)^2 x + m\gamma(-i\omega)x + m\omega_s^2 x = -eE_i \quad (1.13)$$

So the motion of a single electron can be derived as

$$x = \frac{1}{\omega^2 - \omega_s^2 + i\gamma\omega} \frac{eE_i}{m} \quad (1.14)$$

And the velocity is

$$v(r,t) = \frac{e}{m} \frac{1}{(\omega^2 - \omega_s^2) + i\gamma\omega} \frac{\partial E(r,t)}{\partial t} \quad (1.15)$$

In a material, there is a relationship between the current density and the velocity of the electrons,

$$J_0(r,t) = -en_a \sum_s g_s v_s(r,t) \quad (1.16)$$

Where n_a is the number of atom per unit volume. g_s denote the forced oscillation strengths of the electrons of each single atom. Then,

$$J_0(r,t) = -\frac{e^2 n_a}{m} \sum_s \frac{g_s}{(\omega^2 - \omega_s^2) + i\gamma\omega} \frac{\partial E(r,t)}{\partial t} \quad (1.17)$$

Apply the Equation above to Eq. 1.11. Therefore,

$$\left[\left(1 - \frac{e^2 n_a}{\epsilon_0 m} \sum_s \frac{g_s}{(\omega^2 - \omega_s^2) + i\gamma\omega} \right) \frac{\partial^2}{\partial t^2} - c^2 \nabla^2 \right] E(r,t) = 0 \quad (1.18)$$

It's the conventional form of Helmholtz equation. When the E-M wave propagating in a material, the phase velocity changes due to the forced oscillation of the electrons. The optical constant, as the times of the light speed in vacuum, is written as follows.

$$n(\omega) = \left[1 - \frac{e^2 n_a}{\epsilon_0 m} \sum_s \frac{g_s}{(\omega^2 - \omega_s^2) + i\gamma\omega} \right]^{1/2} \quad (1.19)$$

In X-ray band, the frequency of the X-rays is much higher than the resonance frequency of electrons of all the materials. Therefore, the optical constants in X-ray band are very close to 1.

Note that Eq. 1.19 can be written as

$$n(\omega) = 1 - \frac{1}{2} \frac{e^2 n_a}{\epsilon_0 m} \sum_s \frac{g_s}{(\omega^2 - \omega_s^2) + i\gamma\omega} \quad (1.20)$$

And introduce the classical electron radius, $r_e = \frac{e^2}{4\pi\epsilon_0 mc^2} = 2.8 \times 10^{-15} m$, then

$$n(\omega) = 1 - \frac{n_a r_e \lambda^2}{2\pi} [f_1^0(\omega) - i f_2^0(\omega)] \quad (1.21)$$

$$f^0(\omega) = \sum_s \frac{g_s \omega^2}{\omega^2 - \omega_s^2 + i\gamma\omega} = f_1^0(\omega) - i f_2^0(\omega)$$

It is usually written as following style, varying with incident energy:

$$n(\lambda) = 1 - \delta(\lambda) + i\beta(\lambda) \quad (1.22)$$

$$\delta(\lambda) = \frac{n_a r_e \lambda^2}{2\pi} f_1^0(\lambda)$$

$$\beta(\lambda) = \frac{n_a r_e \lambda^2}{2\pi} f_2^0(\lambda)$$

$\delta(\lambda)$ is essential for the X-ray scattering and $\beta(\lambda)$ is responsible for the absorption.. f_1 is the scattering factor and f_2 is the absorption factor. As an example, following figure shows the optical constant of platinum.

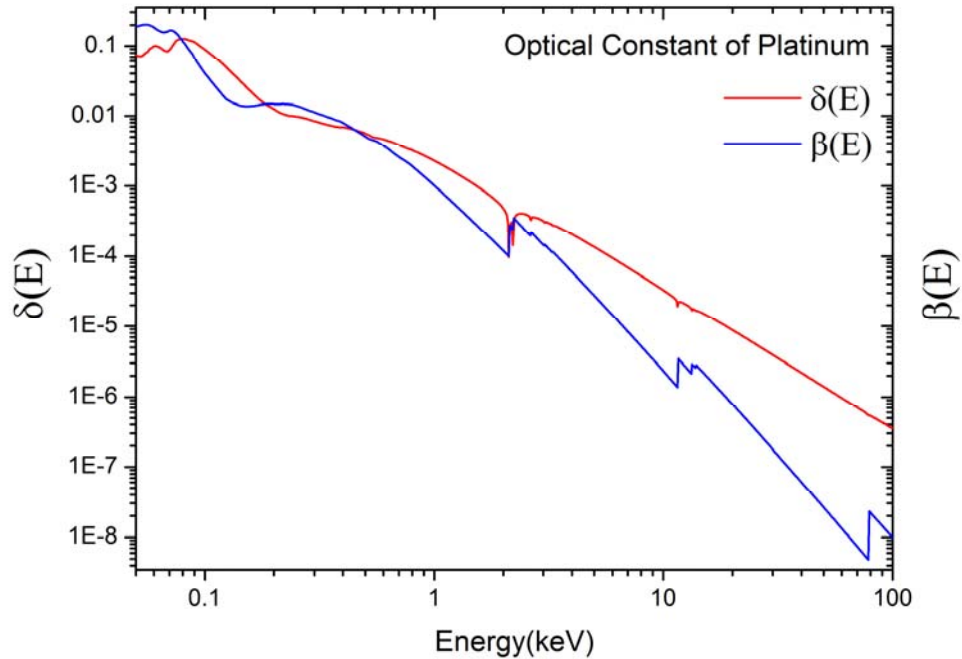


Fig. 1.1 Optical constant of Platinum

Since the optical constant is very close to 1 in X-ray band, the tradition diffraction lens is useless to focus the X-rays. In order to change the propagation direction, a grazing reflection method is under consideration.

The reflection of an incident X-ray transmitted from vacuum to a material is described as follows,

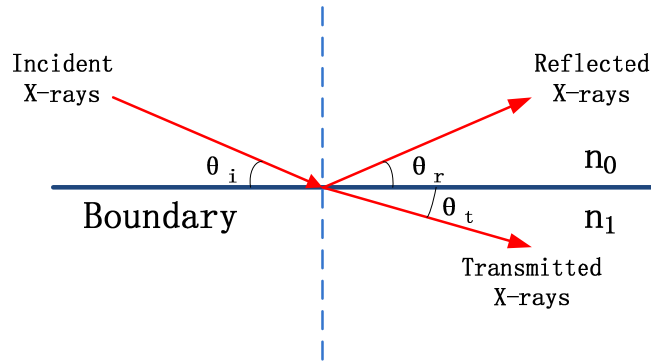


Fig. 1.2 Sketch of X-ray reflection.

The optical constant of all the material is smaller than 1, therefore total reflection phenomenon exists. It can be used to get high reflectivity with small grazing angles. As is described by Snell's law, when the absorption factor is very small, the total reflection grazing angle can be approximated as

$$\cos(\theta_c) = 1 - \delta \quad (1.23)$$

As is described in Eq. 1.19, δ is much smaller than 1 in X-ray band. Hence, equation above can be expressed by Taylor's series.

$$\theta_c \approx \sqrt{2\delta} = \lambda \sqrt{r_e n_a} / \pi \quad (1.24)$$

Therefore, θ_c is inversely proportional to E and proportional to square root of n_a . Subsequently, critical angle decreases quickly with incident energy E , and heavier elements are suitable selections to reflect X-rays. For example, the critical angle of platinum at 8.04keV is approximately 0.6deg, which lead to a 1.2 degrees change of propagation direction.

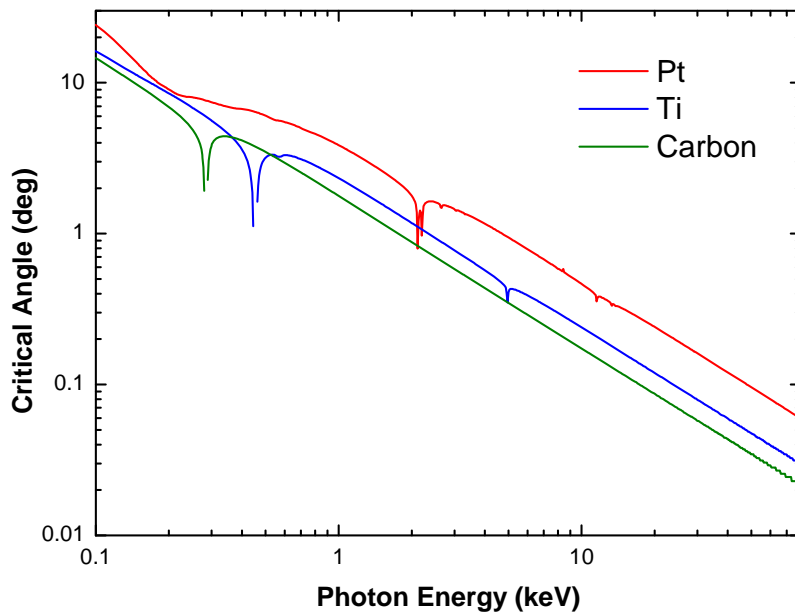


Fig. 1.3 The dependence of the critical angles on X-ray energy for various materials

In 1952, H. Wolter introduced 3 types of optical structures, named as Wolter I, II and III, to focus X-rays by grazing reflection. All of them consist of two mirrors to reflect X-rays with small grazing angles. However, Wolter type I, the combination of a parabolic mirror and hyperbolic mirror, is the most popular for X-ray telescopes application because of its maximum effective collecting area times field of view. The basic structure is shown as follows,

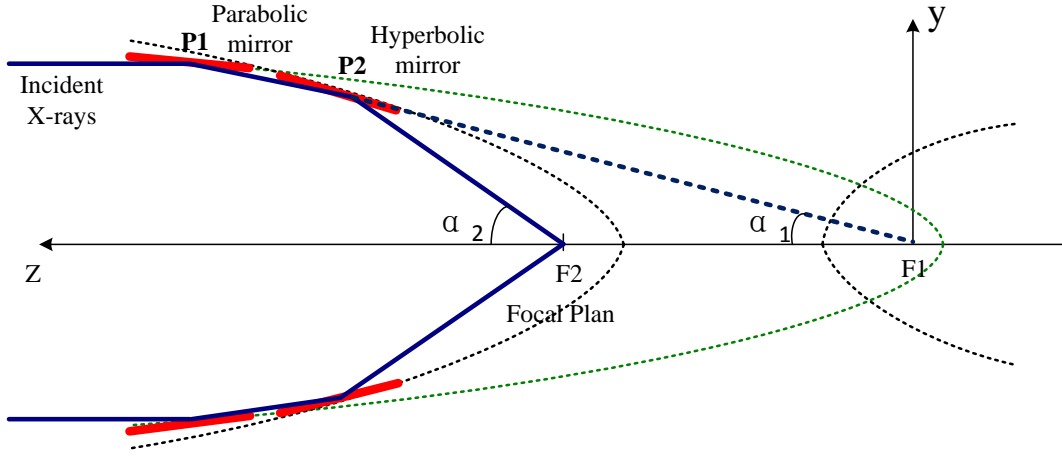


Figure 1.4: Basic structure of Wolter I telescope

The Wolter I optical system consists of a parabolic mirror and a hyperbolic mirror with the same focus F_2 . Incident X-rays reflected by a parabolic mirror (named as primary mirror) at $P_1(x_1, y_1, z_1)$ and propagating direction changes toward focal point $F_1(0, 0)$. Then it is reflected by a hyperbolic mirror (named as secondary mirror) at $P_2(x_2, y_2, z_2)$, the propagating direction changes to the focus of the telescope, i.e., F_2 .

The optical system is circularly symmetric with respect to the optical axis. Therefore, the astigmatism and spherical aberration are eliminated at the focal point. As it is equivalent in optical performance in terms of Abbe sine condition ($\sin \alpha_1 / \sin \alpha_2 = \text{const}$ in this case). It is proved as follows.

For the parabolic curve, shown in Fig. 1.4, a property exists,

$$P = F_1 P_1 - Z_1 \quad (1.25)$$

Where P is a parameter of the parabolic curve.

For the hyperbolic curve, a similar property is

$$2a = F_1 P_2 - F_2 P_1 \quad (1.26)$$

Where a is a parameter of hyperbolic curve.

From Eq. 1.25 and 1.26,

$$\sin \alpha_1 = \frac{y_1}{F_1 P_1} = \frac{y_1}{P + Z_1} \quad \sin \alpha_2 = \frac{y_2}{F_2 P_2} \quad (1.27)$$

And

$$F_1 P_2 = \frac{y_2}{\sin \alpha_1} = \frac{y_2}{y_1} (P + Z_1) \quad (1.28)$$

Therefore,

$$2a = \frac{y_2}{y_1}(P + Z_1) - \frac{y_2}{\sin \alpha_2} \quad (1.29)$$

Thus,

$$\sin \alpha_2 = \frac{y_1}{Z_1 + P - 2a \frac{Z_1}{Z_2}} \quad (1.30)$$

From equations above, we can conclude that

$$\frac{\sin \alpha_1}{\sin \alpha_2} = 1 - \frac{2a}{Z_2} \frac{Z_1}{Z_1 + P} = 1 - \frac{2a}{Z_2 / Z_1} \frac{1}{1 + P / Z_1} \quad (1.31)$$

In our application, the mirror length is much shorter than the focal length. And two reflection points are very close with each other. Therefore,

$$\frac{\sin \alpha_1}{\sin \alpha_2} = 1 - \frac{2a}{Z_2 / Z_1} \frac{1}{1 + P / Z_1} \approx 1 - a = \text{const} \quad (1.32)$$

The Wolter I optical system satisfied the Abbe sine condition and it's appropriate to be used as telescope application.

From Fig. 1.4, it can be easily derived that the relationship between incident angle (θ), radius of telescope (r) and focal length (FL) is expressed as follows,

$$\tan(4\theta) \sim r / FL \quad (1.33)$$

When the FL is fixed, the radius of the telescope is decided by the largest grazing angle. In Eq. 1.24, the grazing angle cannot be larger than the critical angle, which is determined by the optical constant of the material on the surface of the mirror. For example if the coating material is Platinum, then the critical angle at 8.04keV is approximately 0.6deg. In our case, the focal length is determined by the carrier, which is about 4.5 meter for example. Then radius of the telescope is limited at 0.189 meter.

The throughput of the telescope (i.e., Effective Area) is directly related to the radius, which is one of the most important performances due to its direct relations with the ability to collect the photons from celestial objects. In order to enhance this performance, usually a heavy element material is carefully selected and coated on the surface of the mirrors, as is shown in following figure.

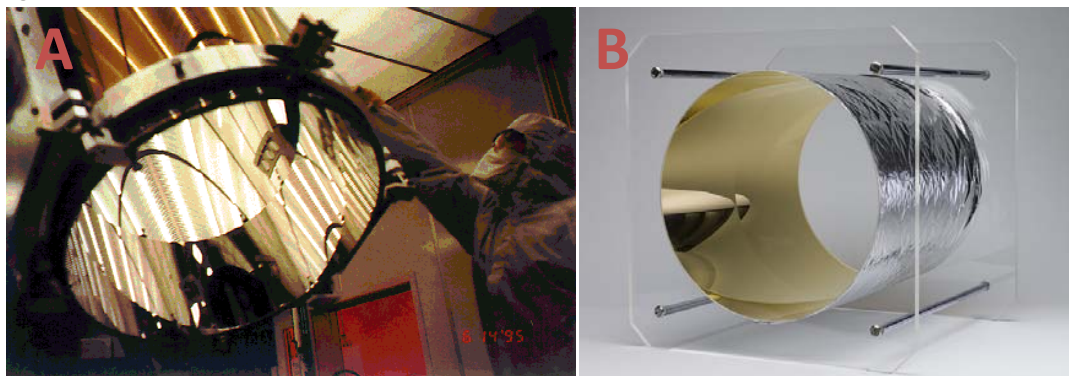


Fig. 1.5, Two types of telescope mirrors coated with Hi-Z material (Iridium(L) Gold(R))

(left Images from websites "http://chandra.harvard.edu/about/telescope_system.html")

(Right Image from [Science Museum London](#))

Panel A shows the mirrors of Chandra telescope. It is a polished glass mirror with Iridium coating on the surface. The advantage of this mirror is extremely good surface quality, which may significantly enhance the image quality. Panel B shows the mirror of XMM-NEWTON mission. It is a Nickel mirror fabricated by electrical forming technology, also coated with Au. The advantage of this mirror is relatively better surface profile.

Once the surface is coated by a material, the reflectivity can be calculated by Snell's law. It is derived from the boundary condition of two materials, and is expressed as following equation,

$$r_s = \frac{n_1 \cos \theta_1 - n_2 \cos \theta_2}{n_1 \cos \theta_1 + n_2 \cos \theta_2} \quad (1.34)$$

$$r_p = \frac{n_2 \cos \theta_1 - n_1 \cos \theta_2}{n_1 \cos \theta_1 + n_2 \cos \theta_2} \quad (1.35)$$

Where r_s and r_p correspond to the amplitude reflectivity of S-polar and P-polar X-rays. Therefore, the intensity reflectivity is equal to

$$R = \frac{1}{2}(r_s \cdot r_s^* + r_p \cdot r_p^*) \quad (1.36)$$

Typically we assume a 100nm Au layer on the surface of mirror shell. Then the response profile with different grazing angle is shown as follows,

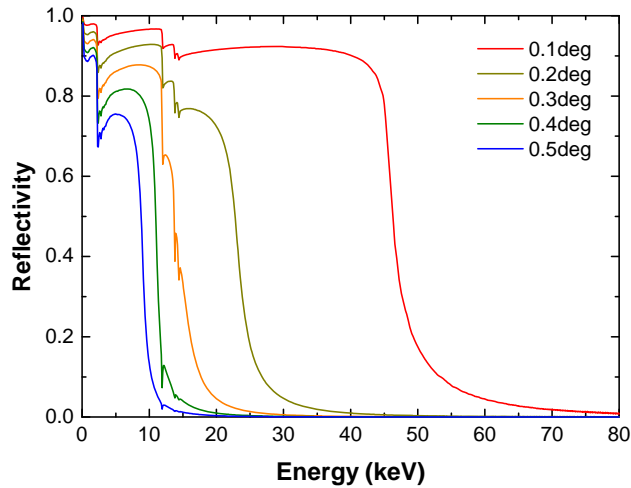


Fig. 1.6 Energy response profile of a single layer with different grazing angles

Since the material coated on the surface is restricted by the coating technology and material properties, the density of the material cannot be endlessly increasing. The radius is restricted due to the optical constant in X-ray band.

In order to get higher effective area, a nested structure was introduced. The basic idea is manufacturing mirror shells with different radius, shell by shell, and mounting them with the same optical axis and focus.

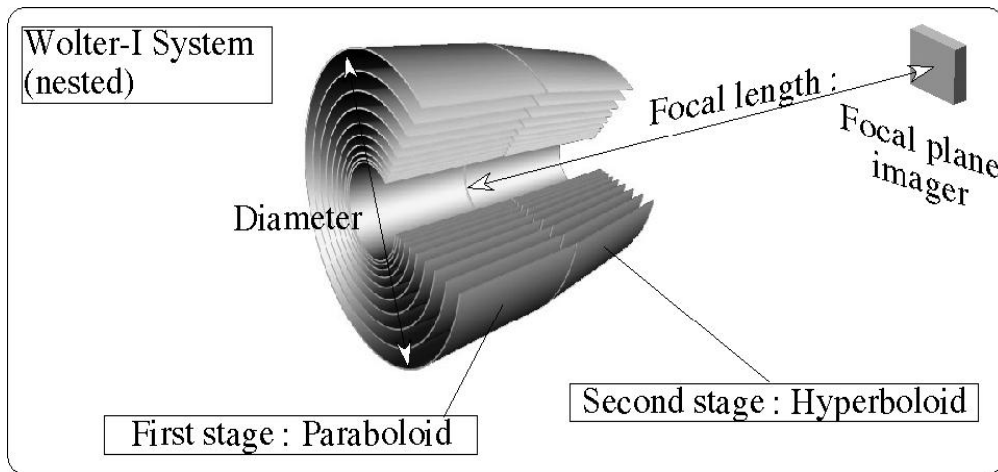


Fig. 1.7. Nested structure of wolter-I telescope system

(Cited from “Design and fabrication of multi-foil hard X-ray telescope for space observations”, Yasushi Ogasaka et al. Proc. SPIE, **5962**, 543-550).

As is shown in the figure above, the Effective Area can be significantly enhanced by employing a nested structure. Since the radius of the telescope is limited by the critical angle of the coating materials, mirror shells are nested tightly to enhance the effective area as much as possible. Different manufacture technology may lead to different performance of mirror shells such as thickness, surface profile and mass. Therefore, the telescopes are divided into three types in terms of the manufacture technology, which are listed as follows.

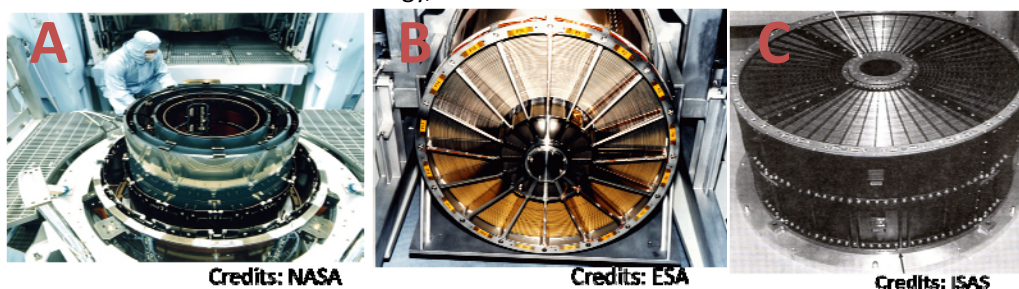


Fig. 1.8 X-ray telescope modules manufactured by different technologies

1. Classical precision optical polishing and grinding mirror

As one of the oldest technology, the optical polished mirror has been applied for many X-ray telescopes, such as Einstein, Rosat and Chandra (shown in Panel A, Fig 1.8). As a matured technology, this technology directly polishes the inner surface of a thick mirror shell. Therefore, it can provide superb surface quality and angular resolution (Chandra: 0.5 arcsec). However, in order to keep the best quality of the surface, the mirror shell is very thick. Subsequently the number of nested mirror shell in one telescope module is low, which may lead to a very low throughput. Moreover, the mass of mirror shell is large, with very high cost.

2. Electric-forming replicate mirror

The electric forming technology is mainly developed for European X-ray mission such as EXOSAT, SAX, JET-X/Swift, XMM-Newton, ABRIXAS, e-Rosita and ART-X.

In order to fabricate thin mirror shells with good surface quality, researchers firstly polish the outer surface of a conical mandrel with respect to the requirement of a telescope. Secondly, an optical layer is coated on the surface of the mandrel (Usually Au layer). Thirdly, a uniform Nickel

layer is deposited on the optical layer by means of electrical forming technology. Finally, due to the fact that the combination between the optical layer and mandrel is weak, the electrical formed mirror with optical layer can be easily released from the mandrel. Panel B in Fig. 1.5 shows a released Nickel mirror with Au coating. Panel B in Fig 1.8 shows the XMM-Newton telescope module nested with Nickel mirrors.

There are several advantages for the Nickel mirror. Firstly, the fabricated mirror shell is much thinner than a classical polished one, which means a highly nested structure can be achieved. Secondly, the surface quality of the mirror shell is enough to satisfy the observation (XMM-Newton: 15-25arcsec). However, there are two drawbacks of this technology. The fabrication process is still expensive. And since Nickel is a very heavy element, the telescope module is very heavy to be sent to the orbit.

3. Thin foil mirror

Since the electrical forming mirror is too heavy and expensive, thin foil mirror is developed to solve these problems.

The basic idea of the fabrication process is to use the light weight substrate instead of the heavy Nickel. Therefore, the electrical forming process has been removed. Epoxy is spread on a coated mandrel. Then, an aluminum foil is bent as the curvature of mirror shell and stick on the mandrel surface. When epoxy cured, the aluminum mirror can be released with the coated layer from the mandrel. Panel C in Fig. 1.8 shows the nested SUZAKU telescope with its foil mirrors as is shown in following figure.

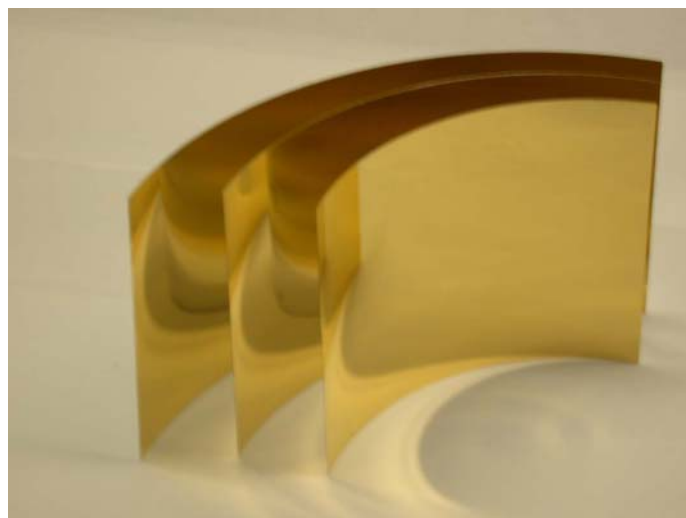


Fig. 1.9 Suzaku's thin foil mirror

The advantage of the thin foil mirror is the lower cost as well as the light weight. It is relatively easier to be sent to the orbit. However, the drawback is significant: the surface profile of mirrors cannot be as good as that of electrical formed one. Subsequently the angular resolution of the telescope module is poor (1-3arcmin)

Obviously, with a fixed weight and cost, there is an inevitable trade-off between the energy resolution and effective area. Fortunately, not only one X-ray telescopes are run in-orbit. This situation may provide an opportunity to observe a celestial object with different emphasis. For example, Chandra may help to locate the position of an object. Then SUZAKU can investigate the spectrum of the X-rays for the located object, especially with an X-ray micro-calorimeter onboard

the satellite.

1.3 Hard X-ray telescopes with multilayer coating

As is discussed in previous sections, hard X-ray band over 10keV becomes more and more important in astronomical observation. Since the higher the X-ray energy the smaller the critical angle, the throughput of the telescope becomes so small in hard X-ray band that is no longer useful to collect photons efficiently. However, the X-ray absorption decreases with the incident energy. Consequently, the penetration depth of X-rays increases in hard X-ray band.

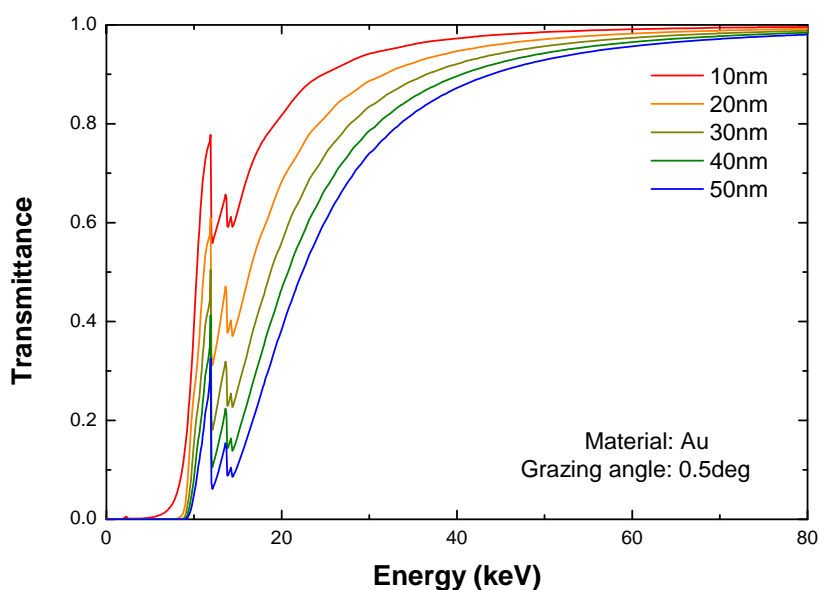


Fig. 1.10 X-ray transmittance of a Gold layer.

As is shown in Fig. 1.10, we assume an X-ray transmitting in a gold film with grazing angle of 0.5deg. If the thickness of gold film is 50nm, the transmittance of X-rays at 40keV is still over 80%. Therefore, a multilayer structure is satisfied to be coated on the surface of mirror shells and enhance the X-ray reflectivity with larger grazing angles and higher incident energy. On the other hand, the geometrical configuration of the telescope employed multilayer is not necessarily modified.

A multilayer is a layered structure which consists of 2 materials and compiled sequentially on a substrate. The basic idea of the multilayer reflection is to reflect X-rays with many inner surfaces instead of one surface of a single layer. Since the lattice plane is parallel with each other, when the thickness of each layer is constant and small enough, the interference of the X-rays reflected by each surfaces cannot be negligible. Bragg reflection may significantly enhance the reflectivity in an energy band with fixed grazing angle due to the fact that the X-rays reflected by all the inner surfaces can be in-phased.

Following figure shows the basic structure of a multilayer. Thickness of layer pair is called "d-spacing". Ratio between the thickness of heavy element layer and d-spacing is named as "Gamma".

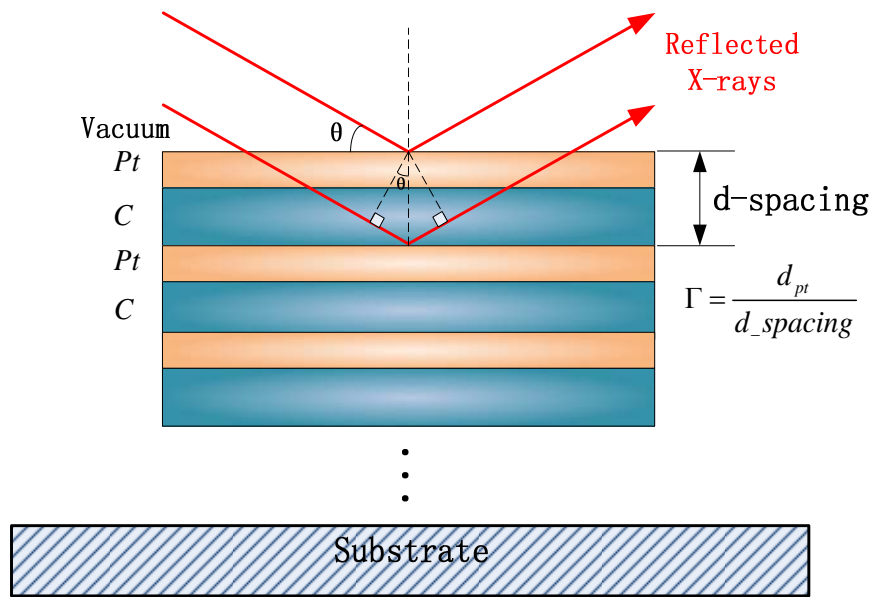


Fig. 1.11 A Pt-C multilayer structure and derivation of Bragg condition

When the grazing angle and d-spacing satisfy a Bragg condition of a designated wavelength

$$2d \sin(\theta_m) \sqrt{1 - \frac{2\delta - \delta^2}{\sin^2(\theta_m)}} = m\lambda \quad (1.37)$$

Reflectivity will be enhanced. For example we assume a Pt-C multilayer with 4nm d-spacing, 0.5 of Gamma, 0.5deg grazing angle and 30 layer pairs, the energy response of reflected X-rays is plotted as follows,

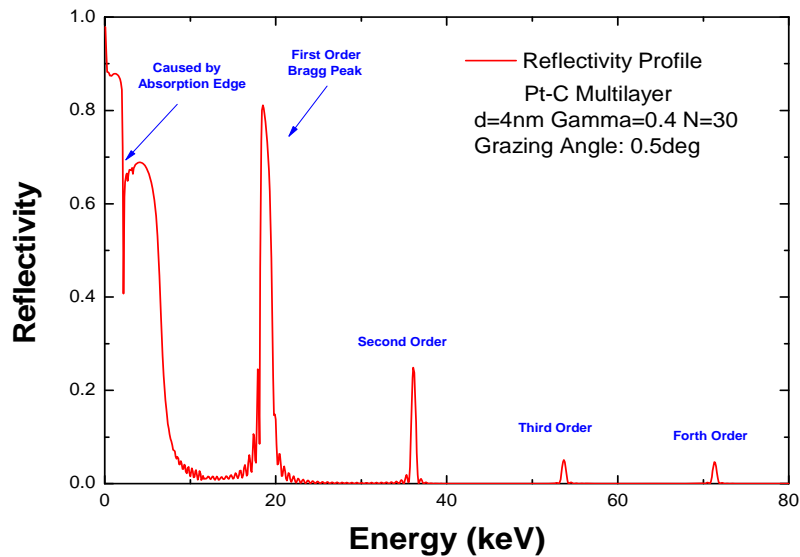


Fig. 1.12 Energy response profile of a Pt-C multilayer

By means of the Bragg reflection, multilayer can gain reasonable reflectivity in hard X-ray band with much larger grazing angle, which can never be achieved by a single layer coating. However, as is shown in Fig. 1.12, band pass of the multilayer response is too narrow (2-3keV for example),

to satisfy the broad bandwidth observation. As we know, the width of the Bragg peak is inversely proportional to the layer number. Reducing the layer pair may somewhat expand the width, but the reflectivity will be sacrificed and is not acceptable.

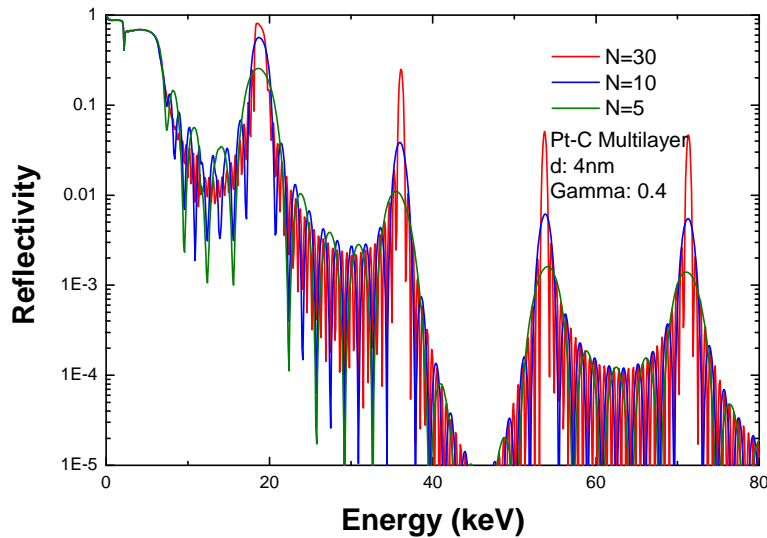


Fig. 1.13 Energy response profiles with different layer pairs

In order to expand the response bandwidth, Supermirror coating has been proposed by several researchers. Supermirror is a depth graded multilayer which means the thickness changes from layers to layers to satisfy Bragg condition at a broaden waveband. There are two kinds of the supermirrors which have been used for hard X-ray telescope and are introduced below.

1. Block structure supermirror

The Block structure supermirror is a layered structure which consists of several periodic multilayer “Blocks”. For each block, the parameters such as d-spacing, Gamma and layer number independently satisfy the Bragg condition at a wavelength. The d-spacing of each block decreases sequentially due to the penetration depth of X-rays at corresponding wavelength. The gap between Bragg peaks is smaller than the width of peaks. Therefore, the energy response profiles of adjacent blocks may overlap with each other, thus cover target bandwidth with “smooth” reflectivity profile.

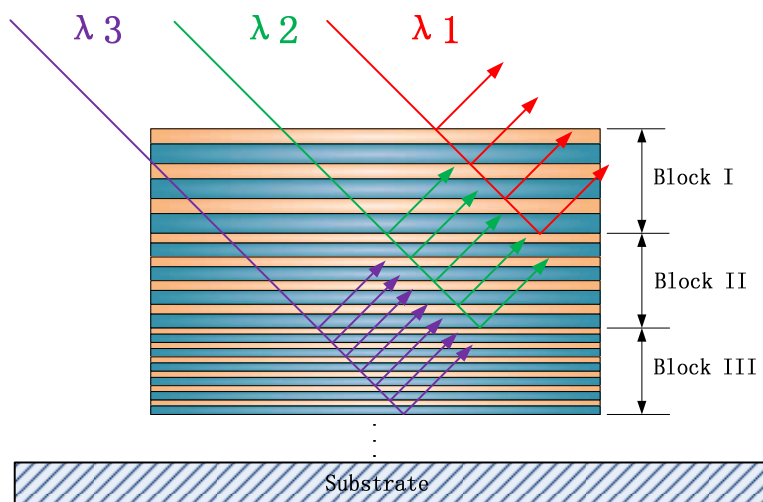


Fig. 1.14 Block structure supermirror

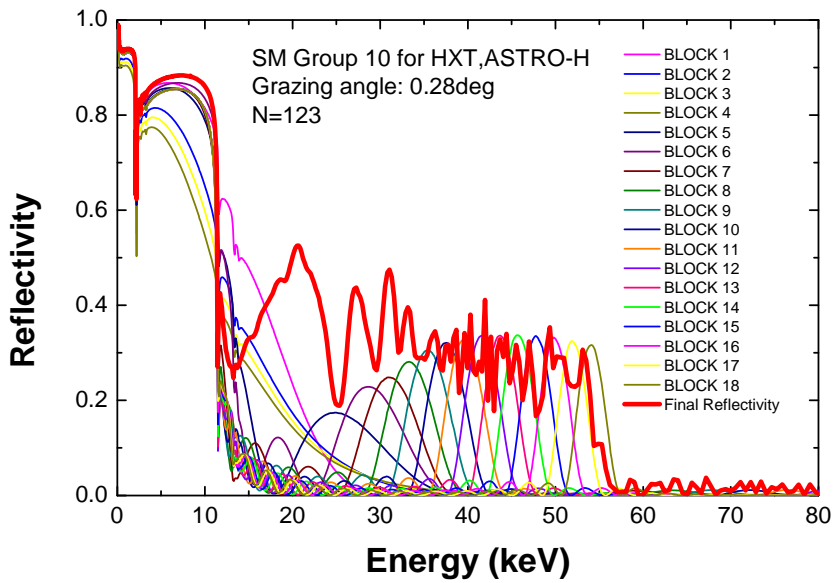


Fig. 1.15 Energy response profile of a block structure supermirror

The block structure supermirror has been successfully applied in “InFOCuS” balloon telescope. It is also applied in ASTRO-H telescope, which is scheduled to launch in 2015.

The advantage of the block supermirror is its convenience in fabrication. Ideally, if we can fabricate very thin films with good thickness precision, then we can gain reasonable reflectivity with very large grazing angle by employing Bragg reflection. However from practical point of view, the lower limit of the layer thickness is about 1nm with ~ 0.05 nm thickness error due to the material property and fabrication process. Actually, a 5% thickness variation may lead to mismatch of response profile. Hence, easy-to-fabricate is extremely important, especially in the case of mass production (over thousands of mirrors for HXT, ASTRO-H). The block structure is quite simple. It’s easy to calibrate the reflectivity profile due to its limited parameters. Hence, easy-to-fabricate is a great advantage of block mirror.

However the disadvantage of this structure is large oscillation of reflectivity profile as well as the connection between the total reflection area and normal reflection area, due to the design problem, which is one of the major topics in following Chapter.

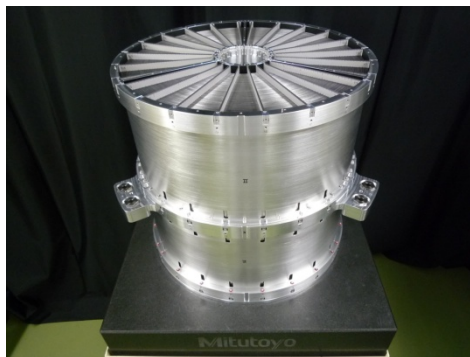
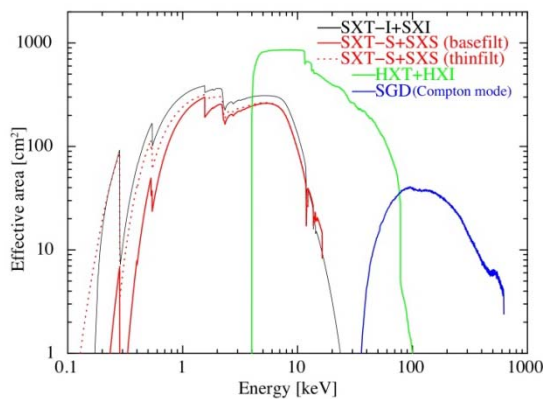


Fig. 1.16 Effective Area of ASTRO-H (left) and its nested mirror HXT module (right).

(From astro-h.isas.jaxa.jp)

2. Power law structure supermirror

The power law structure supermirror is a depth graded layer structure in which the thickness changes gradually from the top to the bottom. Similar with the block structure, the thickness of the layer on the top is thicker than that in the bottom due to the penetration depth of corresponding wavelength of X-rays. Instead of the step-like thickness distribution of Block structure, the distribution of power law structure follows an empirical equation, which is introduced by F. E. Christensen.

$$d_i = \frac{a}{(b+i)^c} \quad (1.38)$$

Where d_i is the thickness of i -th layer pair counted from the top boundary. a , b and c are three parameters which should be optimized by computer algorithm.

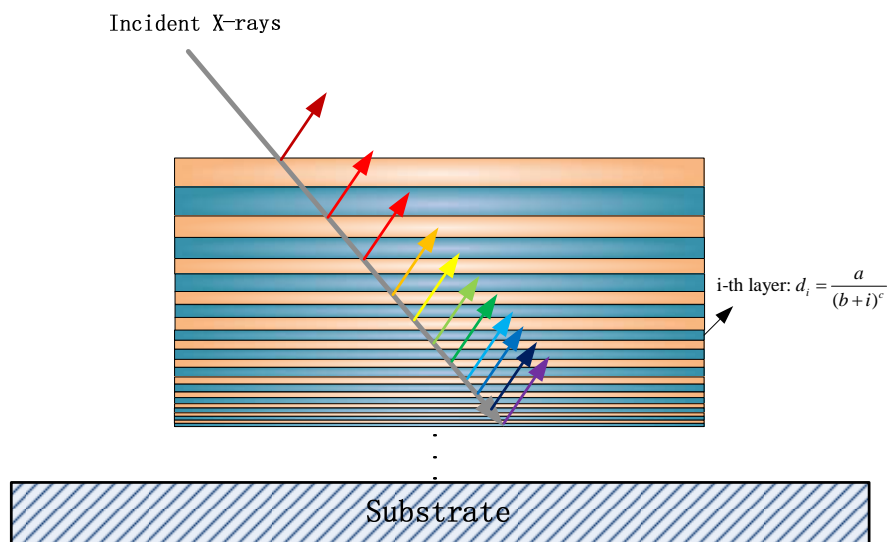


Fig. 1.17 Energy response profile of a power law structure supermirror

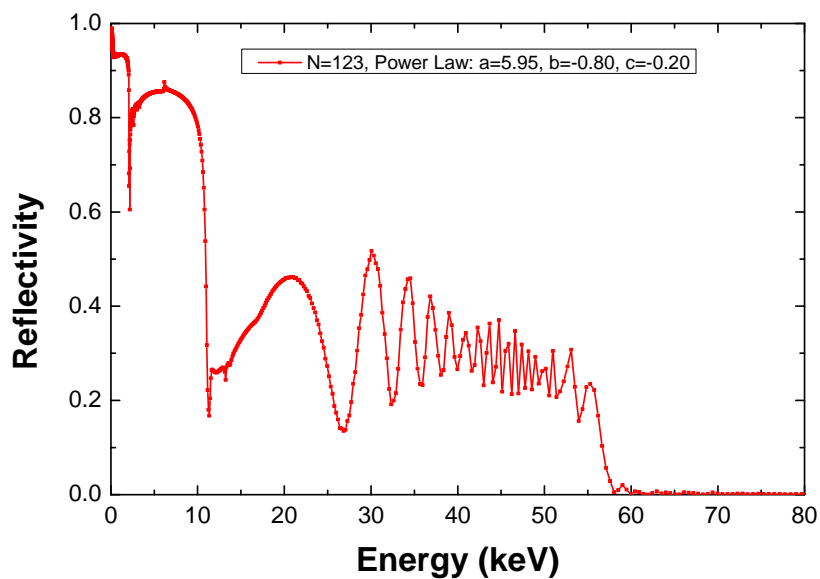


Fig. 1.18 Energy response of a power law structure supermirror

The power law structure supermirror has been successfully applied in NuSTAR mission, a telescope onboard a satellite launched 12 months ago.

Comparing with the block structure mirror, the power law supermirror is easier to design due to the simple empirical equation (Eq. 1.37). The slope of response profile can be easily adjusted following scientific goal by means of computer optimization. However, the structure is relatively difficult to fabricate as block mirror because the difference of adjacent layers is so small. The calibration and diagnosis of fabricated structure is quite a problem.

Fortunately, in telescope module, mirrors are nested to reflect X-rays with different grazing angle. Slight mismatching response profile of a single mirror can be diminished and not affect the final effective area of a telescope, as is shown in following figure.

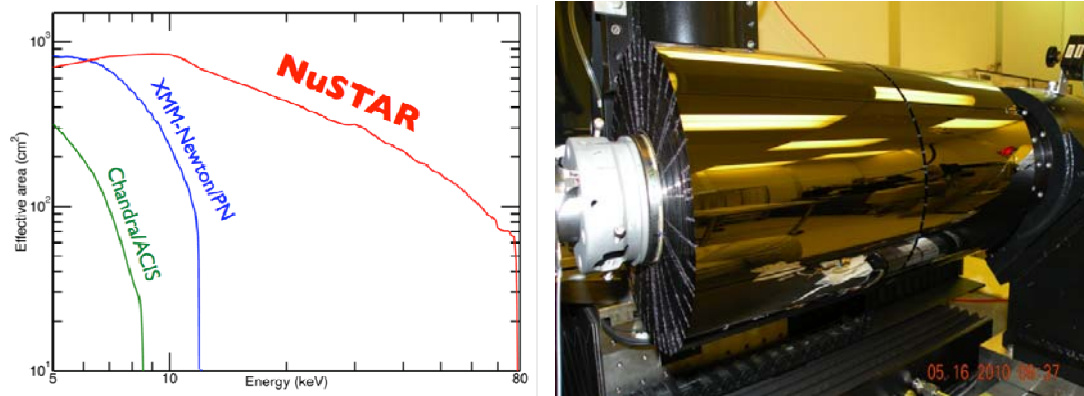


Fig. 1.19 Final Effective Area (left) and nested mirror of NuSTAR telescope (right).

(From NASA.gov)

Chapter 2

Theoretical study of X-ray multilayer

In order to obtain the supermirror design we need, it is necessary to start from the full understanding of the propagation of electro-magnetic waves in the layered structure. The first section will be devoted to the theoretical description of basic processes. In the second section, I introduce our improved (simplified) theory to understand and describe the E-M wave propagation behavior in layered structure. In the last section, we apply our approach to the block structure supermirror to confirm empirical rules derived from previous experiments; InFOCuS and ASTRO-H. It is also applied to design a structure to improve the performance of a multilayer.

2.1 Basic Principles

Propagation of electro-magnetic wave is mathematically described and the reflectivity is calculated with some approximations and considerations of the interfacial roughness. Three types of super mirror designs are introduced and theoretical understandings are described.

2.1.1 Calculation of the reflectivity -- Parratt's recurrence

In 1954, Parratt gives a recurrence method to calculate the reflectivity of a multilayer structure. This calculation method calculates the reflectivity surface by surface, which is easy to be understood. In addition to this method, there's a matrix algorithm to achieve the same purpose, which is very elegant method but relatively complex. Therefore in this section, I introduce the parratt's method. The matrix method is left in appendices.

We firstly consider a single layer reflection

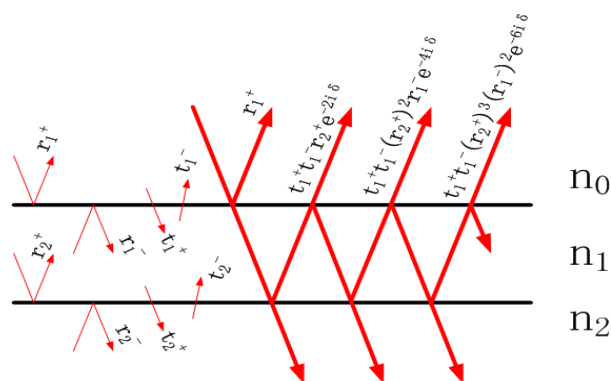


Fig. 2.1 The multi-reflection of a single layer

As is shown in Fig. 2.1, we assume the amplitude reflectivity and transmittance of first surface are r_1 and t_1 , these of second surface are r_2 and t_2 . Consequently the multi-reflectivity of the layer (both surface) can be expressed as

$$\begin{aligned}
r &= r_1^+ + t_1^+ r_2^+ t_1^- e^{-2i\delta} + t_1^+ r_2^+ r_1^- r_2^+ t_1^- e^{-4i\delta} + \dots \\
&= r_1^+ + \frac{t_1^+ r_2^+ t_1^- e^{-2i\delta}}{1 - r_2^+ r_1^- e^{-2i\delta}}
\end{aligned}$$

and

$$\begin{aligned}
r_1^+ &= -r_1^- = r_1, \quad r_2^+ = -r_2^- = r_2, \\
t_1^+ t_1^- &= 1 - r_1^2
\end{aligned}$$

Therefore,

$$\begin{aligned}
r &= \frac{r_1 + r_2 e^{-2i\delta}}{1 + r_1 r_2 e^{-2i\delta}} \\
R &= r \cdot r^*
\end{aligned} \tag{2.1}$$

Here, $\delta = k\sqrt{n^2 - \cos^2(\theta)}d$, which means the phase shift of the X-ray propagate from boundary 1 to boundary 2 and return to boundary 1.

One thing I have to mention is, for X-ray multilayer the high Z material should be a metal, the absorption is not negligible and lead to a complex Fresnel coefficient. Hence, when an X-ray reflected by a boundary, the phase of it should be shifted. And the Eq. 2.1 should be expressed as

$$\begin{aligned}
\tilde{r} &= \frac{\tilde{r}_1 + \tilde{r}_2 e^{-2i\delta}}{1 + \tilde{r}_1 \tilde{r}_2 e^{-2i\delta}} \\
R &= \tilde{r} \cdot \tilde{r}^*
\end{aligned} \tag{2.2}$$

Here \tilde{r} is complex reflectivity of a single layer. When the reflection of a surface is small, i.e., $\tilde{r}_1 \tilde{r}_2 \ll 1$, then Eq. 2.2 can be simplified as "Vector model". (also called kinematical approximation) Then,

$$\tilde{r} = \tilde{r}_1 + \tilde{r}_2 e^{-2i\delta} \tag{2.3}$$

The reflectivity of the single layer \tilde{r} is similar with the sum of Fresnel coefficient with respect to vectors. It is very useful to analyze the X-ray propagation behavior in a complex structure, which will be introduced in following sections.

Now we extend Eq. 2.2 to calculate a multilayer reflection.

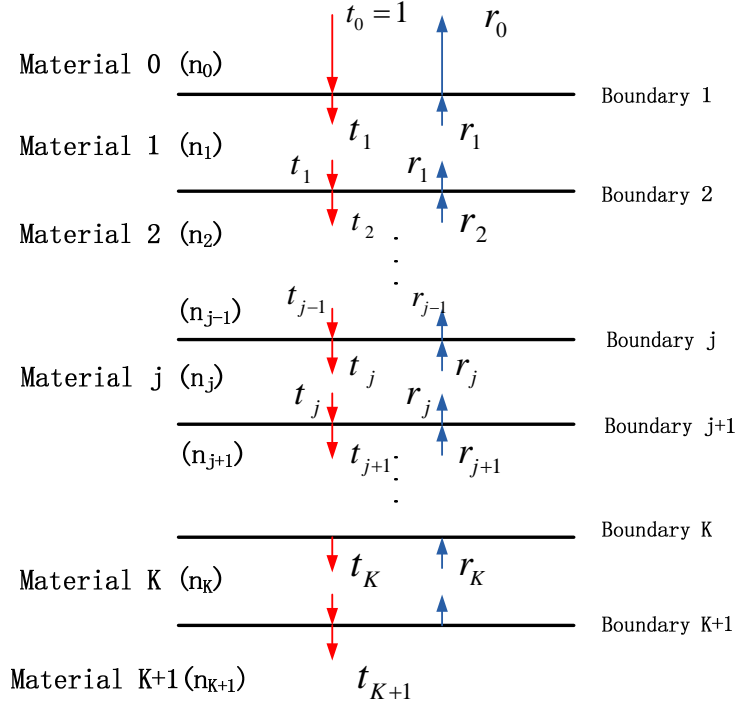


Fig. 2.2 Sketch of K-layer structure with K+1 boundaries.

Fig 2.2 shows a multilayer structure with K layers. At the top of the structure, Material 0 should be vacuum. In the bottom, Material K+1 should be substrate. In this section, we begin from Fresnel's law to calculate the reflectivity of the structure, i.e., r_0 .

We assume that X_j means the amplitude reflectivity of layer system from Boundary K+1 to j +1, Then X_{j-1} means that from Boundary K+1 to j,

$$\tilde{X}_{j-1} = \frac{\tilde{r}_{j-1} + \tilde{X}_j \exp(-2ik_{z,j}d_j)}{1 + \tilde{r}_{j-1}\tilde{X}_j \exp(-2ik_{z,j}d_j)} \quad (2.4)$$

Where $k_{z,j}$ is the normal component of the wave vector propagating in layer j. The expression is

$$k_{z,j} = k\sqrt{n_j^2 - \cos^2(\theta_j)}$$

d_j is the thickness of j-th layer and \tilde{r}_{j-1} is the Fresnel coefficient of interface j,

$$r = \frac{\eta_{j-1} - \eta_j}{\eta_{j-1} + \eta_j} \quad (2.5)$$

Where $\eta_{p,j} = \tilde{n}_j / \cos(\theta_j)$, $\eta_{s,j} = \tilde{n}_j \cos(\theta_j)$

Generally, there is no upper wave in the substrate due to the fact that the penetrate depth is much smaller than the thickness. Consequently $\tilde{X}_{K+1} = 0$ is considered as the start of recursion. The amplitude reflectivity of the whole structure can be obtained from Eq. 2.4, i.e., \tilde{X}_0 . In the following sections, all the reflectivity is calculated by Parratt's recurrence algorithm.

2.1.2 Interfacial roughness

From a practical point of view, the surface and interfaces in the layer structure is not perfect. The atom profile, the thermal vibrations, the diffusion of materials and the surface error can lead to a “rough” surface. For example, diffusion means the mixture of the materials at boundary, thus causes a continuous variation of the refractive index $\tilde{n}(z) \in [\tilde{n}_j, \tilde{n}_{j+1}]$. In addition, the surface error means the position of the surface from the original point follows a distribution for height. Both of them reduce the reflectivity because contributions from different depths within a boundary may add amplitudes with different phases. In this section, due to the fact that an understandable and simple model is needed to calculate the reduction of reflectivity rather than research the roughness itself, we assume all kinds of the surface roughness lead to one result, i.e., the position of X-ray reflection from original point follows Gaussian distribution for height.

$$P(h) = \frac{1}{\sqrt{2\pi}\sigma} \exp\left(-\frac{h^2}{2\sigma^2}\right) \quad (2.6)$$

Where h is the height of reflection point from original surface. σ is defined as root-mean-square roughness. Obviously in Eq. 2.6, the average position of the surface is considered as 0.

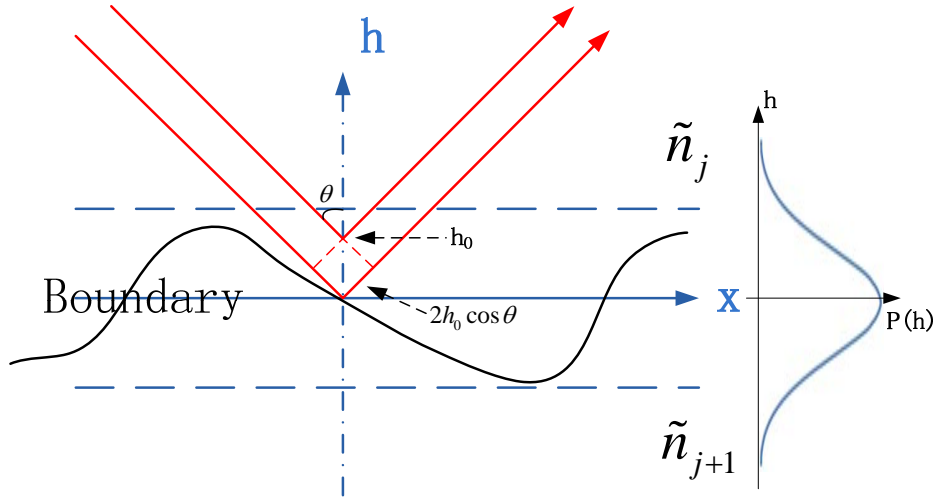


Fig. 2.3 X-ray reflection at a rough interface.

As is shown in figure above, the X-rays reflected by a rough interface. The phase shift can be calculated as a layer reflection. The expression is shown as follows,

$$\begin{aligned} r &= r_j \int P(h) \exp(i2kh \cos \theta) dh \\ &= r_j \int P(h) \exp(i2k_{\perp} h) dh \\ &= r_j \mathcal{F}(P(h)) \end{aligned} \quad (2.7)$$

And the Fourier transformation of the Gaussian distribution is defined as Debye-Waller factor.

$$\mathcal{DW} = \mathcal{F}(P(h)) = \exp\{-2[k \cos(\theta)\sigma]^2\} \quad (2.8)$$

Combine with Eq. 2.5, DW factor has been used to calculate the multilayer reflectivity.

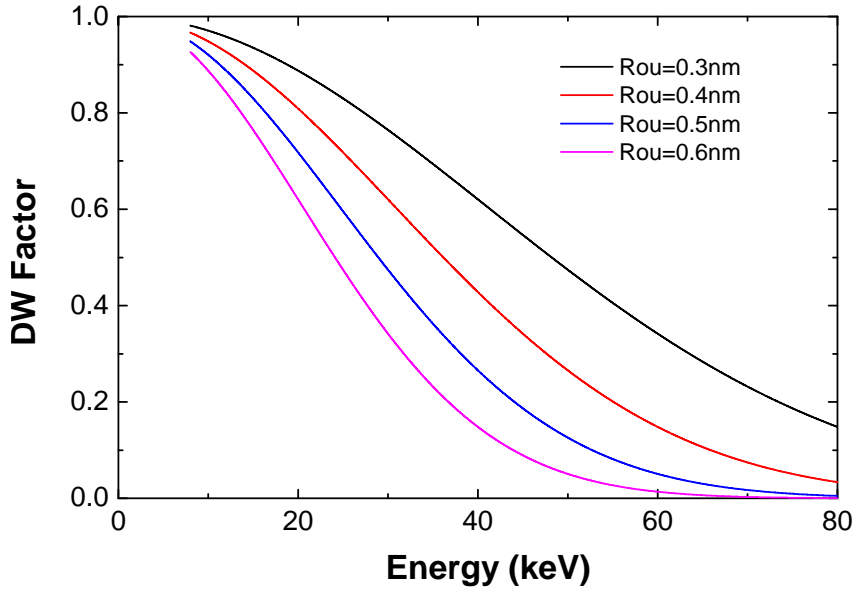


Fig. 2.4 DW factor for interfacial roughness within interest band, with grazing angle 0.3deg

2.1.3 Design of a multilayer structure

Previous sections demonstrated the methods to calculate the reflectivity of a multilayer structure. However, the recurrence method may not be helpful to design a multilayer structure with desired response. Generally, several parameters need to be determined such as d-spacing, Gamma and layer number. In this section, three design methods are illustrated to obtain the structures with desired reflectivity profile.

Prior to the designing section, selection of the materials is important and demonstrated as follows.

We firstly select a spacer material which has the lowest possible absorption, especially K- or L-edge should be avoided for the X-ray energy of interest, 10-80keV as introduced in the first chapter. The selection is quite limited. Carbon is a good candidate for example. The partner of the spacer material should provide a large contrast of the optical constant. In addition, absorption edge should also be carefully prohibited from the interest band. From Fig. 2.4, the interfacial roughness may significantly reduce the reflectivity.

Therefore, the physical and chemical stability and the quality of the interface are extremely important and should be limited below 0.5nm within approximately 200 layer pairs. The pair of the materials is very limited. Eventually Platinum/Carbon multilayer is ideal and selected for our purpose.

2.1.3.1 Block structure supermirror

The block structure, which consists of several blocks of periodical multilayer, is one of the popular structures due to its convenience in fabrication. When designing the structure, the parameters to be determined for each block are d-spacing, number of layer pair and Gamma. Since the response of each block can be calculated by the Parratt's algorithm and displayed directly in the computer in front of designer, usually the parameters are optimized manually with several directions of design rule. Generally, maximization of the integrated reflectivity is the first priority

for astronomical application. The “smoothness” of reflectivity profile is not so important which has been demonstrated in Chapter 1.3. The maximization of the integrated reflectivity can be expressed as follows,

$$MAX(R_{int}) = MAX \int_{E_{min}}^{E_{max}} R(E)dE \quad (2.9)$$

In order to achieve the purpose, the design rules are demonstrated below.

1. Design process should be sequentially from the top to the bottom to confirm the X-rays can penetrate upper blocks and arrive the corresponding block.
2. Thickness of the first layer should be decided by the critical angle.
3. The lowest energy of the X-rays which penetrate the first layer provide the upper limit of d-spacing.
4. For adjacent blocks, the energy gap of corresponding Bragg peak should be constrained as constant firstly. ($\Delta E = const$ i.e., $N_i d_i = constant$)

Layer number of each block should be determined as follows,

We assume an X-ray reflected by a multilayer structure with d-spacing of 3nm, Gamma of 0.4 and perfect interface. The grazing angle is 0.28deg. The reflectivity of first order Bragg peak is calculated and plotted for number of layer pairs N.

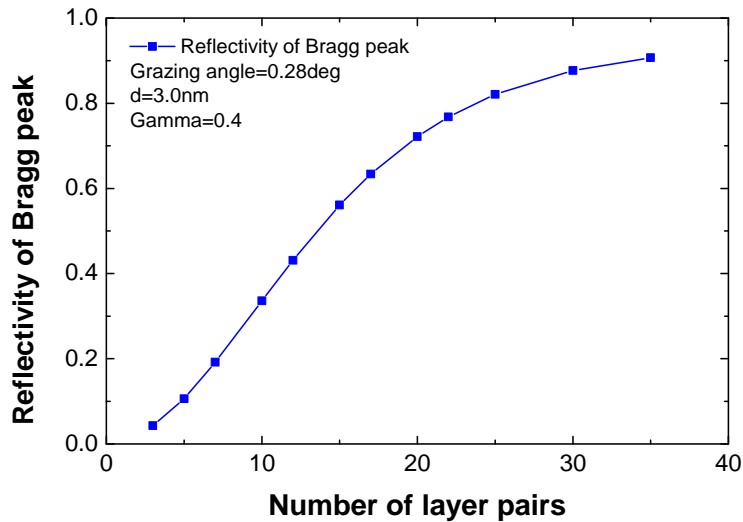


Fig. 2.5 Bragg peak reflectivity v.s. number of layer pairs.

As is shown in figure above, the reflectivity increases rapidly with the number of layer pairs when the layer number is not so large (<20 for example), since the penetrated X-rays can be reflected by the adding layers in the bottom of the structure. However, the reflectivity becomes saturated when the layer number is larger than 20 due to the fact that most of X-rays reflected by the upper layers, less and less X-rays can achieve the bottom. Based on a practical point of view, total layer numbers of a multilayer structure should be limited below 150 to promise an acceptable interfacial roughness (below 0.5nm). In order to maximize the efficiency of all layer pairs in the structure, the layer number of each block should be determined in case of the reflectivity begin to saturate, i.e.,

$$\frac{dR}{dN} \approx \max \quad (2.10)$$

When the number of layer pair and d-spacing of one block are determined, following the rule that $\Delta E = const$ and Eq. 2.10, the layer number can be determined block by block. Here a designed structure is given as an example. One thing I have to mention is that the designed structure may not seriously follow the design rules, since the parameters optimized manually, it is flexible to achieve the reflectivity profile satisfying the scientific goal.

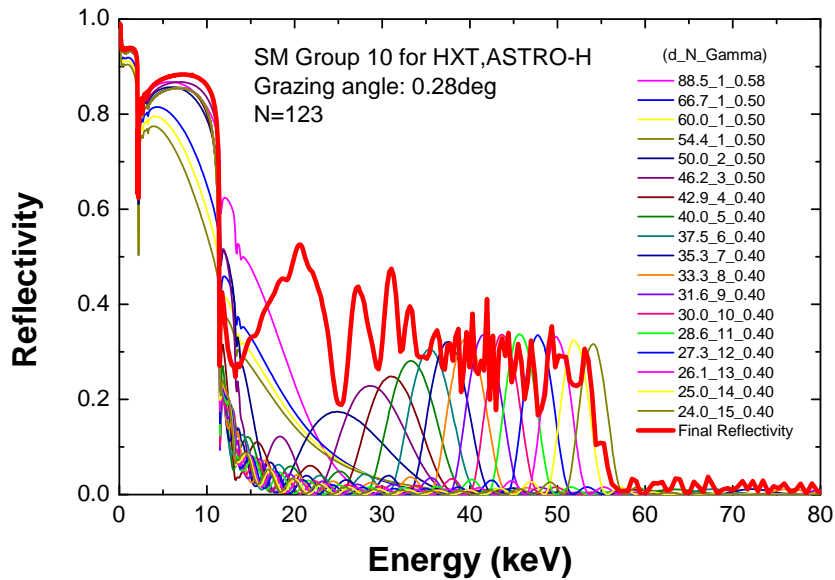


Fig. 2.6. An example of designed block structure supermirror-SM Group 10

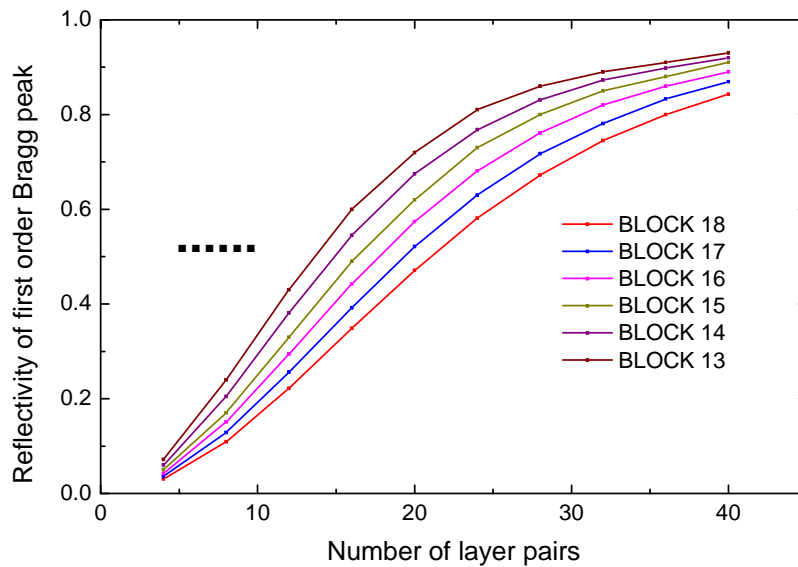


Fig. 2.7 Reflectivity of first order Bragg peak v.s. Number of layer pairs

2.1.3.2 Power law structure supermirror

In 1976, the power law structure was firstly introduced in neutron optics to reflect thermal neutron (Mezei et.al) due to the fact that neutrons may not be absorbed by a material. Since in hard X-ray band the absorption is negligible, in 1992 F. E. Christensen firstly applied this technology to improve the performance of hard X-ray Astronomical instrumentation. A power law mirror was considered to reflect hard X-rays with broaden energy bandwidth. The structure of the power law mirror was described by an empirical equation.

$$d_i = \frac{a}{(b+i)^c} \quad (2.11)$$

Where d_i is the thickness of i -th layer pair. a , b and c are parameters which should be optimized with the help of computer. When designing the structure, an optimization algorithm is used to produce various sets of parameters and select the best one with reference to Function Of Merit (FOM).

$$FOM = \sqrt{\frac{1}{m} \sum_{j=1}^m (R(E_j) - R_{target}(E_j))^2} \quad (2.12)$$

Here, the energy band of interest is dispersed to m points. E_j is the j -th energy point and $R(E_j)$ is the reflectivity calculated by Parratt's algorithm, with a set of parameters. $R_{target}(E_j)$ is a desired reflectivity at energy E_j . Obviously, Eq. 2.12 means the standard deviation of calculated reflectivity profile from a desired one. The optimization algorithm keeps the parameters which produce the lowest FOM. There are many optimization algorithms which can optimize those three parameters. Downhill simplex algorithm is used in most cases. Usually the parameters with minimum FOM can be found without any difficulties.

A great advantage of the power law structure is its convenience in design. In the design process only two things need to determine manually: total layer number of the structure (N) and target reflectivity profile $R_{target}(E_j)$. N is related to the integrated reflectivity within target band. Usually N is determined to maximize the integrated reflectivity and reduce the fabrication difficulties. Following is an example of power law design.

Due to the fact that constant reflectivity within the target band has various applications, target reflectivity with a flat top profile has been assumed. Since the integrated reflectivity may have a direct relationship with the number of layer pairs, the reflectivity profiles of power law structures with different layer numbers are calculated and are presented in Fig. 2.8. In this case, the number of layer pairs is set from 80 to 180, including 123. The integrated reflectivity is calculated and is shown in Fig. 2.9. The reflectivity profiles for n less than 123 does not reach to the upper bound of 55keV (see Fig 2.8). On the other hand, the integrated reflectivity within target band starts to becomes saturated when the number of layer pairs becomes 140 or more. In previous experiments, we experienced that the interfacial roughness of multilayer increased if the total pair number exceeded 120 or so. Then we define the maximum layer pair number to be 123, the same as for Astro-H HXT (Fig. 2.6). The design results are shown as follows,

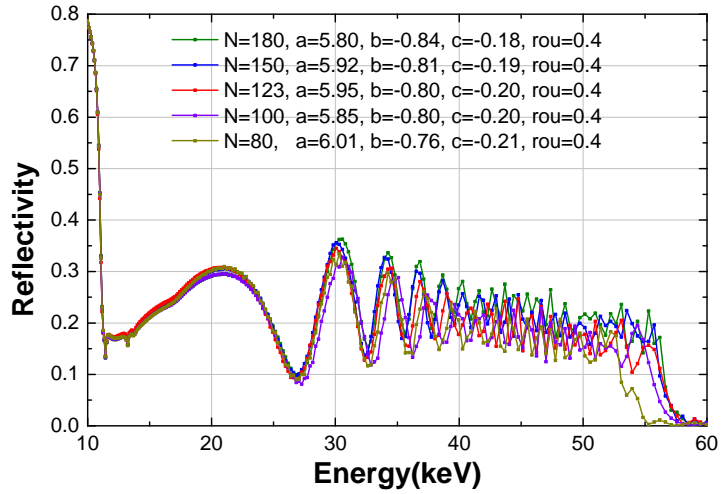


Fig. 2.8 Optimized reflectivity profiles v.s. number of layer pairs.

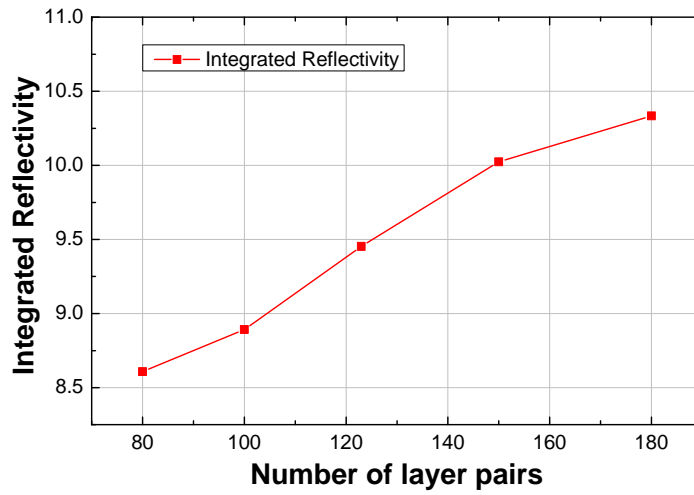


Fig. 2.9 Integrated reflectivity v.s. number of layer pairs.

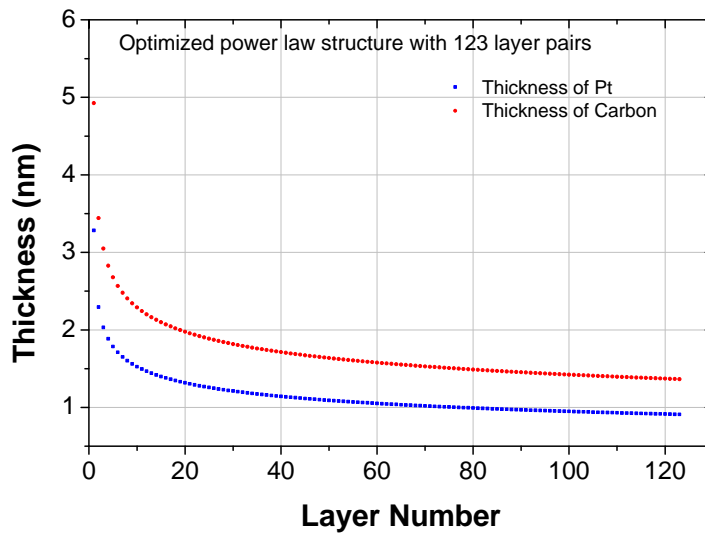


Fig. 2.10 An optimized power law structure with 123 layer pairs.

2.1.3.3 Depth graded structure supermirror (Ref. 8)

In previous sections, the design methods are based on empirical rules. All of them are efficient to design a structure which can satisfy the scientific purpose, but it's hard to demonstrate the essential principle of those rules. In 2001, Igor V. Kozhevnikov gave a theoretical study on depth graded supermirror. The reflectivity of the depth-graded supermirror was successfully connected with a parameter which is called the "gradient of layer number". Although this theory has many limitations such as it cannot analyze the block structure supermirror, it still provides an opportunity to understand the X-ray propagation behavior in depth graded multilayer. Moreover, this theory is the starting point of my theoretical work – a theory to understand the block mirror. Therefore, detail of Igor V. Kozhevnikov's theory is presented in this section.

In order to investigate the propagation of E-M waves in a multilayer structure, the first step is to formulate the multilayer structure by introducing a function of dielectric constants distribution. The purpose of this work is to solve the E-M wave propagation in such structure, and to calculate the reflectivity, which is equal to the emerging amplitude of the E-M wave at the top boundary, as was described in IGOR's theoretical study. In his work, the polarization between two boundaries was neglected due to the fact that the grazing angle is small (< 0.5 degrees).

First, the mathematical expression of the structure can be described by following equation:

$$\varepsilon(z) = \varepsilon_2 + (\varepsilon_1 - \varepsilon_2)U(y(z), \Gamma), \quad z \in [0, L] \quad (2.13)$$

Where $\varepsilon(z)$ is a dielectric constant function of the material for depth z , $U(y(z), \Gamma)$ is a periodic step-like function with the argument $y(z)$. It takes the value 0 or 1 as:

$$U(y(z), \Gamma) = \begin{cases} 0, & m \leq y < m + \Gamma \\ 1, & m + \Gamma \leq y < m + 1 \end{cases} \quad (2.14)$$

$$y(z) = \int_0^z q(z') dz', \quad q(z) > 0 \quad (2.15)$$

Here y is a continuous layer number function for variable z . Γ is the thickness ratio of the heavy element layer to each period, and $q(z)$ is the first derivation of the layer number function. If $q(z)$ is constant, the structure should be a multilayer with a constant d -spacing, and m is the pair number that counted from the top.

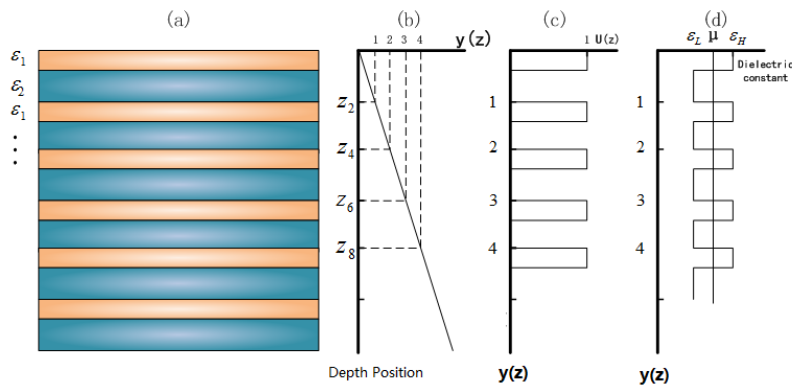


Fig. 2.11 Physical model of a multilayer structure. (a) Cross section of a layered structure. The structure consists of two kinds of materials with two different dielectric constants ε_1 and ε_2 . (b) Layer number function $y(z)$. In case of periodical multilayer, it should be extended to linear function. (c) Step-like function $U(y(z), \Gamma)$ to select the

dielectric constant. (d) Function of dielectric constant.

In order to formulate the E-M wave propagation, the Fourier series expansion has been used to describe the multilayer structure. The expression can be described by following equations:

$$\begin{aligned} \varepsilon(z) &= \mu + \sum_{n=1}^{\infty} B_n \cos(2\pi n y(z) + \pi n \Gamma) \\ \mu &= \Gamma \varepsilon_1 + (1-\Gamma) \varepsilon_2, \quad B_n = 2(\varepsilon_1 - \varepsilon_2) \frac{\sin(\pi n \Gamma)}{\pi n} \end{aligned} \quad (2.16)$$

Where μ is the mean dielectric constant of the material in layered structure.

E-M wave propagation with the grazing angle θ in the material is described by the following equation:

$$E''(z) + k^2(\varepsilon(z) - \cos^2(\theta))E(z) = 0, \quad k = \frac{2\pi}{\lambda} \quad (2.17)$$

The wave equation (Eq. 2.17) can be re-written in an integral form:

$$E(z) = E_0 - k^2 \int_0^L g(z, z')(\varepsilon(z') - \mu)E(z')dz' \quad (2.18)$$

Where $g(z, z')$ means the Green function of a equivalent wave equation which describing the interaction of a X-ray wave in homogeneous film with thickness L and dielectric constant μ . This Green function is expressed with respect to two standard solutions $E_1(z)$ and $E_2(z)$. They correspond to a negative propagating wave and a positive propagating wave following the depth, z .

$$\begin{aligned} g(z, z') &= \frac{E_1(z_>)E_2(z_<)}{2ikt_f}, \\ z_> &= \min(z, z') \quad z_< = \max(z, z') \end{aligned} \quad (2.19)$$

Here t_f is the X-ray transmission amplitude in a homogeneous film. Since only the X-rays operating out of the total external reflection region is interested, the reflected waves can be neglected and transmitted waves are retained. Therefore, $E_1(z)$ and $E_2(z)$ can be expressed in following equations,

$$\begin{aligned} E_1(z) &\approx \begin{cases} \exp(ivz) & \text{at } z < 0 \\ \exp(i\kappa z) & \text{at } z \in [0, L] \\ t_f \exp(ivz) & \text{at } z > L \end{cases} \\ E_2(z) &\approx \begin{cases} t_f \exp(-ivz) & \text{at } z < 0 \\ t_f \exp(-i\kappa z) & \text{at } z \in [0, L] \\ \exp(-ivz) & \text{at } z > L \end{cases} \end{aligned} \quad (2.20)$$

$$v = k \sin \theta, \quad \kappa = \kappa_1 + i\kappa_2 = k\sqrt{(\mu - \cos^2(\theta))}$$

Combine Eq. 2.18-2.20, we can get the expression for the field inside the multilayer structure.

$$\begin{aligned} E(z) &= \exp(i\kappa z) \left\{ 1 + \frac{ik^2}{2\kappa} \int_0^z E(z') [\varepsilon(z') - \mu] \exp(-i\kappa z') dz' \right\} \\ &+ \exp(-i\kappa z) \left\{ \frac{ik^2}{2\kappa} \int_z^L E(z') [\varepsilon(z') - \mu] \exp(i\kappa z') dz' \right\}, \quad z \in [0, L] \end{aligned} \quad (2.21)$$

And obviously, the reflectivity can be expressed as

$$r = \frac{ik^2}{2\kappa} \int_0^L E(z') [\varepsilon(z') - \mu] \exp(i\kappa z') dz' \quad (2.22)$$

The field inside the multilayer structure is considered as two opposite direction waves travelling along the z-axis

$$E(z) = \exp(i\kappa z)U_+(z) + \exp(-i\kappa z)U_-(z) \quad (2.23)$$

Substituting Eq. 2.16 and Eq. 2.23 into Eq. 2.21 and Eq. 2.22, the expression of U_+ and U_- can be obtained.

$$U_+(z) = 1 + \frac{ik^2}{4\kappa} \sum_{n=1}^{\infty} B_n \exp(in\pi\Gamma) \int_0^z U_-(z') \exp[i2\pi n y(z') - 2i\kappa z'] dz' + S_+(z) \quad (2.24)$$

$$U_-(z) = \frac{ik^2}{4\kappa} \sum_{n=1}^{\infty} B_n \exp(-in\pi\Gamma) \int_z^L U_+(z') \exp[-i2\pi n y(z') + 2i\kappa z'] dz' + S_-(z) \quad (2.25)$$

And

$$r = \frac{ik^2}{4\kappa} \sum_n B_n \exp(-i\pi n \Gamma) \int_0^L U_+(z') \exp[-2i\pi n y(z') + 2i\kappa z'] dz' + S_-(0) \quad (2.26)$$

The Eq. 2.24-2.26 is very important and I'll explain the physical meaning of those equations in next section.

$S_{\pm}(z)$ are the terms include all the terms that cannot be developed. In IGOR's theory, it is assumed that the spectral band of a depth-graded multilayer is much wider than that of a periodical multilayer. Therefore comparing with the conventional multilayer, the resonance interaction of a monochromated X-ray wave only occurs within a narrow position which satisfies the Bragg condition. The value of the integral presented in Eq. 2.24-2.26 is mainly due to the stationary point z , which can be expressed as

$$\frac{dy(z)}{dz} \equiv q(z) = \frac{\kappa(\lambda)}{\pi n}, \quad n=1,2,\dots \quad (2.27)$$

Here n is derived from the Fourier series expansion of $\varepsilon(z)$, which corresponds to order of Bragg peak. Considering that the stationary point (where resonance happened) are contained in the integral terms of Eq. 2.24-2.26 and missing in the term of S_{\pm} . Therefore, it does not contribute to the amplitude U_+ and U_- , thus should be omitted.

Up to now, the theory explicitly derived the expression of the wave amplitude propagating in a material, with the Bragg condition Eq. 2.27. However, it's quite difficult to solve the Eq. 2.24-2.26. In order to solve the expression of reflectivity, the theory gives two assumptions.

1. Only one stationary point exists for each wavelength λ in the spectral interval. This assumption constrained the first derivation of $y(z)$ as a monotonically increase/decrease function.
2. The stationary point corresponding to the first order Bragg peak, i.e., $n=1$. This assumption gives a limitation of the interest band: $\lambda_{\max} < 2\lambda_{\min}$. Then, a classical stationary point method has been used.

Consider the integral shown in Eq. 2.26,

$$I(z) \equiv \int_0^z U_+(z') \exp(-i2\pi y(z') + 2i\kappa z') dz' \quad (2.28)$$

Here the phase of the exponential term, $\varphi(z') = 2\kappa z' - 2\pi y(z')$ is expanded to Taylor series at point $z'=z$. Stationary phase method assume that the first derivation of $\phi(z)$ is zero (Bragg condition). Therefore,

$$\begin{aligned} I(z) &\equiv \int_0^z U_+(z') \exp(-i2\pi y(z') + 2i\kappa z') dz' \\ &\sim \int_0^z U_+(z) \exp\{-i[\varphi(z) + \varphi'(z)(z-z') + \frac{1}{2}\varphi''(z)(z-z')^2]\} dz' \end{aligned} \quad (2.29)$$

and $\varphi'(z) = 0$ due to the assumption that point z is stationary point, then,

$$\begin{aligned} I(z) &\approx U_+(z) \exp\{-i[\varphi(z)]\} \int_0^z \exp[\frac{i}{2}\varphi''(z)(z-z')^2] dz' \\ &= \frac{U_+(z)}{\sqrt{2|q'(z)|}} \exp[-i2\pi y(z') + 2i\kappa z'] \int_0^{z\sqrt{2|q'(z)|}} \exp[\frac{i\pi t^2}{2} \text{sign}(q'(t))] dt \end{aligned}$$

In which the integral

$$G(z\sqrt{2|q'(z)|}) = \int_0^{z\sqrt{2|q'(z)|}} \exp[\frac{i\pi t^2}{2} \text{sign}(q'(t))] dt$$

It is expressed as Fresnel integral. In IGOR's theory, it is assumed that the value of the Fresnel integral is asymptotically convergence at $G(z\sqrt{2|q'(z)|}) = 1/2$.

By means of the derivation method introduced in Eq. 2.29, Eq. 2.24-2.26 can be approximated as follows,

$$\begin{aligned} U_+(z) &= 1 + \frac{ik^2 B_1}{4\kappa} \frac{U_-(z)}{\sqrt{2|q'(z)|}} G(z\sqrt{2|q'(z)|}) \times \exp(-2i\kappa z + 2i\pi y(z) + i\pi\Gamma) \\ U_-(z) &= \frac{ik^2 B_1}{4\kappa} \frac{U_+(z)}{\sqrt{2|q'(z)|}} G((L-z)\sqrt{2|q'(z)|}) \times \exp(2i\kappa z - 2i\pi y(z) - i\pi\Gamma) \\ r(\lambda) &= \frac{ik^2 B_1}{4\kappa} \frac{U_+(z)}{\sqrt{2|q'(z)|}} \exp(2i\kappa z - 2i\pi y(z) - i\pi\Gamma) \times [G(z\sqrt{2|q'(z)|}) + G((L-z)\sqrt{2|q'(z)|})] \\ z &= z(\lambda) \end{aligned} \quad (2.30)$$

Eventually, the reflectivity of a graded multilayer can be derived from Eq. 2.30

$$\begin{aligned} R(\lambda) &= |r(\lambda)|^2 = \left| \frac{2\eta(\lambda)\sqrt{|q'(z)|}}{\eta^2(\lambda) + |q'(z)|} \right| \exp(-4\kappa_2(\lambda)z) \\ \eta(\lambda) &\equiv \frac{k^2 B_1}{8\kappa} = \frac{\pi}{4\lambda} \frac{B_1(\lambda)}{\sqrt{\mu(\lambda) - \cos^2(\theta)}} \\ B_1 &= 2(\varepsilon_1 - \varepsilon_2) \frac{\sin(\pi\Gamma)}{\pi} \\ z &= z(\lambda) \end{aligned} \quad (2.31)$$

In Eq. 2.31, the final expression of multilayer reflectivity is related to

1. The depth to reflect the X-ray of wavelength λ : $z=z(\lambda)$
2. The depth gradient (second derivation of $y(z)$) at the depth z . (caused by the stationary point)

Eq. 2.31 shows that, when the depth gradient changes rapidly ($|q'| \rightarrow \infty$), the reflectivity decrease to 0. When the period gradient decrease, the reflectivity increase firstly, then obtain a maximum value of $|q'| \sim \eta^2$ and then down to 0 again. It is not true because of the stationary phase approximation. Therefore, the theory gives a constrain on $q'(z)$:

$$|q'(z)| > \eta^2(\lambda) \quad (2.32)$$

Subsequently, the Eq. 2.31 cannot satisfy a block structure mirror.

Since Eq. 2.31 gives the relation between the gradient of the structure and the reflectivity at corresponding wavelength, it is possible to design the multilayer structure with a desired target reflectivity, which is described as follows,

From Eq. 2.31,

$$|q'(z)| = \eta^2(\lambda) \frac{2 - \tau + 2\sqrt{1 - \tau}}{\tau} \equiv F(\lambda, z) \quad (2.33)$$

$$\tau \equiv R(\lambda) \exp(4\kappa_2(\lambda)z)$$

From the Bragg condition,

$$q(z) = \frac{\kappa_1(\lambda)}{\pi} \quad (2.34)$$

And there is a simple equation

$$\frac{dq}{dz} = \frac{dq}{d\lambda} \frac{d\lambda}{dz} \quad (2.35)$$

Substituting Eq. 2.33 and Eq. 2.35,

$$\frac{d\lambda}{dz} = \pm \pi F(\lambda, z) \left| \frac{d\kappa_1(\lambda)}{d\lambda} \right|^{-1} \quad (2.36)$$

The Eq. 2.36 gives the relation between the X-ray wavelength λ and the depth z where the reflection occurs. Starting from continuous z and λ to a discrete numerical variable z_j and λ_j , the recurrent expressions is obtained which can derive a multilayer with desired reflectivity

$$z_{2j+2} \cong z_{2j} + \frac{\pi}{\kappa_1(\lambda_{2j})}, \quad j=0,1,2\dots$$

$$z_{2j+1} = z_{2j} + \Gamma(z_{2j+2} - z_{2j})$$

$$\lambda_{2j+2} \cong \lambda_{2j} \pm 2\pi^2 F(\lambda_{2j}, z_{2j}) \left| \frac{d\kappa_1^2(\lambda_{2j})}{d\lambda} \right|^{-1}$$

$$z_0 = 0, \quad \lambda_0 = \lambda_{\min} \text{ or } \lambda_{\max}$$
(2.37)

In order to prove that the recurrent expressions above are correct, an algorithm has been programmed, based on those expressions. We assume to design a multilayer structure with the

target reflectivity of 30% from 25keV to 50keV, with grazing angle of 0.36deg. The designed d-spacing from Eq. 2.37 and its reflectivity calculated by Parratt's algorithm is shown as follows,

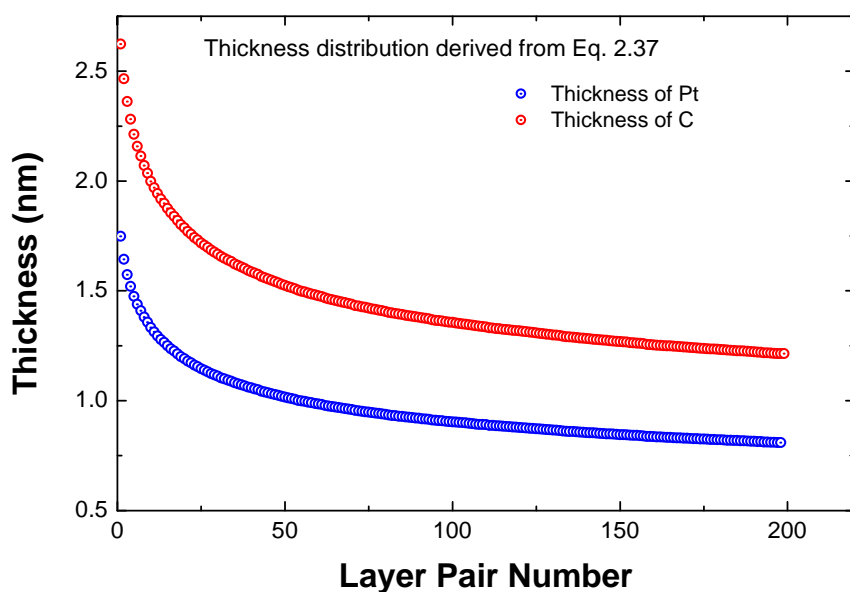


Fig. 2.12 Thickness distribution derived from Eq. 2.37.

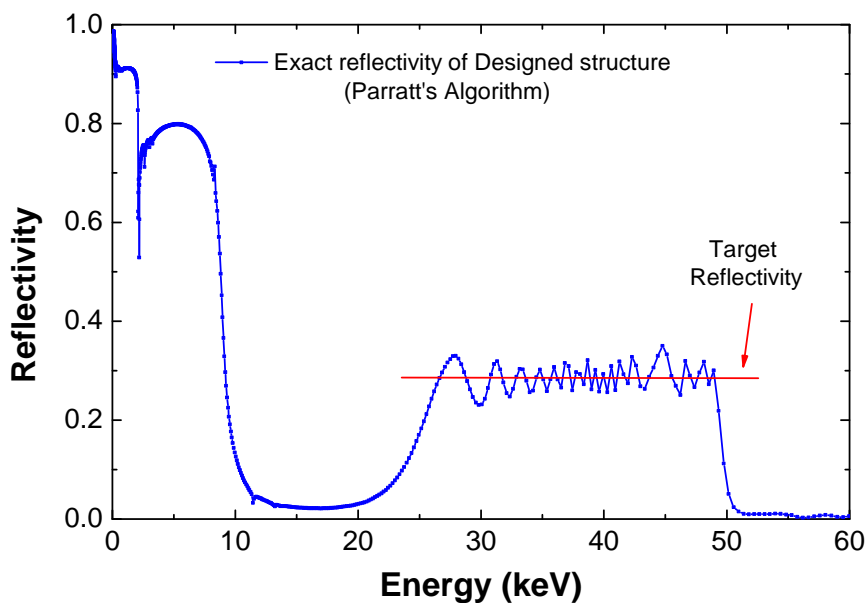


Fig. 2.13 Exact reflectivity of designed structure, Parratt's algorithm.

As are shown in figures above, IGOR's theoretical work perfectly explains the relation between the depth of a structure and its reflectivity. His recurrent expressions (Eq. 2.37) provide a design rule for depth-grad layer structure. The designed structure can provide a good response following the target.

However as is mentioned in stationary method, the theory does not satisfy a periodic multilayer, subsequently the basic principle of a block mirror has not been granted. And it is the starting point of my theoretical work. In following section, the block structure mirror will be analyzed.

2.2 Theoretical study of the block structure supermirror

As is mentioned in Chapter 2.1.3.1, the block structure supermirror is very useful. It has been applied on InFOCuS and ASTRO-H telescopes. Until now all the design rules are empirical. In this section I will introduce my theoretical work on block mirror by means of IGOR's equations.

2.2.1 Simplification of Igor's theory

IGOR's theory cannot deal with the block structure because it applied a stationary phase method (Eq. 2.29) to solve Eq. 2.24-2.26. In order to solve the block structure, another way should be found on those equations. Firstly, let's analyze the physical essence of Eq. 2.24-2.26, which is written here.

$$U_+(z) = 1 + \frac{ik^2}{4\kappa} \sum_{n=1}^{\infty} B_n \exp(in\pi\Gamma) \int_0^z U_-(z') \exp[i2\pi n y(z') - 2i\kappa z'] dz' + S_+(z) \quad (2.38)$$

$$U_-(z) = \frac{ik^2}{4\kappa} \sum_{n=1}^{\infty} B_n \exp(-in\pi\Gamma) \int_z^L U_+(z') \exp[-i2\pi n y(z') + 2i\kappa z'] dz' + S_-(z) \quad (2.39)$$

In the multilayer structure, U_+ is the amplitude of the E-M wave traveling from the top to the bottom; and U_- is the amplitude of the E-M wave traveling from the bottom to the top. k means the wave number, which is equivalent with $2\pi / \lambda$. μ corresponds to the mean dielectric constant, κ is the complex wave number equal to $k\sqrt{\mu - \cos^2(\theta)}$, which means the normal component of the wave vector in the structure. B_n and $y(z)$ comes from Eq. 2.15-2.16, and L is the total thickness of the multilayer. $S_+(z)$ and $S_-(z)$ are the terms which may oscillate rapidly which can be derived in Eq. 2.21. They will be discussed in the next section and will be neglected finally. Obviously those two equations demonstrate the relationship between the amplitudes of a positive and a negative E-M wave in the multilayer, which is essential for Green function.

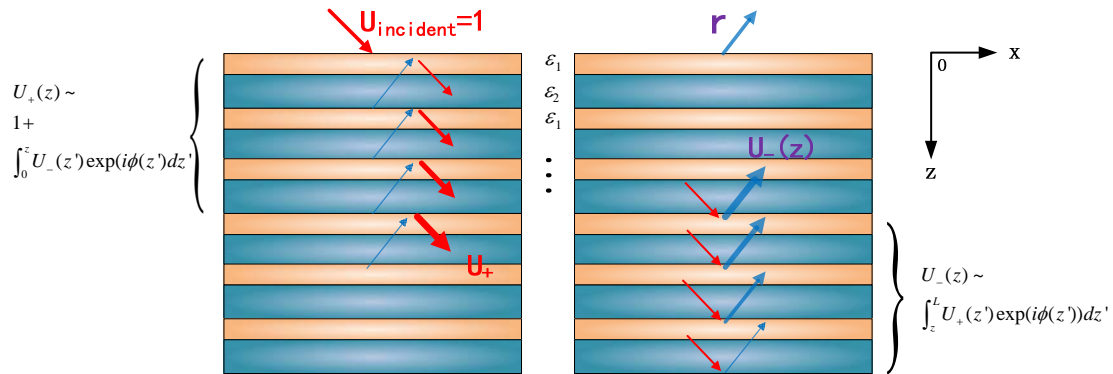


Fig. 2.14 Physics meaning of Eq. 2.38 and Eq. 2.39.

In Eq. 2.38, the constant 1 before the plus sign means the amplitude of the incident X-ray at the top (normalized as 1). The term in front of the integration sign corresponds to the reflectivity of each boundary. The integration term means the sum of the phase-shifted U_- (negative traveling wave) from the top to depth z . U_- means the amplitude of the E-M wave propagating upward (along Z axis). Eq. 2.39 can be demonstrated as the same way. And the amplitude of reflected wave is equal to the amplitude $U_-(0)$ of the E-M wave on the top of the structure, as is shown in Eq. 2.26 and written below.

$$r = \frac{ik^2}{4\kappa} \sum_n B_n \exp(-i\pi n\Gamma) \int_0^L U_+(z') \exp[-2i\pi ny(z') + 2i\kappa z'] dz' + S_-(0) \quad (2.40)$$

Since Eq. 2.38 and Eq. 2.39 are iteratively expressed, the analysis of those equations is relatively complex (stationary phase method for example). However, the major goal of my approach is to analyze the propagation behavior of the E-M waves in the multilayer structure and to quickly derive the spectrum profile of reflectivity from the structure, and then provide a qualitative guidance of multilayer design, especially for a block structure supermirror with less oscillation in the reflectivity spectrum, rather than to derive accurate expression for the spectrum profile of reflectivity of the block structure supermirror.

Then I introduce a “vector model” approximation, which means the incident X-ray may not lose intensity when it propagates through boundaries, i.e. $U_+(z) \approx 1$. Though this approximation may leads to overestimation of the reflectivity, the spectrum profile of the reflectivity can be calculated qualitatively,

1. Amplitude reflectivity of each boundary is very low for hard X-rays at large grazing angles. Therefore the amplitude of the X-ray propagating in the structure is still comparable with unity, i.e., 1.
2. The vector model is simple, which means it's suitable for qualitative analysis of the shape of the reflectivity (oscillation).
3. Reflectivity curves will be calculated by an exact method (Parratt's recurrence) and the results from vector model will be compared to demonstrate the validity of this approximation.

According to the vector model, the reflectivity can be simplified as,

$$r = U_-(0) = \frac{ik^2}{4\kappa} \sum_{n=1}^{\infty} B_n \exp(-i\pi n\Gamma) \int_0^L \exp[-2\pi iny(z')] \exp(i2\kappa z') dz' + S_-(0) \quad (2.41)$$

Eq. 2.41 can be considered as a Laplace transformation.

$$r(\kappa) = \frac{ik^2}{4\kappa} \sum_{n=1}^{\infty} B_n \exp(-i\pi n\Gamma) \mathcal{L}[\exp(-i2\pi ny(z))] \Big|_0^L + S_-(0) \quad (2.42)$$

In this expression, the argument κ is used instead of k to take the optical constant of the material into account. The exponential term $\exp(-i2\pi ny(z))$ is defined as a “structure function”, which is the presentation of the optical constant variation. The term $\mathcal{L}[\exp(-i2\pi ny(z))] \Big|_0^L$ is defined as “spectral function” of the “structure function”, which corresponds to the frequency component of the multilayer structure. $S_-(z)$ will be discussed later. Considering the fact that term $i \exp(-i\pi n\Gamma)$ may not affect the absolute value of $r(k)$ (only change the phase angle), subsequently this term has been omitted.

In Eq. 2.42, the integer n corresponds to the order of the Bragg peak. In this section, we only analyze the reflectivity contributed by the first order Bragg peak to simplify the expression derivation, i.e. $n=1$. It is because the amplitude of second order Bragg peak is negligible.

The expression of the reflectivity can be derived as:

$$r(\kappa) = \frac{[\varepsilon_1(k) - \cos^2(\theta)] - [\varepsilon_2(k) - \cos^2(\theta)]}{\Gamma \cdot [\varepsilon_1(k) - \cos^2(\theta)] + (1 - \Gamma) \cdot [\varepsilon_2(k) - \cos^2(\theta)]} \frac{\sin(\pi\Gamma)}{2\pi} \{\kappa \mathcal{L}[\exp(-i2\pi y(z))]\} + S_-(0) \quad (2.43)$$

Subsequently the intensity reflectivity can be expressed in following equation:

$$R(\kappa) = \frac{[\varepsilon_1 - \cos^2(\theta)] - [\varepsilon_2 - \cos^2(\theta)]}{[\varepsilon_1 - \cos^2(\theta)] + [\varepsilon_2 - \cos^2(\theta)]} \frac{1}{\pi^2} \kappa^2 \mathcal{L} * \mathcal{L}^* + (\text{terms including } S_-(0)) \quad (2.44)$$

In this equation, the phase has been eliminated due to the fact that the conjugation may produce a real value. However, the interference between different parts of the structure (BLOCKS) still exists because:

$$\mathcal{L}(A + B) * \mathcal{L}^*(A + B) = \mathcal{L}(A) * \mathcal{L}^*(A) + \mathcal{L}(B) * \mathcal{L}^*(B) + \mathcal{L}(A) * \mathcal{L}^*(B) + \mathcal{L}^*(A) * \mathcal{L}(B)$$

Here, A and B are the different parts of the supermirror structure (different blocks for example). Once the spectral function of all the structure (blocks) has been considered, the third and fourth term in the right side in the expression may lead to the oscillation of the reflectivity, at least. Up to now, IGOR's equations have been simplified to Eq. 2.43 and 2.44. The response of a multilayer has been correlated to the Laplacian spectrum of the structure function. In next section I'll introduce how to use those equations to analyze a periodical multilayer.

2.2.2 Theoretical analysis of the periodical multilayer

Firstly, we analyze the Eq. 2.43 without $S_-(0)$. The structure function of each block, i.e., periodic multilayer, can be expressed in following equation:

$$\exp[-i2\pi y(z)] \Big|_0^{L_0} = \exp(-ik_0 z) \Big|_0^{L_0} \quad (2.45)$$

k_0 means the inverse lattice of the multilayer which is equal to $2\pi/d$. d means the d-spacing and L_0 means the total thickness of the block. We looked up the table and found the expression of Laplace transform of the structure function defined in $[0, +\infty]$ is:

$$\mathcal{L}[\exp(-ik_0 z) \Big|_0^{\infty}] \equiv \mathcal{L}[\exp(-ik_0 z)u(z)] = \frac{1}{i(2\kappa - k_0)} \quad (2.46)$$

Where $u(z)$ is the unit step function from the definition of the Laplace transform. Since the total thickness of one block is limited, we use the delay operator on the image function and subtract them from each other to cut out a block structure, as shown in following figure,

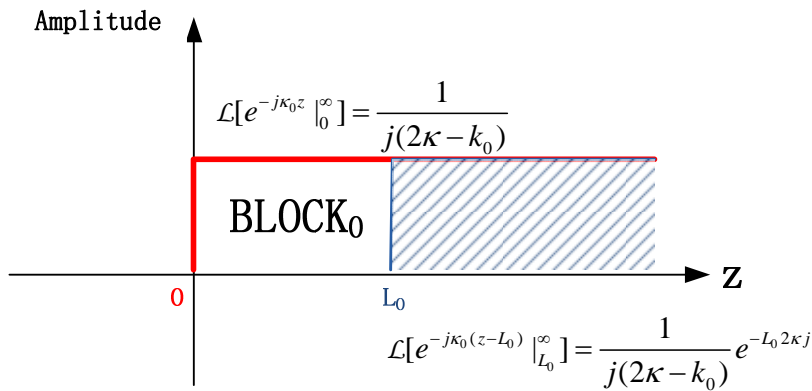


Fig. 2.15. The spectral function of a block which begin from original point (zero). k_0 is the inverse lattice of Block₀. Since the total thickness of Block₀ is L_0 , the spectral function of the structure can be derived as the subtraction between an image function (original function defined from 0 to infinity) and an delayed image function (original function defined from L_0 to infinity).

Therefore, the Laplace transformation of the structure function of Block₀ should be:

$$\mathcal{L}[BLOCK_n] = \frac{1}{j(2\kappa - k_0)} [1 - \exp(-L_0 2\kappa i)] \quad (2.47)$$

Second, with the “vector model” assumption, here I’ll discuss the $S_-(0)$ of one block.

From Eq. 2.18-2.21, the original expression of U_- is derived,

$$U_-(z) = \frac{ik^2}{2\kappa} \sum_{n=1}^{\infty} B_n \int_z^L U_+(z') \cos[2\pi n y(z') + \pi n \Gamma] \exp(i2\kappa z') dz' \quad (2.48)$$

While we apply the “vector model”, i.e. $U_+(z)=1$, and $z=0$ to derive the reflectivity, then

$$r = \frac{ik^2}{2\kappa} \sum_{n=1}^{\infty} B_n \int_0^L \cos[2\pi n y(z') + \pi n \Gamma] \exp(i2\kappa z') dz' \quad (2.49)$$

The amplitude reflectivity is proportional to the Laplace transform of a cosine function. And the cosine function describes the varying of the dielectric constant. However, the textbook told us that the spectrum of the cosine function consists of a positive frequency component and a negative frequency component which are symmetrical with Y-axis.

Subsequently, the Eq. 2.49 can be derived as follows,

$$\begin{aligned} r(\kappa) &= \frac{ik^2}{4\kappa} \sum_{n=1}^{\infty} B_n \exp(-i\pi n \Gamma) \mathcal{L}[\exp(-i2\pi y(z)) \Big|_0^L] + S_-(0) \\ S_-(0) &= \frac{ik^2}{4\kappa} \sum_{n=1}^{\infty} B_n \exp(i\pi n \Gamma) \mathcal{L}[\exp(i2\pi y(z)) \Big|_0^L] \end{aligned} \quad (2.50)$$

We conclude that the negative frequency component directly relates with S_- . For one block structure, the positive frequency component has already been described by Eq. 2.47, and decay quickly when the normal component of the wave vector κ is far away from the inverse lattice k_0 . Considering that the tail of the negative component drops so much at the position of the peak of positive component, it is concluded that $S_-(0)$ can be neglected in our reflectivity expression.

Therefore the expression of one block, of which the surface is defined at 0 point, can be expressed as follows,

$$r(\kappa) = \frac{[\varepsilon_1(k) - \cos^2(\theta)] - [\varepsilon_2(k) - \cos^2(\theta)]}{[\varepsilon_1(k) - \cos^2(\theta)] + [\varepsilon_2(k) - \cos^2(\theta)]} \frac{1}{\pi} \frac{\kappa}{j(2\kappa - k_0)} [1 - \exp(-L_0 2\kappa i)] \quad (2.51)$$

As is known to all, in the theory of Fourier/Laplace Transformation, if a function $F(k)$ (named as image function) is the Fourier transform of a function $f(t)$ (named as original function), then there exist a property:

$$F(k) \exp(-ikt_0) = \mathcal{F}[f(t - t_0)] \quad (2.52)$$

Here, t_0 is an arbitrary constant. Eq 2.52 means that when the original function is drifted a distant as t_0 , the Fourier transform of the original function, i.e., image function, should time a “delay operator” as $\exp(-ikt_0)$.

In the case of a block structure supermirror, the surface of one block (periodical multilayer) is not always located at 0 point, as is shown in following figure.

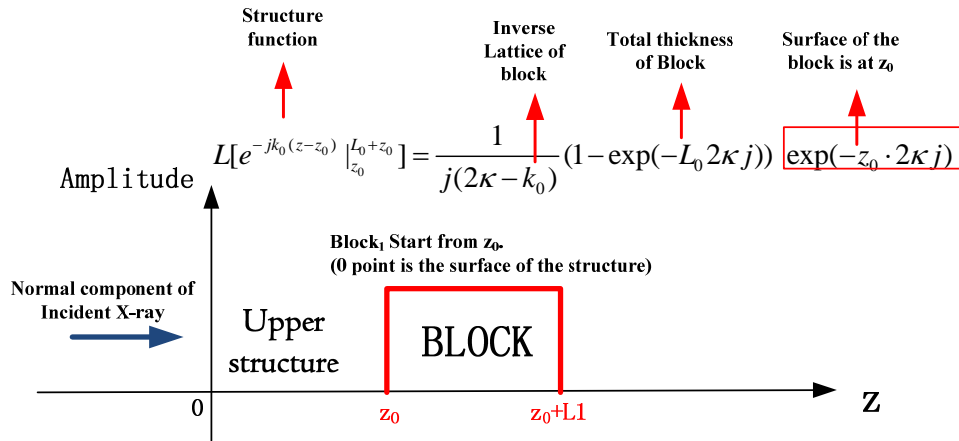


Fig. 2.16, A block which starts from z_0 .

Therefore, the expression of a block's reflectivity should multiply to a delay operator,

$$r(\kappa) = \frac{[\varepsilon_1(k) - \cos^2(\theta)] - [\varepsilon_2(k) - \cos^2(\theta)]}{[\varepsilon_1(k) - \cos^2(\theta)] + [\varepsilon_2(k) - \cos^2(\theta)]} \frac{1}{\pi} \frac{\kappa}{j(2\kappa - k_0)} [1 - \exp(-L_0 2\kappa j)] \exp(-z_0 \cdot 2\kappa j) \quad (2.53)$$

Until now, the reflectivity of a block has been derived. From this equation, we can easily understand the X-ray propagation behavior in the structure, demonstrated below.

Firstly, $r(\kappa)$ is a complex function with the complex variable κ . It can be written as a full equivalent form

$$r(\kappa) = |r(\kappa)| \exp[i\phi(\kappa)] \quad (2.54)$$

In which $\phi(\kappa)$ is a phase function which means the phase of reflected wave at the surface, defined at 0 point shown in Fig. 2.16. From a practical point of view, the phase is shown in following figure.

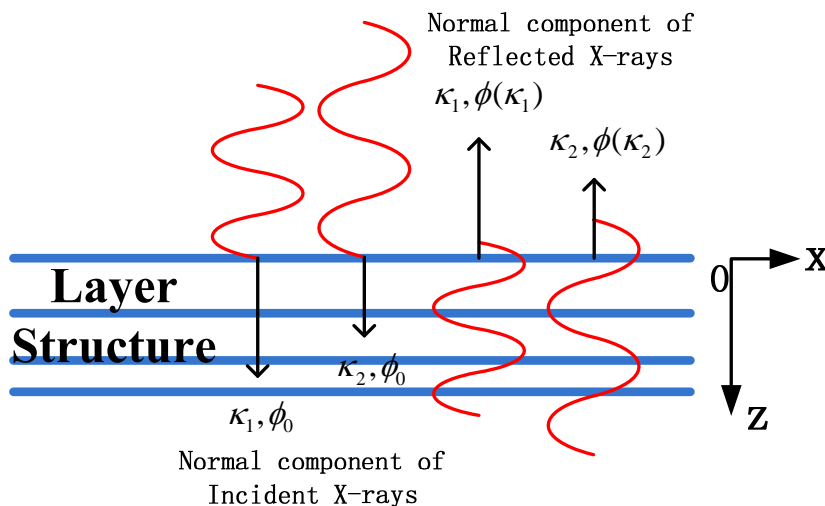


Fig. 2.17 Sketch of the physics meaning of phase function $\phi(\kappa)$

In Fig. 2.17, we assume two incident X-rays with different wave number are reflected by a layer structure. The phase of incident X-rays are the same and defined as 0. Then $\phi(\kappa)$ gives the information of the reflected E-M wave's phase at the surface of the 0 point (surface).

We consider Eq. 2.53 and assume $z_0=0$. The phase function can be derived as follows,

$$\angle r(\kappa) = \angle \left\{ \frac{[\varepsilon_1(k) - \cos^2(\theta)] - [\varepsilon_2(k) - \cos^2(\theta)]}{[\varepsilon_1(k) - \cos^2(\theta)] + [\varepsilon_2(k) - \cos^2(\theta)]} \frac{1}{\pi} \frac{\kappa}{j(2\kappa - k_0)} [1 - \exp(-L_0 2\kappa i)] \right\} \quad (2.55)$$

In hard X-ray band, we assume that the absorption is negligible. Consequently,

$$\frac{[\varepsilon_1(k) - \cos^2(\theta)] - [\varepsilon_2(k) - \cos^2(\theta)]}{[\varepsilon_1(k) - \cos^2(\theta)] + [\varepsilon_2(k) - \cos^2(\theta)]}$$

The contrast term is considered as a real function and does not contribute additional phase shift. Then,

$$\begin{aligned} \phi(\kappa) &= \angle r(\kappa) = \angle \left\{ \frac{\kappa}{j(2\kappa - k_0)} [1 - \exp(-L_0 2\kappa i)] \right\} \\ &= \angle \left\{ \frac{\kappa}{j(2\kappa - k_0)} [\exp(L_0 \kappa i) - \exp(-L_0 \kappa i)] \exp(-L_0 \kappa i) \right\} \\ &\approx \angle \exp(-L_0 \kappa i) \\ &= -L_0 \kappa \end{aligned} \quad (2.56)$$

Hence, the function of a multilayer is linear. It is consistent with the “vector model” approximation,

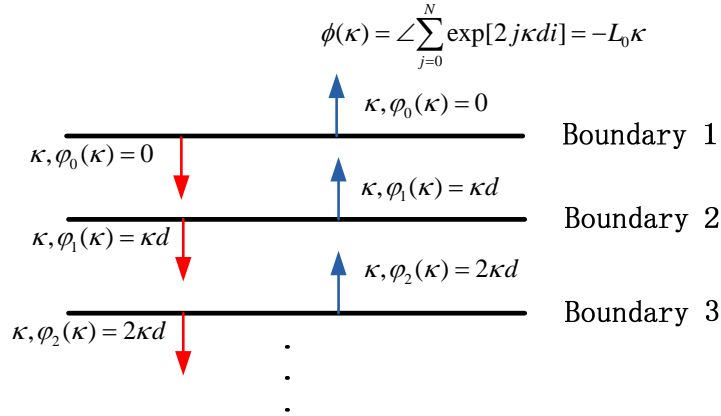


Fig. 2.18. Demonstration of Eq. 2.56. For a reflectance at the surface, the relation of phase and wave vector is linear.

If the surface of the block is not set at 0 point, then we consider the phase function of Eq. 2.53.

$$\begin{aligned} \phi(\kappa) &= \angle r(\kappa) = \angle \left\{ \frac{\kappa}{j(2\kappa - k_0)} [1 - \exp(-L_0 2\kappa i)] \exp(-2iz_0 \kappa) \right\} \\ &\approx \angle \exp(-L_0 \kappa i) + \angle \exp(2iz_0 \kappa) \\ &= (-L_0 - 2z_0) \kappa \end{aligned} \quad (2.57)$$

It is very interesting that the position of a block may affect the slope of phase function. For example, if the surface of the block is set as 0, then the slope of the phase function is $-L_0$. However if the center of the block is set as 0, then the slope of that is 0.

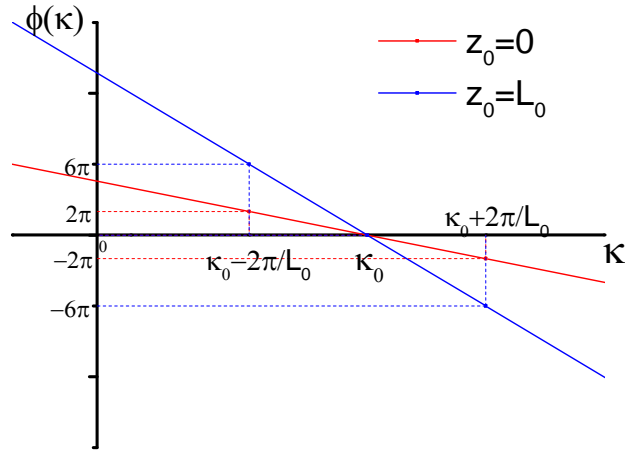


Fig. 2.19. Phase function of blocks at different position.

From Eq. 2.57, we get information that the slope of a phase function varies for the position of the block. As is shown in Fig. 2.19, the slope is steeper when the 0 point is set higher than the surface. The reason is explained in the following figure.

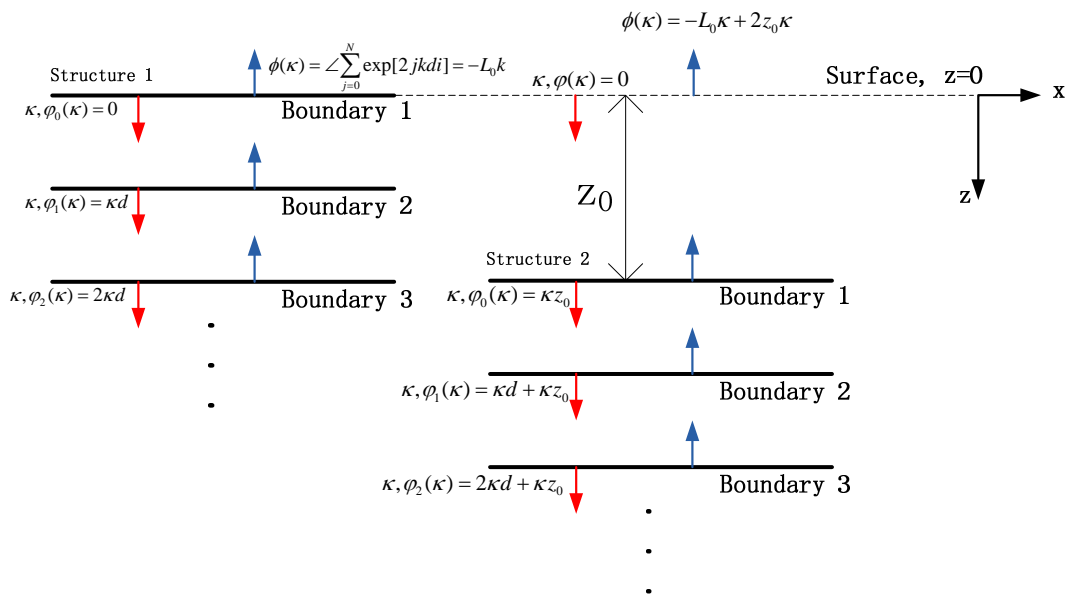


Fig. 2.20. A sketch to explain why the phase function of reflectivity varies with position of a block.

As is shown in Figure above, we assume that the surface of structure 1 is located at 0 point while that of structure 2 is located at Z_0 . When an X-ray reflect by structure 1, the initial phase at the surface is 0. However in case of structure 2, the X-ray have to travel a distance Z_0 firstly. Obviously the phase of X-ray at boundary 1 is a linear function of wave number. Therefore, Eq. 2.57 can be thoroughly understand.

The equation of a multilayer's reflectivity Eq. 2.53 is related to the position of itself. This conclusion is very important, because in block structure supermirror, multilayers are placed one by one. We have to realize that even for the same block, the position of it may significantly change the interference behavior of X-rays propagating inside the structure.

Now let's analyze the amplitude of the reflectivity. As is shown in Eq. 2.57, the position of the multilayer may only affect the slope of $\phi(\kappa)$, but not the absolute value of amplitude. Hence, we set the zero point at the center of a multilayer. Therefore, the slope of $\phi(\kappa)$ is 0. The reflectivity can be derived from Eq. 2.53,

$$\begin{aligned}
r(\kappa) &= \frac{[\varepsilon_1(k) - \cos^2(\theta)] - [\varepsilon_2(k) - \cos^2(\theta)]}{[\varepsilon_1(k) - \cos^2(\theta)] + [\varepsilon_2(k) - \cos^2(\theta)]} \frac{1}{\pi} \frac{\kappa}{i(2\kappa - k_0)} [1 - \exp(-L_0 2\kappa i)] \exp(L_0 \kappa i) \\
&= \frac{[\varepsilon_1(k) - \cos^2(\theta)] - [\varepsilon_2(k) - \cos^2(\theta)]}{[\varepsilon_1(k) - \cos^2(\theta)] + [\varepsilon_2(k) - \cos^2(\theta)]} \frac{1}{\pi} \frac{\kappa}{i(\kappa - k_0/2)} \frac{[\exp(L_0 \kappa j) - \exp(-L_0 \kappa i)]}{2} \\
&= \frac{[\varepsilon_1(k) - \cos^2(\theta)] - [\varepsilon_2(k) - \cos^2(\theta)]}{[\varepsilon_1(k) - \cos^2(\theta)] + [\varepsilon_2(k) - \cos^2(\theta)]} \frac{\kappa L_0}{i\pi} \frac{\sin[L_0(\kappa - k_0/2)]}{L_0(\kappa - k_0/2)} \\
&= \frac{[\varepsilon_1(k) - \cos^2(\theta)] - [\varepsilon_2(k) - \cos^2(\theta)]}{[\varepsilon_1(k) - \cos^2(\theta)] + [\varepsilon_2(k) - \cos^2(\theta)]} \frac{\kappa L_0}{i\pi} \text{SINC}[L_0(\kappa - k_0/2)]
\end{aligned} \tag{2.58}$$

Therefore, the amplitude of the reflectivity is proportional to a Sinc function times normal component of the wave vector. Apply Eq. 2.57, then the reflectivity expression can be written as

$$\begin{aligned}
r(\kappa) &= |r(\kappa)| \exp[i\phi(\kappa)] \\
&= \frac{[\varepsilon_1(k) - \cos^2(\theta)] - [\varepsilon_2(k) - \cos^2(\theta)]}{[\varepsilon_1(k) - \cos^2(\theta)] + [\varepsilon_2(k) - \cos^2(\theta)]} \frac{\kappa L_0}{i\pi} \text{SINC}[L_0(\kappa - k_0/2)] \times \exp[i(-L_0 - 2z_0)\kappa]
\end{aligned} \tag{2.59}$$

In order to demonstrate the physical meaning of Eq. 2.59, we use this equation to calculate an example structure. We assume a multilayer of which the d-spacing is 2.94nm and 17 layer pairs. Therefore the total thickness of this structure is 50nm. The gamma of the structure is 0.4. An incident X-ray beam propagates into the structure with grazing angle of 0.28deg.

We plot the reflectivity in 3-dimensions. X-axis means the energy of incident X-rays. Y-axis means the real part of the reflectivity. Z-axis means the imaginary part of the reflectivity. The calculated results are shown as follows,

We firstly assume $z_0 = -L_0/2$, which means 0 point is set at the center of the structure.

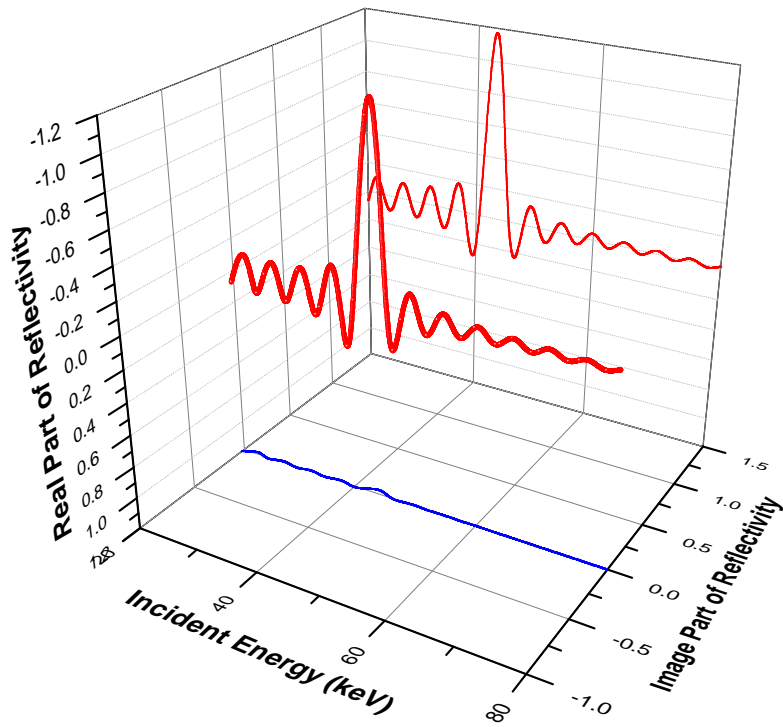


Fig. 2.21. Reflectivity profile of a multilayer structure when 0 position is at center.

Then we assume $z_0 = 0$, which means the 0 point is set at the surface of the structure.

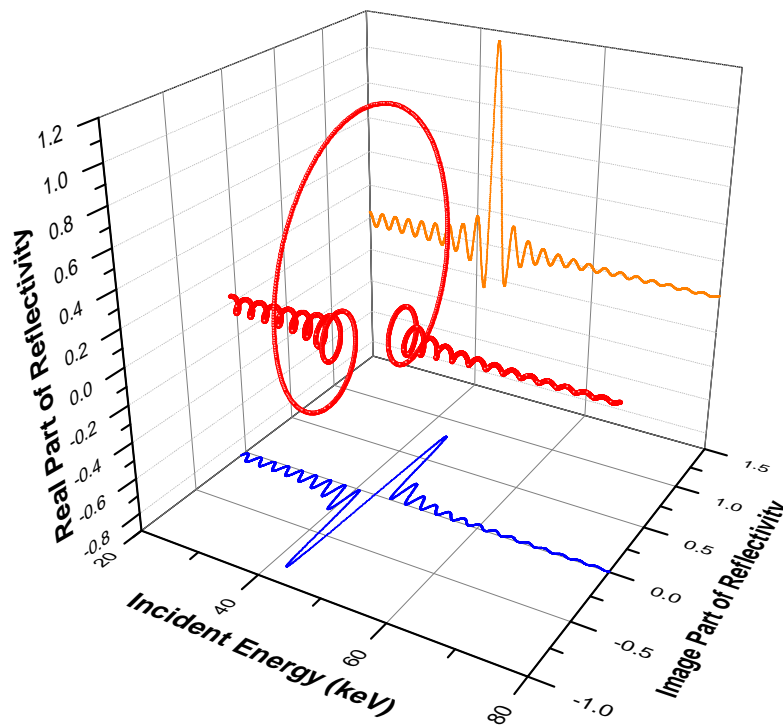


Fig. 2.22. Reflectivity profile of a multilayer structure when 0 position is at surface.

Then we assume $z_0=L_0$, which means the 0 point is set at 50nm above the surface.

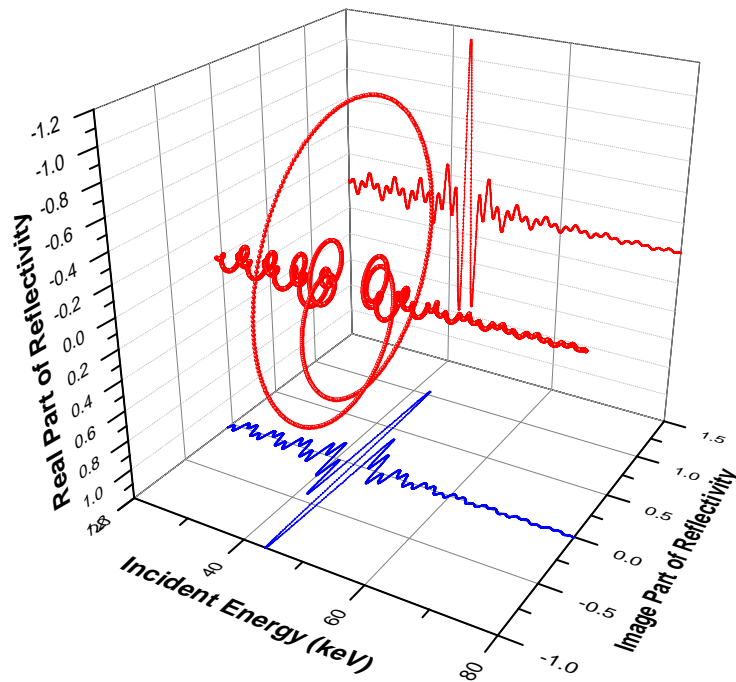


Fig. 2.23 Reflectivity profile of a multilayer structure when 0 position is 50nm above the surface.

As is shown in the figures above, the reflectivity plotted in 3-dimension is very complicated. When the 0 point set at the center of the structure, the reflectivity is in real space and we can see clearly the absolute value of the reflectivity, very similar with a Sinc function. However when the structure shifted downward, then the Sinc function begin to rotate in complex plane (Y-Z dimension). The more the center is far away, the faster the amplitude spin.

One thing I need to emphasis is, let's remove the contrast term and spin term in Eq. 2.59 and look at the absolute value of the rest part of the equation:

$$r(\kappa) \sim \frac{\kappa L_0}{i\pi} \text{SINC}[L_0(\kappa - k_0 / 2)] \quad (2.60)$$

Let's calculate the absolute value of Eq. 2.60:

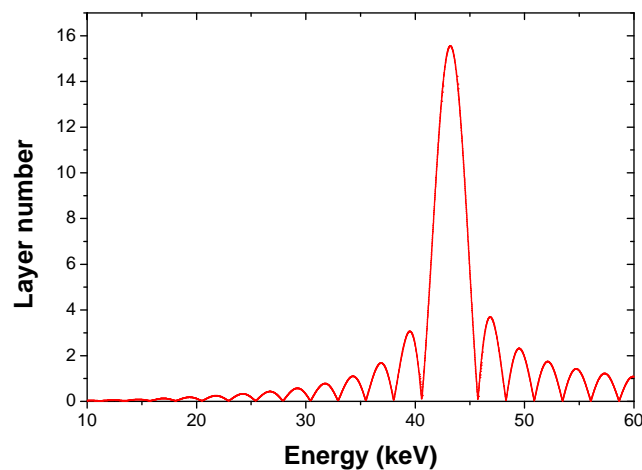


Fig. 2.24 Eq. 2.60's calculate result from the example structure

The Eq. 2.60 derived from Eq. 2.51. It is the product of the normal component of wave number and the spectrum of the structure. Actually, there are 17 layer pairs in the example structure. Please look at the Y-axis of the figure above and I conclude that it is the equivalent layer number of the structure. At the position of the Bragg peak, the value is smaller than 17. That is due to the fact that the absorption has already been considered in the Laplace transformation. The absorption may reduce the equivalent layer number. Hence, the amplitude reflectivity shown in Fig. 2.21 to 2.23 has been thoroughly understood and shown as follows,

$$r(\kappa) = \frac{\text{Contrast of Materials} - \text{Single layer reflectivity}}{\text{Contrast of Materials} + \text{Single layer reflectivity}} \times \frac{\text{Equivalent Layer Number}}{i\pi} \text{SINC}[L_0(\kappa - k_0 / 2)] \times \text{Rotation Term} \exp[i(-L_0 - 2z_0)\kappa]$$

2.2.3 Theoretical analysis of the combined blocks

The amplitude reflectivity expression of a block structure can be determined with the “vector model” assumption,

$$r(\kappa) = \frac{[\varepsilon_1(k) - \cos^2(\theta)] - [\varepsilon_2(k) - \cos^2(\theta)]}{[\varepsilon_1(k) - \cos^2(\theta)] + [\varepsilon_2(k) - \cos^2(\theta)]} \frac{1}{\pi} \kappa \sum_{m=1}^N \mathcal{L}_m \quad (2.61)$$

The spectral function of one block structure is derived in Eq. 2.47. In that case, the surface of the block is set at $z=0$.

For the block structure supermirror, the blocks should be arranged appropriately due to the fact that the starting point of the later block must be the end point of the former block. So the delay operator should be added on the expression of the spectral function to drift the position of each block, as is shown in following figure.

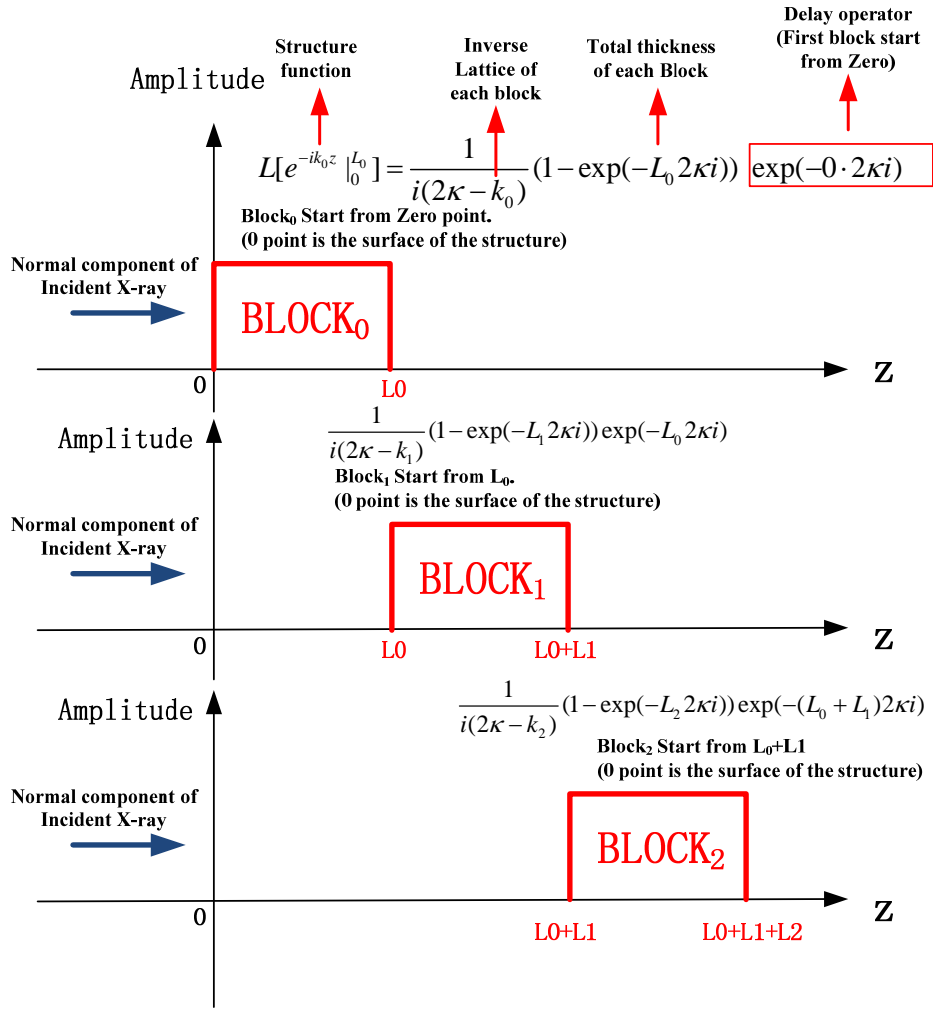


Fig. 2.25. Spectral function of each block in supermirror structure. Normal component of the X-ray wave vector propagate along z-axis to the right side. The spectral function of each block is effected by the total thickness, the d-spacing and the position. The surface of the later block must be the bottom of the former block. Thus, the spectral function of the block structure can be derived.

So the expression of spectral function of the block structure can be derived as follows:

$$\sum_{n=0}^N \mathcal{L}[\text{Block}_n] = \sum_{n=0}^N \left\{ \frac{1}{i(2\kappa - k_n)} [1 - \exp(-L_n 2\kappa i)] \exp\left(-\sum_{j=0}^n L_{j-1} 2\kappa i\right) \right\} \quad (2.62)$$

L_j means the total thickness of j -th block. L_{-1} is defined as 0, which means the surface of the first block is set at 0 point. N is the number of blocks.

Until now, the reflectivity expression of a block structure supermirror has been developed as Eqs. 2.61- 2.62. However, the validity of those equations established with the assumption of the "vector model" is still not clear.

In order to prove the validity of this assumption, calculated results for a model structure are compared in two cases with Eqs. 2.61- 2.62 (vector model with our theoretical study) and exact method (Parratt's algorithm).

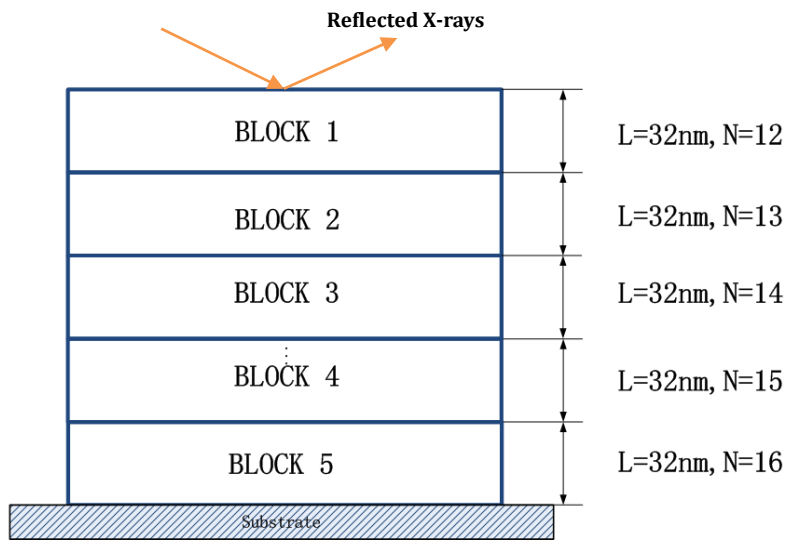


Fig. 2.26 Demonstration the validity of the “vector model” assumption. In this example, the thickness of each block is equal (constant) and set as 32nm. The layer number of each block increases incrementally from 12 to 16.

The above Fig. 2.26 demonstrate the sample structure which consisting of five blocks. For each block, the thickness is set as 32nm and the layer number is incrementally increasing from 12 to 16. The material of layer pair is Pt/C and the grazing incident angle is set at 0.3deg. Then Eqs. 2.61 and 2.62 are used to calculate the reflectivity,

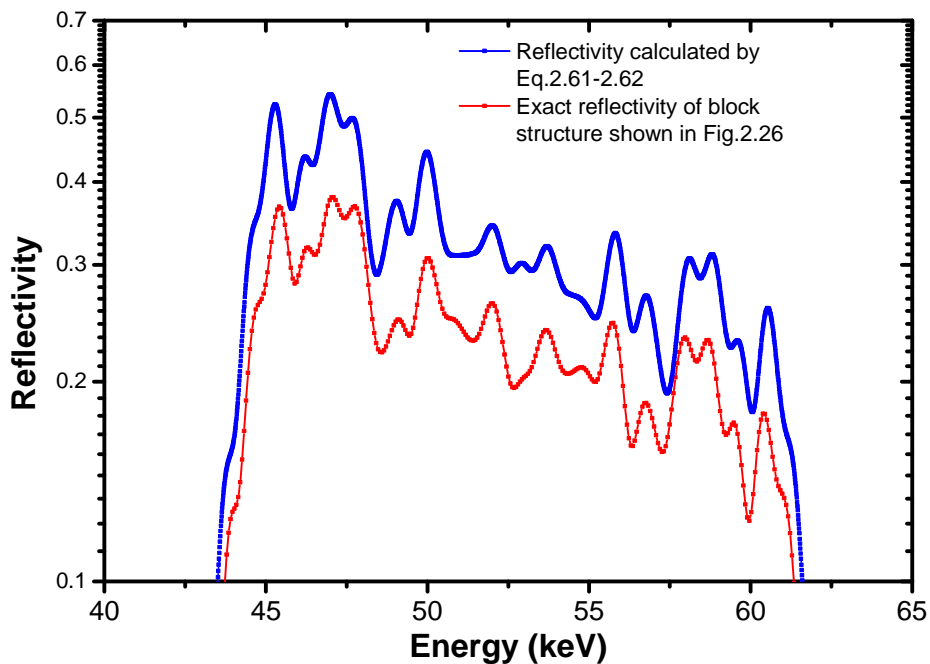


Fig. 2.27 Calculated reflectivity of the structure shown in Fig.2.26. The red line is the reflectivity calculated by exact method (parratt’s recurrence) and the blue line is calculated by Eqs. 2.61 and 2.62. The oscillation of these lines is very similar, which suggests that “vector model” approach is enough to describe the interference behavior of the X-ray propagating in a block mirror.

In Fig. 2.27, the blue line is the reflectivity calculated by Eqs. 2.61 and 2.62. The red line is the reflectivity calculated by exact method. Our calculation result (blue) is higher because of the “vector model” assumption. However, the reflectivity profiles (oscillations) are very similar with each other, which suggest that the vector model is useful to qualitatively analyze the interference behavior of the X-ray in block structure.

In case of the block structure supermirror, Eqs. 2.61 and 2.62 may help us to understand the interference behavior of the X-ray propagation.

Similar with the method shown in Fig. 2.21-2.23, the reflectivity profiles shown in Fig. 2.27 can also be plotted in 3 dimensions,

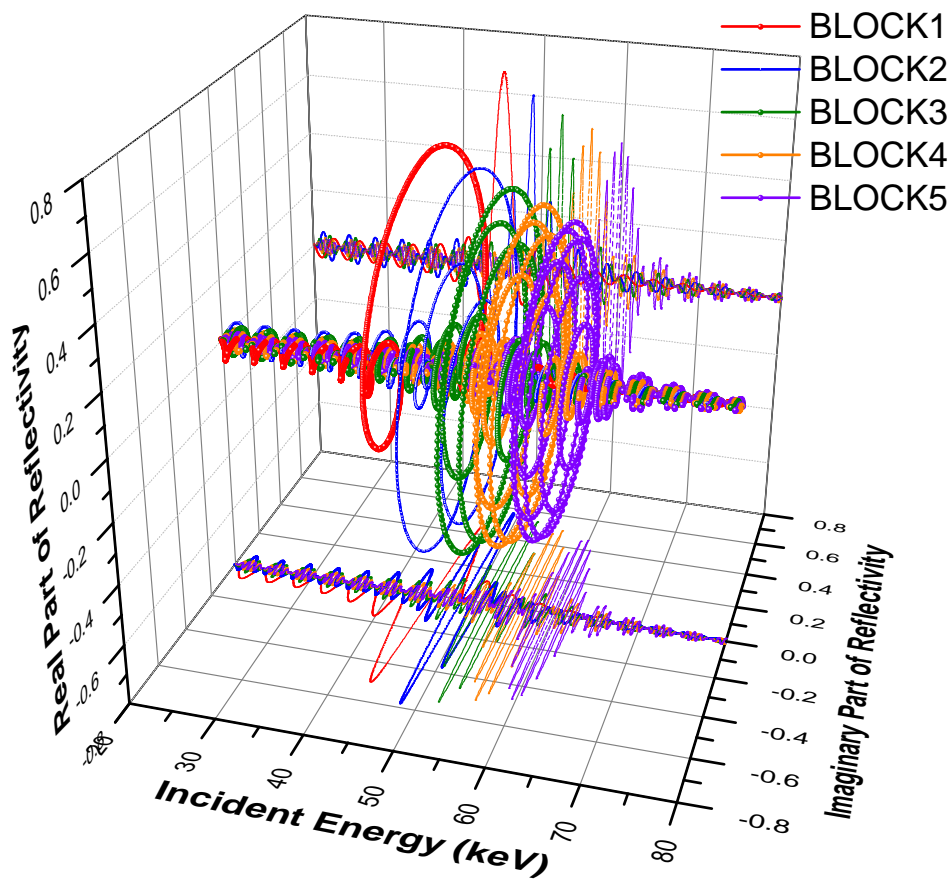


Fig. 2.28. Reflectivity of each block of the structure shown in Fig. 2.27.

As is shown in Figure above, the interference behavior of the reflectivity profiles from each block has been plotted. The sum of all those profiles are the final reflectivity, as is shown in following figure.

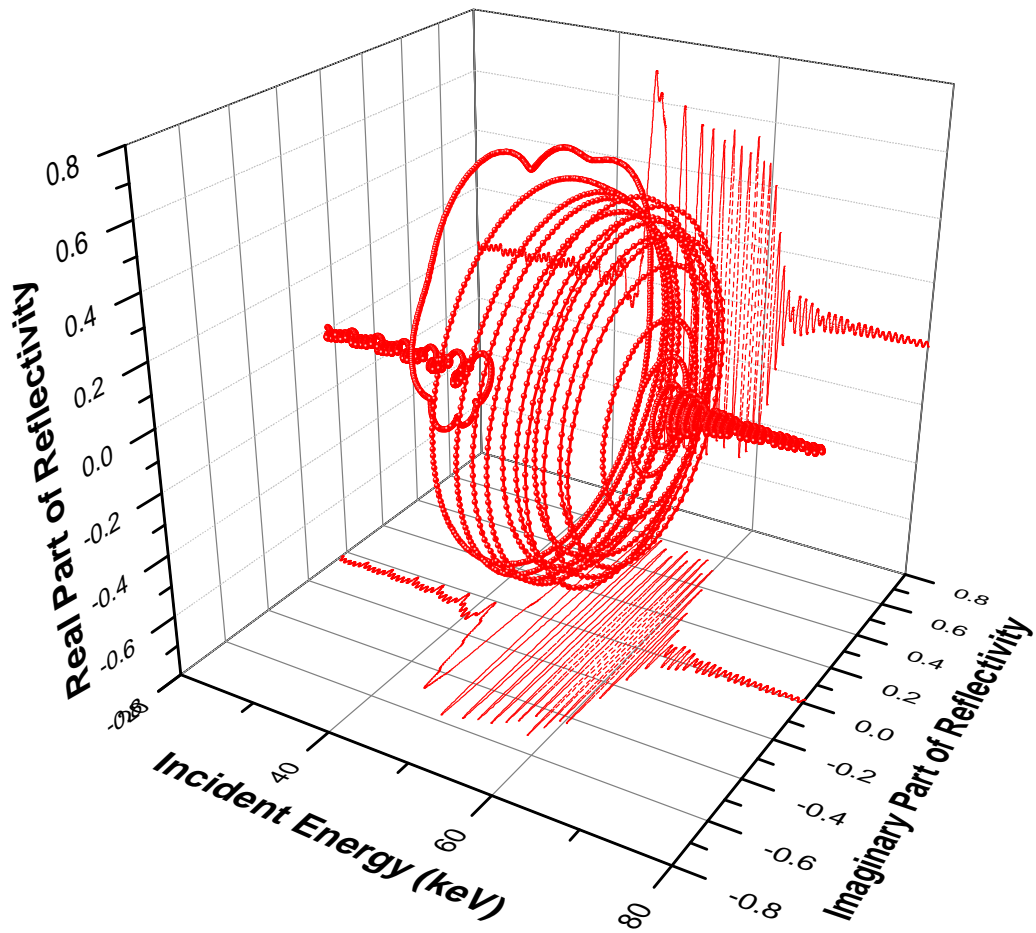


Fig. 2.29. Sum of the profiles in Fig. 2.28. The absolute value of this profile is corresponding to the blue line shown in Fig. 2.28.

As is shown in Figure above, the reflectivity profile is far from our conventional understanding. Conventionally when we design the multilayer, the interference behavior of the X-rays is neglected due to its minor importance for our telescope application. Therefore the complex reflectivity was not studied. However if we really want to design a multilayer structure with smooth profile, some effort should be made to give some constrains. It will be discussed in following section.

2.3 Applications of the simplified Igor's theory

The X-ray propagation behavior in a block structure supermirror has been understood by means of the IGOR's theory and "Vector Model" approximation. However, the most important is how to design a structure. Based on the simplified theoretical approach, I'll introduce a design process to obtain "smooth" reflectivity profile.

In addition, I'll introduce an idea to improve the energy/angular response of a periodic multilayer, based on the equations derived from this theory.

2.3.1 Design of the Block structure supermirrors

2.3.1.1 Design rules and advantage of present theoretical approach

As is shown in Fig. 2.29, the response of a block structure supermirror is very complex. The amplitude reflectivity of each block spins rapidly in the complex plane. Therefore it's very difficult to obtain a design rule from Eq. 2.61 and Eq. 2.62 directly. In order to simplify those equations, I suggest to omitting the spin term (see section 2.2.1) of each block based on two assumptions.

1. The adjacent Bragg peaks are close to each other. Therefore the phase difference is less than 180 degrees
2. For each block, the amplitude of the reflectivity decay quickly out of the Bragg reflection region. Therefore the sidelobe reflectivity is not efficient to donate the final reflectivity profile.

Subsequently, Eq. 2.61 and Eq. 2.62 can be simplified as follows,

$$r(\kappa) = \frac{[\varepsilon_1(k) - \cos^2(\theta)] - [\varepsilon_2(k) - \cos^2(\theta)]}{[\varepsilon_1(k) - \cos^2(\theta)] + [\varepsilon_2(k) - \cos^2(\theta)]} \frac{\kappa}{i\pi} \sum_{j=0}^N \{L_j \text{SINC}[L_j(\kappa - k_j / 2)]\} \quad (2.63)$$

Here, j is the sequential number of block counted from the surface. When analyzing this equation, a very interesting idea occurred.

In Communication Science, there is a very popular transmission theory which is called "OFDM" (Orthogonal Frequency-Division Multiplexing). It is a technology to encode digital data on frequency carriers. As is introduced in this theory, in time domain, when a series of length-limited sinusoidal signal multiplexing with each other, the frequency gap of adjacent signal should be $2\pi/T$, in which T is the total length of the signal. In this case, the signals are "orthogonal" with each other, which mean the minimum interference as is shown in following figures.

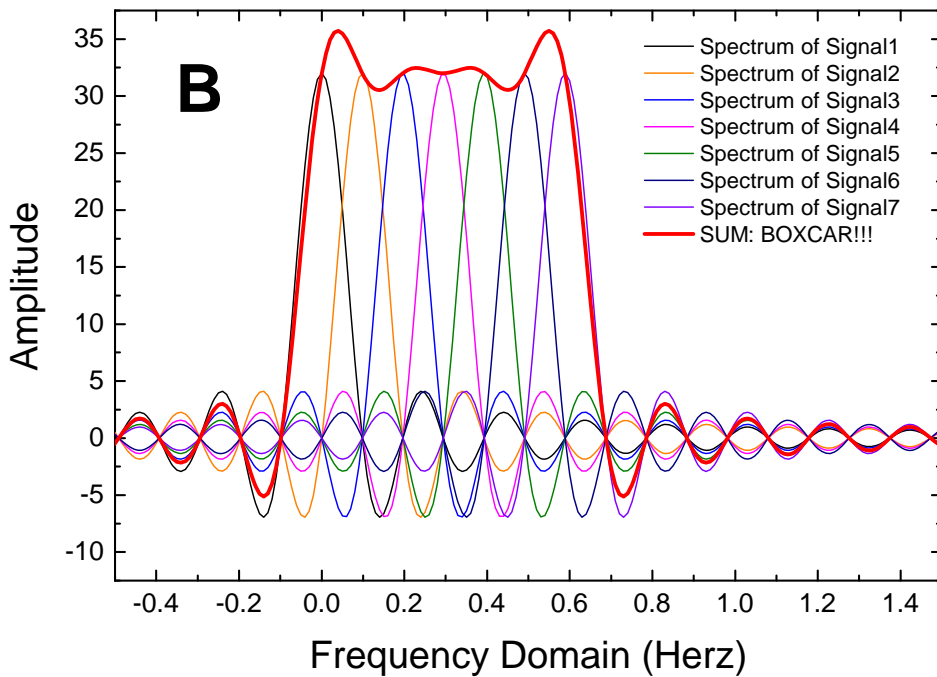
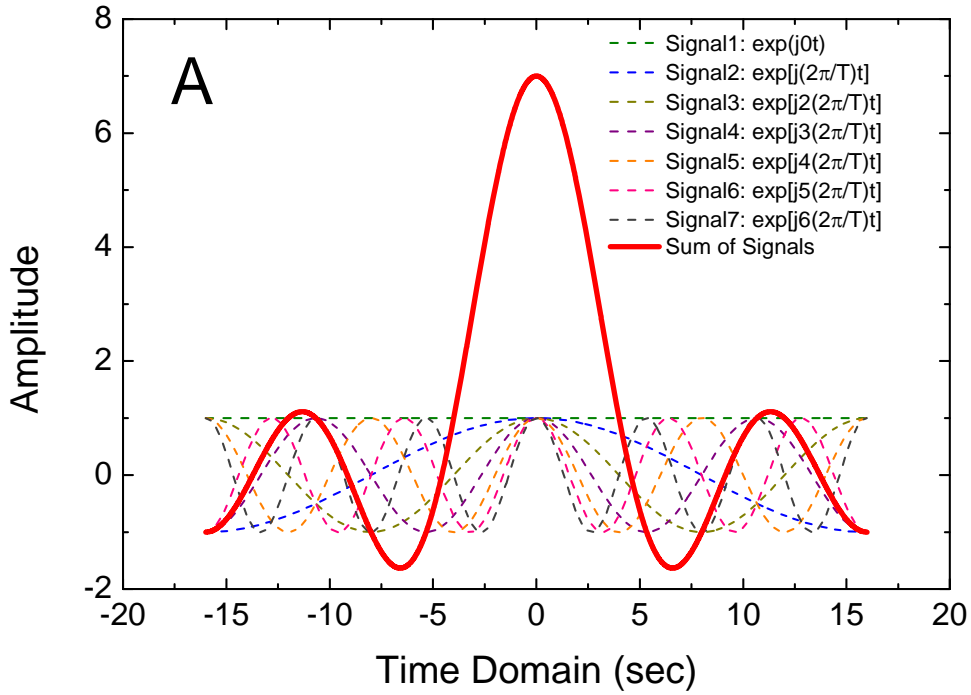


Fig. 2.30. Demonstration of OFDM technology.

As is shown in figure above, in time domain (Panel A), the dash lines correspond to signal series with frequency gap of $2\pi/T$, in which T is the length of the signal (32sec). The red solid line means the sum of all signals in time space. It is a SINC function. In frequency domain (Panel B), the spectrum of each signal overlaps with each other sequentially. The sum of them is a BOXCAR function, shown as red line. It is due to the fact that the BOXCAR function is the Fourier transform of SINC function.

Such conclusion from Communication theory can be applied in our supermirror design. As is

shown in Eq. 2.63, the reflectivity of each block is proportional to a SINC function. The essential of our design is to decide the position and width of the peak of SINC function. If the final spectrum of the multilayer is a BOXCAR profile, then the oscillation should be minimized.

Hence, following the conclusion from “OFDM” theory, I give two design rules to obtain “smooth” reflectivity, presented as follows,

1. The total thickness of each block is equal.
2. The layer number of each block increases incrementally from the top to the bottom.

The structure following the above design rules is presented as follows,

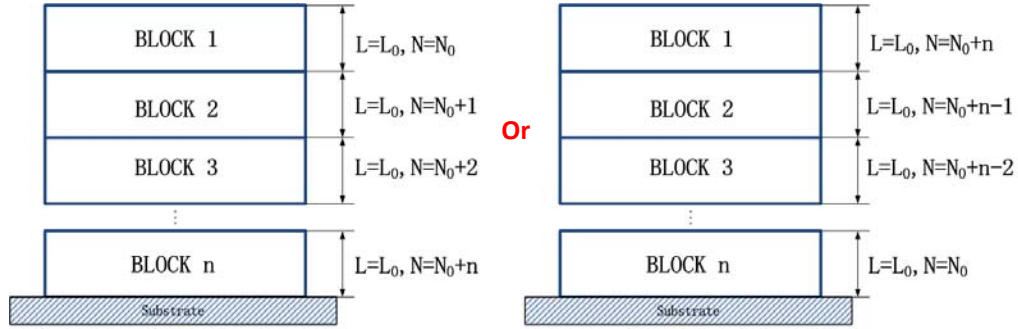


Fig. 2.31. The structure that will provide smooth reflectivity. Here L_0 , N_0 and n are arbitrary parameters which means the thickness of the blocks, the layer number of the first block, and the total number of the blocks. In our experience, whatever they are, the oscillation of the response profile is low (in high energy band $\sim 30\text{keV}$).

If we apply these two new rules, the Eq. 2.62 which describes the interference between blocks can be expressed as follows,

$$\sum_{n=1}^N \mathcal{L}[\text{Block}_n] = \sum_{n=1}^N \frac{1 - \exp(-2\kappa jL_0)}{2\kappa - k_0 - \frac{2\pi(n-1)}{L_0}} \exp(-2j\kappa(n-1)L_0) \quad (2.64)$$

Here, the thickness of each block L_i is the same and equal to L_0 , and the inverse lattice is in the arithmetic series with common difference of $2\pi / L_0$, which suggests the layer number of each block increases with an increment of one.

We assume a structure with 8 blocks. The thickness of each block is set as 50nm ($L_0=50\text{nm}$). The layer number of each block is set incrementally from 17 to 24. The grazing angle is set at 0.28deg. Then, Eq. 2.64 has been calculated and the profile of the spectral function is shown as follows. Eq. 2.63 (OFDM model) has also been calculated to provide a comparison.

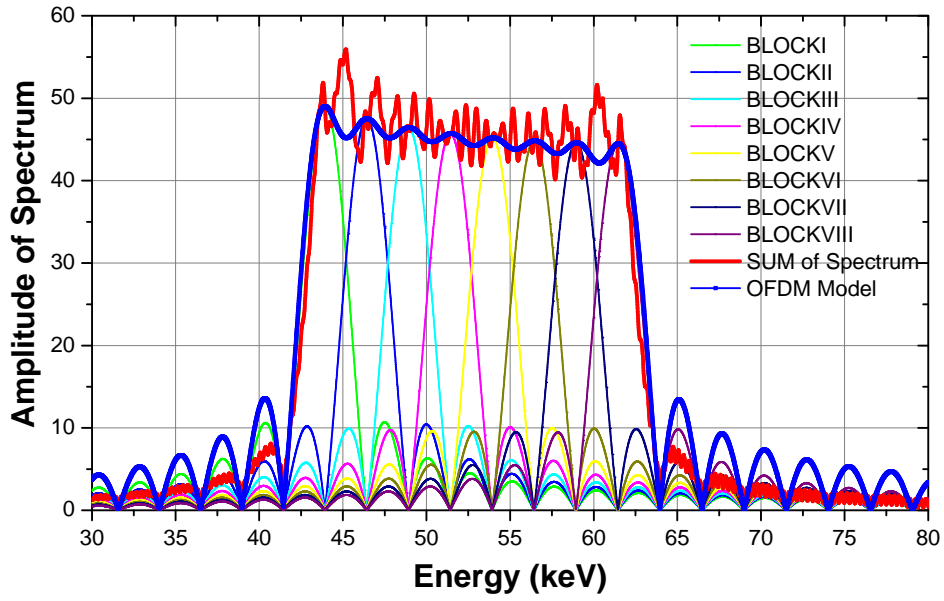


Fig. 2.32. Calculated spectrum of the example structure.

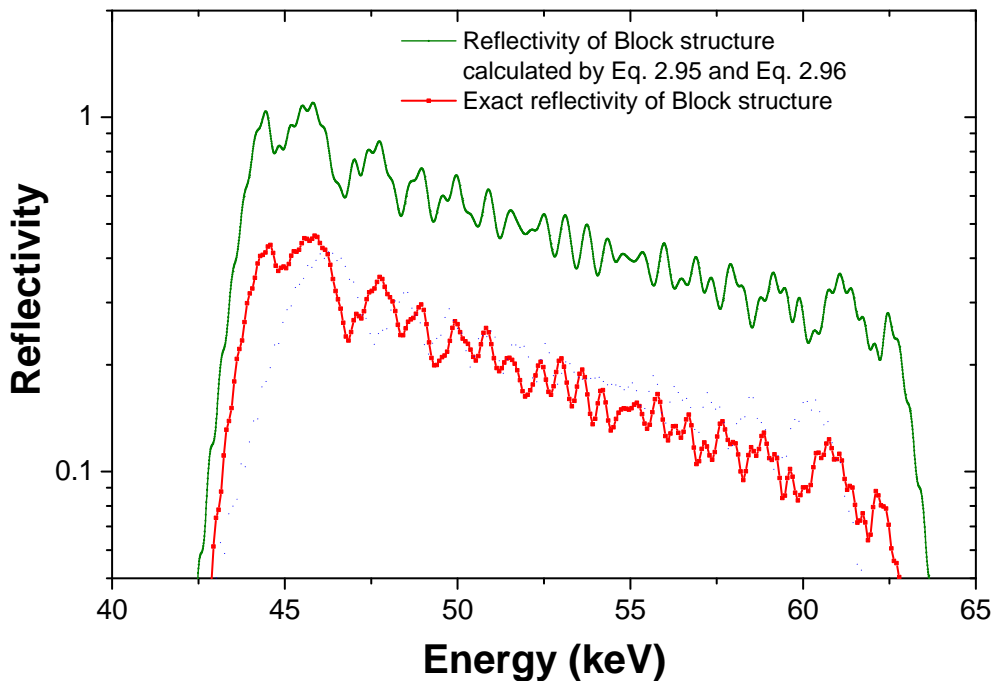


Fig. 2.33 Calculated reflectivity by Eq. 2.61-2.62 (Green line) and Parratt's Algorithm.

In Fig. 2.32, the red line shows the power spectrum of the whole block structure. The power spectrum of each block is shown by the profile with a different color. Obviously, the nodes of all the profiles coincide. Moreover, the center position of each Bragg peak is located exactly at the position of the node position of adjacent block, which suggests the orthogonal phenomena described in "OFDM" theory. Actually, the blue line is exactly the result from OFDM. It absolutely presents that the "smooth" reflectivity due to the boxcar spectrum.

One major point in this section is the fact that the real reflectivity profile with oscillations can be

directly related to the spectral function of the supermirror structure. If a smooth profile of reflectivity response is required, the boxcar type spectral function shown in Fig. 2.32 should be very promising. Eventually, we can give one possible solution to guide the parameter design of a block mirror.

Another question of the designing process is how to maximize the integrated reflectivity. In hard X-ray band, the absorption is negligible and the reflectivity is always far from saturated with limited number of layer pairs. Therefore if the target band is relatively high, then the integrated reflectivity is always maximized. In order to prove this point of view, a power law structure is designed with the same layer number and design target with the example structure. The design results are shown as follows,

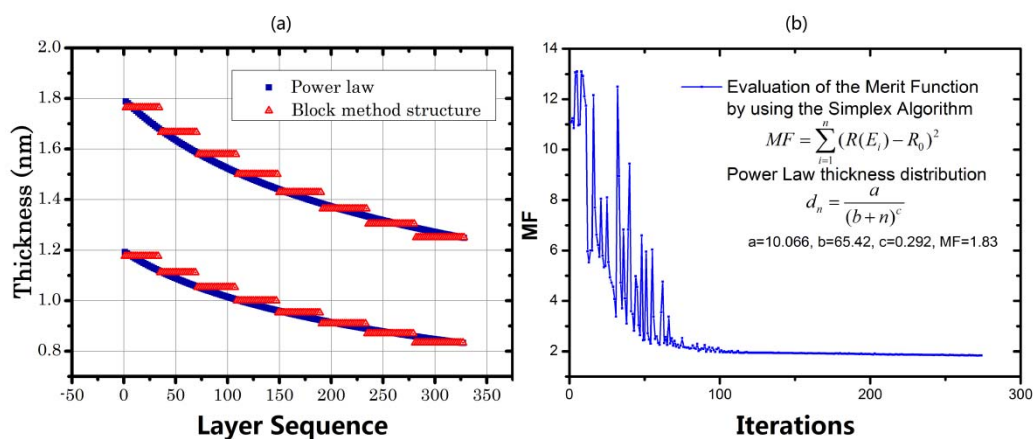


Fig. 2.34. Designed results of the power law structure and block structure. (a) The red line is the thickness distribution of the block structure supermirror, the blue line corresponds to the power law structure. Upper lines correspond to carbon and lower lines correspond to platinum. (b) The evolution of the Merit function of the optimization process of power law structure.

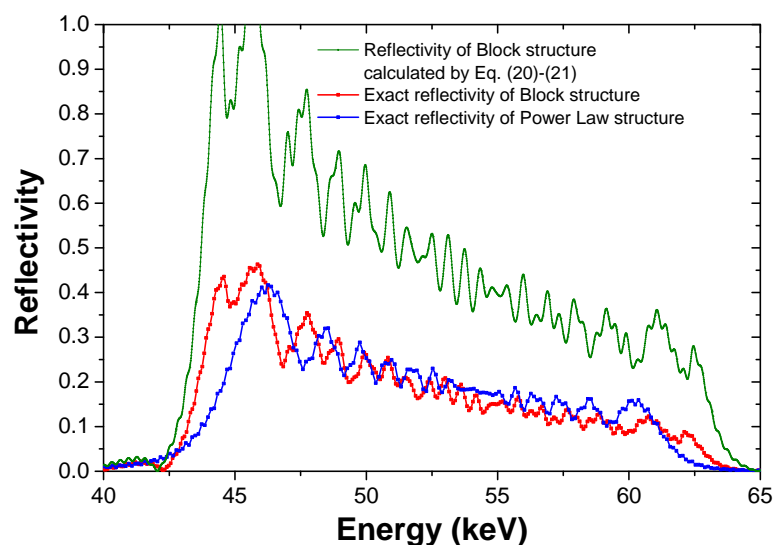


Fig. 2.35. Comparison of the calculated reflectivity. The red line is the reflectivity of block structure calculated by exact method. The blue line is the reflectivity of the power law structure calculated by exact method. Both structures have the same number of layers. The green line is the block structure reflectivity calculated by Eq. 2.61 and Eq. 2.62.

The power law structure is optimized by the simplex algorithm to maximize the integrated reflectivity in target band (N=164, Grazing angle 0.28deg, Roughness 0.4nm). As is shown in Fig. 2.35, the block structure thus designed provides comparable integrated reflectivity with reasonably small ripples as the power law model structure. This result suggests that the design rules introduced in this section are a reasonable guideline to design a block structure supermirror in the high energy band that is easy to be fabricated for real applications, or as the initial structure for computer optimization. So, it is important for hard X-ray telescopes and other potential application in future.

2.3.1.2 Relationships with the empirical rules of block-structure

As is mentioned in previous sections, the block structure has been widely applied in telescopes. Researchers used to find the relations of the parameters between blocks: $d \cdot Ni = \text{constant}$, may provide smooth reflectivity. This empirical rule is theoretically explained by this thesis.

However the reflectivity profiles are not only decided by the spectrum, but the contrast of the materials as well. In low energy band, the contrast of the material is much more significant than that of high energy band. Therefore if we keep the design rules introduced above, the reflectivity profile will be too steep to be acceptable.

However, the design rule is a very good starting point for design. In following figure, the layer number of each block increases sequentially to get lower oscillation of the reflectivity. And then the d-spacing is adjusted to reduce the reflectivity in low energy band.

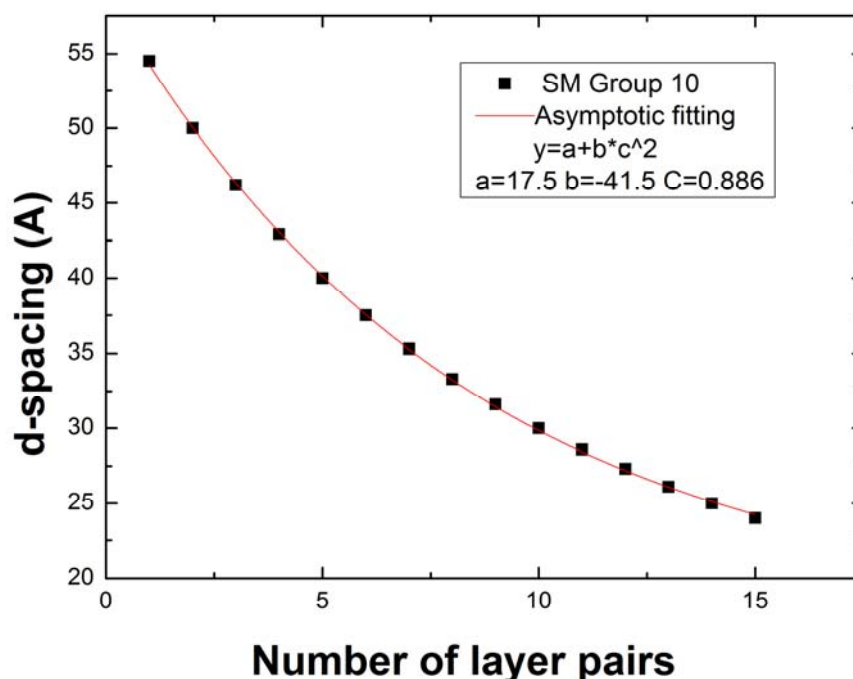


Fig. 2.36. Parameters of a block structure supermirror for ASTRO-H, Supermirror Group 10. The total thickness of each block is adjusted to prevent reflectivity from saturation. However, the layer number of each block still increases sequentially to promise small oscillation.

2.3.2 Design of the Side lobe suppressed multilayer mirrors

2.3.2.1 Relations between Window function and sidelobes

In this section, I'll present another application of my theoretical study —side lobe suppression technology. This technology may not have strong correlation with the X-ray telescope. However, it is very useful for Ground based X-ray optics.

The side lobes are the reflectivity peaks beside the Bragg peak, as is shown in following figure.

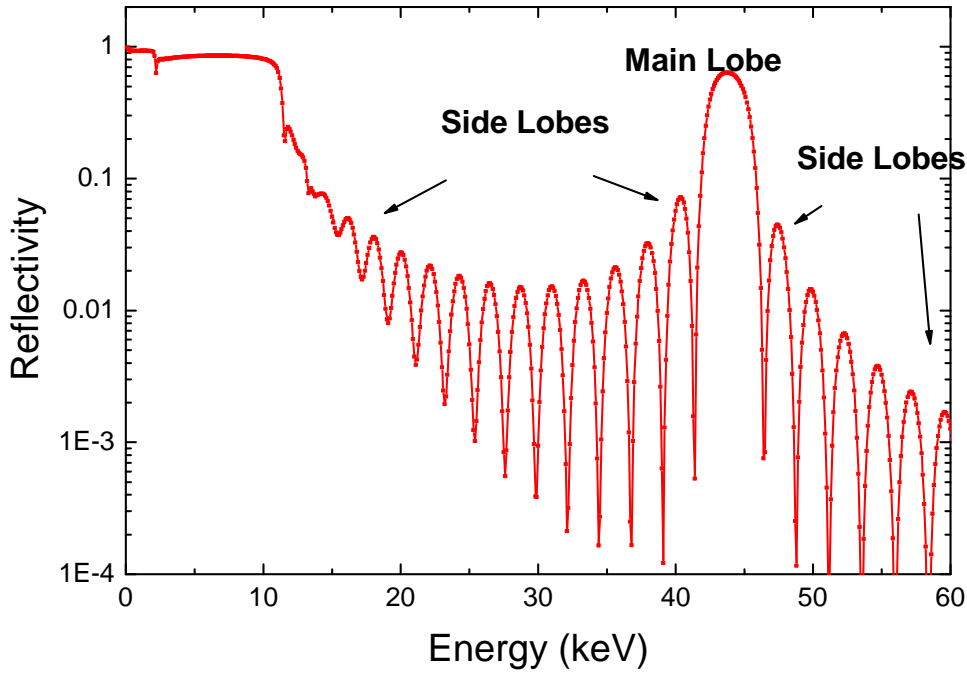


Fig. 2.37. Demonstration of Side lobe peaks.

Figure above presents a reflectivity profile of a periodical multilayer. The Bragg peak is called “main lobe”. The Kiessig fringes are called “side lobes”. As is known to all, the multilayer is very useful for X-ray optics due to the fact that it can pick up signals and provide semi-monochromatic X-rays by means of the Bragg peak. However, not only the main peak of response (Bragg peak) but the side lobe can add useless reflectivity, which is a disadvantage for applications. For X-ray spectroscopy, the multilayer has been used to create high intensity incident X-ray beam from synchrotron radiation by means of Bragg peak reflection while the side lobe may provide noises as well (X-rays caused by the side lobe can be reflected by the sample). In the plasma diagnosis, the multilayer can pick up the interested emission lines, but the noise reflected by the side lobes may disturb the analysis result. Subsequently, the suppression of the side lobes has strong impact from a practical point of view.

In previous sections, the reflectivity profile of a periodical multilayer has been described by Eq. 2.59. The side lobes of reflectivity profile correspond to the side lobe of a SINC function, as is written below

$$\begin{aligned}
 r(\kappa) &= |r(\kappa)| \exp[i\phi(\kappa)] \\
 &= \frac{[\varepsilon_1(k) - \cos^2(\theta)] - [\varepsilon_2(k) - \cos^2(\theta)] \frac{\kappa L_0}{i\pi}}{[\varepsilon_1(k) - \cos^2(\theta)] + [\varepsilon_2(k) - \cos^2(\theta)] \frac{\kappa L_0}{i\pi}} \text{SINC}[L_0(\kappa - k_0/2)] \times \exp[i(-L_0 - 2z_0)\kappa]
 \end{aligned} \tag{2.65}$$

Actually, Eq. 2.65 is derived from Eq. 2.50. If we just consider the first order Bragg peak, the equation is written as follows.

$$r(\kappa) = \frac{ik^2}{4\kappa} B_1 \exp(-i\pi\Gamma) \mathcal{L}[\exp(-i2\pi y(z)) \Big|_0^L]$$

$$\kappa = k\sqrt{\mu - \cos^2(\theta)} \tag{2.66}$$

$$\mu = \Gamma\varepsilon_1 + (1-\Gamma)\varepsilon_2, \quad B_n = 2(\varepsilon_1 - \varepsilon_2) \frac{\sin(\pi n\Gamma)}{\pi n}$$

The SINC function in Eq. 2.65 is corresponding to the Laplace transform of an exponential term in Eq. 2.66. If the total thickness L of a multilayer is infinity, then the Laplace term should be a Dirac function, no oscillations should exist in reflectivity profile. As has been discussed in communication theory, the limited total thickness can be considered as a boxcar window function, which produces side lobes and consequently oscillates the reflectivity profile. Moreover, if the boxcar window function is replaced by a Gaussian window, the side lobes could be significantly suppressed, as is described in following equations and figures.

We firstly assume an exponential function $f(x)=\exp(ikx)$ times a window function $g(x)$. The Fourier transform of $f(x)$ can be expressed as

$$F(k) = \mathcal{F}[g(x) \cdot f(x)]$$

$$= \mathcal{F}[g(x)] \otimes \mathcal{F}[f(x)]$$

$$= \mathcal{F}[g(x)] \otimes \delta(k)$$

$$= \mathcal{F}[g(x)] \tag{2.67}$$

In which \otimes means convolution. $\delta(k)$ is a Dirac function.

When $g(x)$ is a boxcar window, the Fourier transform of $g(x)$ should be a SINC function. Side lobes oscillate the reflectivity shown in Fig. 2.37.

However if $g(x)$ follows Gaussian distribution (Gaussian window), the Fourier transform of $g(x)$ should also be a Gaussian function. Therefore the side lobes in k-space can be suppressed.

Following figures present the difference between a Boxcar window and Gaussian window.

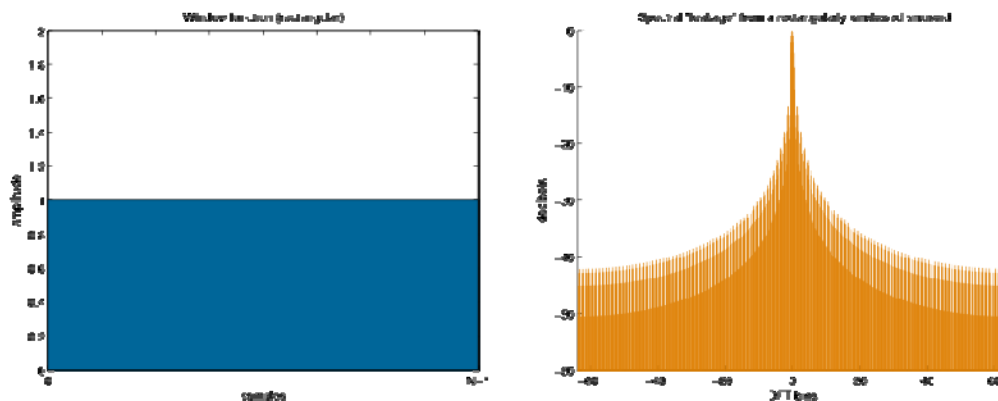


Figure 2.38. A boxcar window in real space (Left Panel) and its corresponding spectrum in k-space (Right panel).

From "http://en.wikipedia.org/wiki/Window_function".

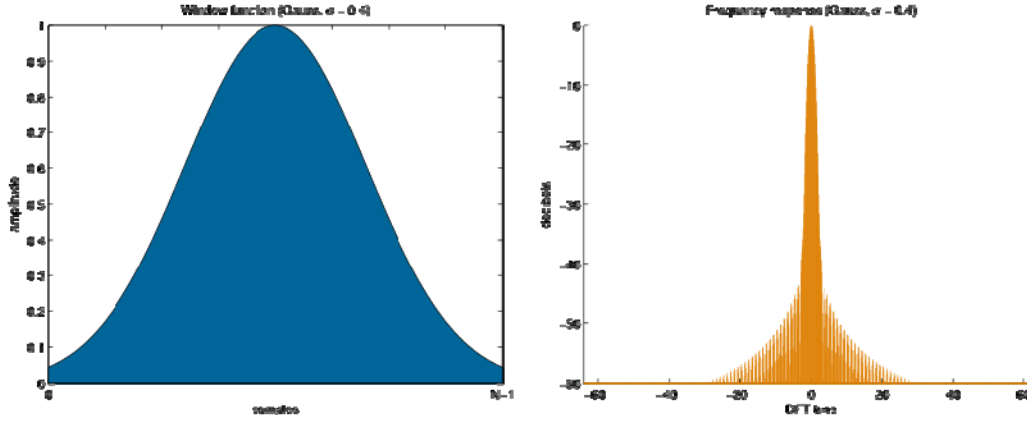


Fig. 2.39. A Gaussian window in real space (Left Panel) and its corresponding spectrum (Right Panel).

From "http://en.wikipedia.org/wiki/Window_function".

As is shown in figures above, the Gaussian window can significantly suppress the side lobes in K-space. Therefore, if we apply this method in Eq. 2.66, then the side lobes of the multilayer reflectivity should be eliminated.

2.3.2.2 Gaussian distribution to suppress side lobes of reflectivity profile

In this section, we establish the Gaussian window to achieve our purpose, by adjusting the thickness ratio (Gamma) distribution as is described below.

In Eq. 2.66, the thickness ratio Γ is fixed to promise a unified mean dielectric constant μ in the multilayer structure. Here we assume that Eq. 2.66 is still correct when Γ varies layer by layer, since the dielectric constants of layer pairs in X-ray band are close to 1, consequently μ is independent from varying Γ .

In Eq. 2.66, the term $B_n \exp(-i\pi\Gamma)$ is placed in front of the Laplace transformation sign due to the assumption that Γ is constant. When Γ varies for layer pairs, that term should be placed in front of the periodical exponential term $\exp(-j2\pi y(z))$.

Therefore, the reflectivity can be derived as follows,

$$r(\kappa) = \frac{ik^2(\varepsilon_1 - \varepsilon_2)}{2\pi\kappa} \mathcal{L}[\sin(\pi\Gamma(z)) \times \exp(-i\frac{2\pi}{d}z - i\pi\Gamma(z))] \Big|_0^L \quad (2.68)$$

Here the sinusoidal term $\sin[\pi\Gamma(z)]$ is considered as a window function. If it follows a Gaussian distribution, then it should be a Gaussian window. In fact, Γ discretely varies for layer pairs. Therefore, we introduce a discrete window function to simulate the continuous one, varying for layer pairs, as following equation.

$$\sin[\pi\Gamma(m)] = \exp\left[-\frac{1}{2}\left(\frac{m - (N-1)/2}{\sigma(N-1)/2}\right)^2\right] \quad (2.69)$$

Here m is the serial number of the layer pair counted from the top and in proportion to the depth. N is the total number of layer pair. Since the window function $\sin[\pi\Gamma(m)]$ discretely follows the Gaussian distribution, σ means the standard deviation to be determined. If σ is infinity,

Γ is fixed at 0.5. However, if σ is close to 0, Γ may evolve quickly with layer pairs (see Fig. 2.41).

As is shown Eq. 2.68, the varying Γ adds an offset on the period of the exponential term. However, when Γ is varying slowly, the tiny deviation may not affect the period of the structure and hence negligible.

We present our procedure to design a side lobe suppressed multilayer. First, determine the d-spacing for target energy band at certain grazing angle. Second, optimize the layer number N to maximize the reflectivity. Third, determine σ to suppress the side lobe of the reflectivity profile. Usually the smaller σ is, the more significant suppression of side lobes. However, a very low σ may lead to a Γ that is close to 0 or 1 at the boundary of the structure. Subsequently the layers would be too thin to fabricate. In our case (Pt/C multilayer), the lower limit of the layer thickness was set at 0.6nm, which helped us to determine the best value of σ , as 0.7 for example.

In order to demonstrate the validity of our design procedure, side lobe suppressed structures have been designed for typical X-ray band. The d-spacing was set at 5nm, sigma were determined at 0.7, 1.0 and $+\infty$ (standard multilayer), grazing angle was fixed at 0.7deg, number of layer pairs were set at 20 and 30 for comparison. The calculated reflectivity profiles are shown in Fig. 2.40.

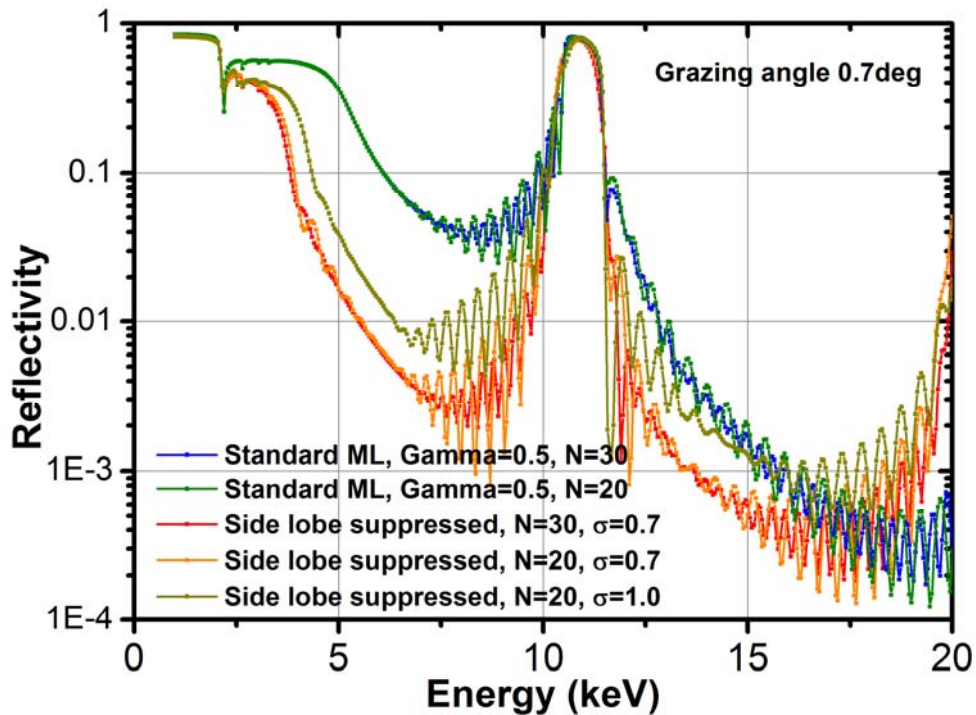


Fig. 2.40. Reflectivity profiles of the side lobe suppressed multilayers and standard multilayers. The side lobes are successfully suppressed when σ is equal to 0.7 and 1.0. Although the reflectivity become saturated when the number of the layer pairs is 20, the profiles of the side lobes are alleviated better when the layer pairs is achieved 30.

The side lobes of the reflectivity profiles are significantly suppressed when the thickness ratio $\Gamma(z)$ follows the distribution mentioned in Eq. 2.69. When the sigma are set at 0.7 and 1.0, the thickness of the thinnest layer at the boundary of the structure are corresponding to 0.6nm and 1.2nm. It was eventually determined at 0.7 for our fabrication ability and better suppression. The

number of layer pairs was determined at 30 due to the fact that the side lobes can be alleviated better. When the incident energy is over 18keV, the reflectivity of the side lobe suppressed sample is higher, since the gamma of the standard multilayer is 0.5, which suggests a vanish phenomenon for 2nd order Bragg peak. However, the first order Bragg peak reflectivity is more crucial for the applications. Moreover, comparing with the side lobes around the first order Bragg peak, higher order Bragg peaks are far away in energy space. Therefore, it can be distinguished by the detectors with energy resolutions or prohibited by a selected filter with proper absorption edges. Subsequently the suppression of the second order Bragg peak is not under consideration.

The thickness ratio Γ is defined between 0 and 1. The solution of $\Gamma(m)$ for Eq. 2.69 could be monotonically increasing, decreasing or strongly oscillation. In this work, the thickness ratio distribution against the layer number m is determined to be monotonically increasing due to three facts listed as follows,

1. Fabrication difficulty can be reduced once the thickness of each layer evolves slowly against the layer number m .
2. Total reflection part of response can be minimized by means of the low average density at the top of the structure.
3. The monotonically increasing $\Gamma(m)$ is close to a linear function which may not strongly offsets the period of exponential term as is described in Eq. 2.68.

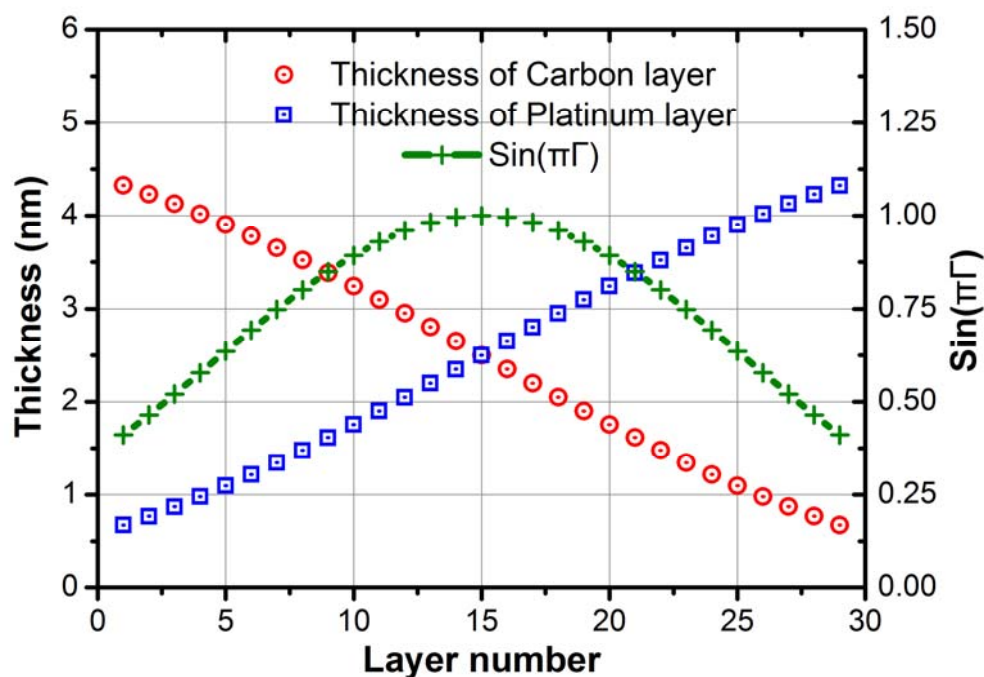


Fig. 2.41. Thickness distribution (red open circle and blue open square) and the window function (green cross) of the side lobe suppressed structure, corresponding response is shown in red line in Fig. 2.40.

The thickness distribution of the designed multilayer and the constructed window function for the layer number m are shown in Fig. 2.41. The X-axis is corresponding to the layer number counted from the top. The red and blue marks mean the thickness of carbon and platinum layers which are corresponding to the Y-axis on the left side. The green marks stand for the window function which follows the Gaussian distribution. The corresponding value is shown via the Y-axis on the right side. In this structure, the thickness evolved gradually against the layer pair numbers. The smallest thickness is 0.6nm, which is determined by our fabrication ability.

The design method introduced above can provide multilayer structures of which the side lobe reflectivity can be significantly suppressed. Such multilayer is better than conventional design and has potential applications in future

In order to demonstrate the validity of designed structure, several samples have been fabricated. The fabrication and testing results will be introduced in Chapter 4.2.3.

Chapter 3.

Numerical design of the Supermirrors

3.1 Introduction -- Goal of the design

In previous chapters, multilayer design are all based on physics model which produce the supermirror structure with a continuous or block structure thickness distribution. In those supermirror structures thus designed, however, solutions should be found for the following problems. First, the oscillations of the reflectivity profiles are relatively large (~50%, see Fig. 1.14 and Fig. 1.17). Although the ripples of the final response can be smeared by the reflection of many mirror shells (grazing angle changes gradually), residual complex structure still could be found which is demonstrated in following figure.

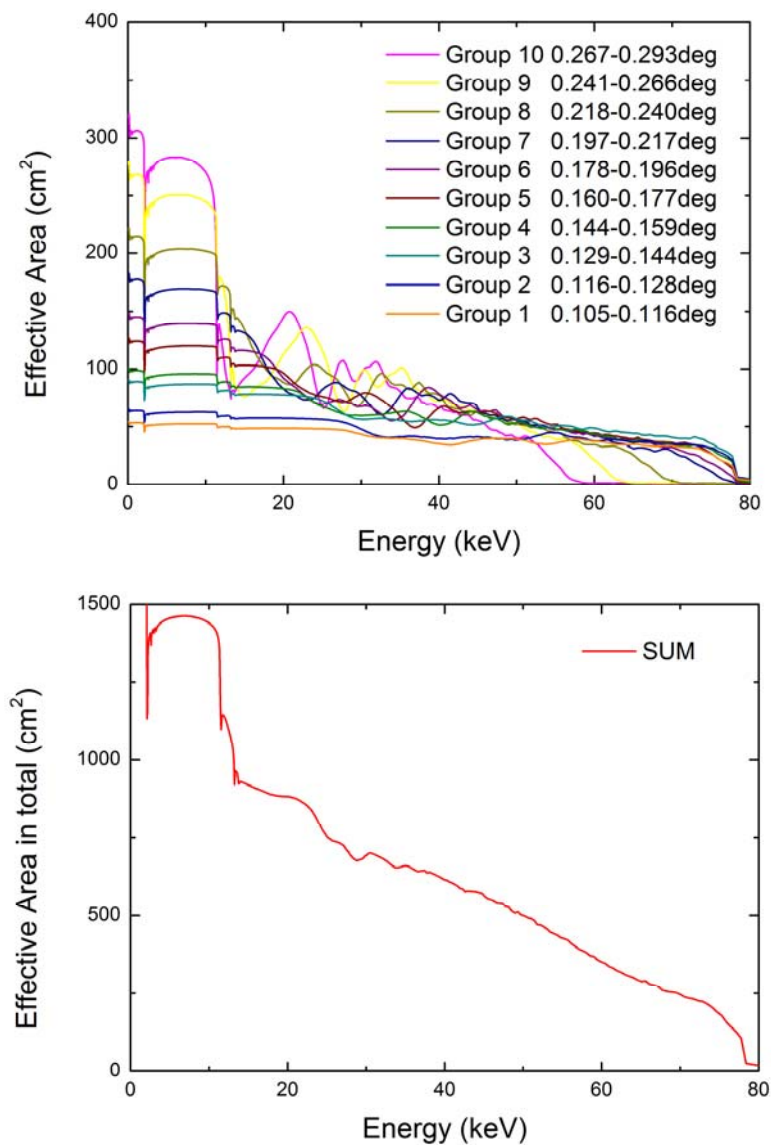


Fig. 3.1. Demonstration of residual complex structure in the response of hard X-ray telescope (one reflection).

Figures above are simulation results for ASTRO-H. There are 10 supermirror groups designed for the telescope. For each group there are ~20 mirror shells. Although most of the ripples of final

response are removed by means of integrating the reflection with changing grazing angles gradually, it's still difficult to smooth the profile thoroughly. This phenomenon may inevitably lead to the difficulties in calibration process since we cannot calibrate the telescope thoroughly on the ground (in case of ASTRO-H, only 2 energy points are measured precisely). The calibration by celestial objects is always unstable and suspicious.

Second, all of the current multilayers are designed with declining reflectivity profiles against X-ray energies to get a higher counting rate from distant celestial objects, which have more photons in low energies. At the same time, flat response in a broad energy range is preferable for observing X-ray spectral shapes in a broader X-ray range. In laboratory experiments, reflectors should cover broader incident angles with constant reflectivity without complex structure of the response. We would like to develop a design method applicable to various types of optics for different scientific purposes. For example, a boxcar response against X-ray energies is needed for monochromator optics to obtain constant and featureless reflectivity response only in the interesting band.

In order to address the concerns mentioned above, I present our new insights to improve the performance of the supermirror for hard X-ray telescopes by our procedures to design and fabricate a multilayer supermirror. With this kind of multilayer structure, the reflectivity profiles can be realized with arbitrary slopes, and the integrated reflectivity can be maximized by means of a numerical approach -- computer optimization. In this Chapter, an optimization strategy is selected that allows us to achieve the final structure by two steps. First, as an initial structure, the supermirror structure is to be designed with a simple model such as a power law model. Second, the final structure is to be obtained by optimizing the initial multilayer structure layer by layer to reduce the ripples, minimizing the merit function newly introduced.

With this optimization strategy, we elaborate proper procedures to achieve two non-periodic multilayer supermirror designs which are practically applicable for hard X-ray telescopes and other optics. One is a broad angular bandwidth supermirror with fixed incident energy and another one is a broad energy bandwidth supermirror with fixed grazing angle. In following sections I'll demonstrate how we succeed to achieve our purpose.

3.2 Basic principles of the optimization processes

3.2.1 Optimization strategy

We selected IGOR's method [8] to optimize and design the supermirror structure with target reflectivity profile. He introduced a promising strategy with the combination of a proper initial structure and an appropriate local optimization method. Especially when a proper initial structure is provided, the final supermirror structure based on this initial one to be achieved by the local optimization algorithm converges within similar ranges of parameters. Hence, this optimization strategy is mature and stable to avoid insufficient local minima.

Our application raises additional requirements for X-ray telescopes, compared with conventional applications such as mirrors for X-ray microscopes. For example in previous applications such as HXT of ASTRO-H, the response of the mirrors must be very broad (typically 10keV-80keV in X-ray energy range). Therefore several differences from the conventional procedures have been noticed. Firstly, the power law structure has been considered as an initial structure due to the fact that it can provide reasonable reflectivity in a wide energy range. Secondly, an evaluation procedure should be established to achieve the best design because of the special requirements such as fabrication difficulties, as mentioned below.

The robustness of the response profile for grazing incident angles is important, because the reflectivity of off-axis X-ray beam directly determines the image quality in field of view of telescopes. So the reflectivity profiles for different grazing angles should be calculated to evaluate the stability and validity of the designed structure.

From a practical point of view, fabrication difficulty should be carefully considered since the thickness-controlling precision is very important to realize the designed structures. In order to estimate such problem, the random thickness error (follows Gaussian distribution) is assumed for each layer of the designed structures. The ripples in the reflectivity profile were calculated for different amplitudes of thickness error (sigma of Gaussian distribution). Based on this simulation, it is possible to estimate how much fabrication accuracy is necessary for acceptable ripples of the reflectivity response profile, less than 2%, for example.

Based on our previous study of multilayer coating technology, Pt/C multilayer is suitable for our application [13-15]. The optical constants of those materials were collected from the database of IMD software [16].

3.2.2 Merit Function

In order to estimate the difference from the target reflectivity to the design results, the merit function is defined in following equation.

$$M.F. = \sqrt{\frac{1}{m} \sum_{i=1}^m [R(E_i) - R_{target}(E_i)]^2} \quad (3.1)$$

where E_i is the i -th discrete energy point, $R_{target}(E_i)$ is the target reflectivity profile, while $R(E_i)$ is the calculated reflectivity. m is the number of discrete energy points in the target band. The merit function means the standard deviation of the calculated reflectivity profile from the target. During optimization of the supermirror structure, a selected algorithm prepares various different sets of the parameters and try to find the best reflectivity profile $R(E_i)$ by searching the minimum value of $M.F.$ Thus, the calculated profile should become close to the target profile.

The optimization strategy with merit function is plotted as follows,

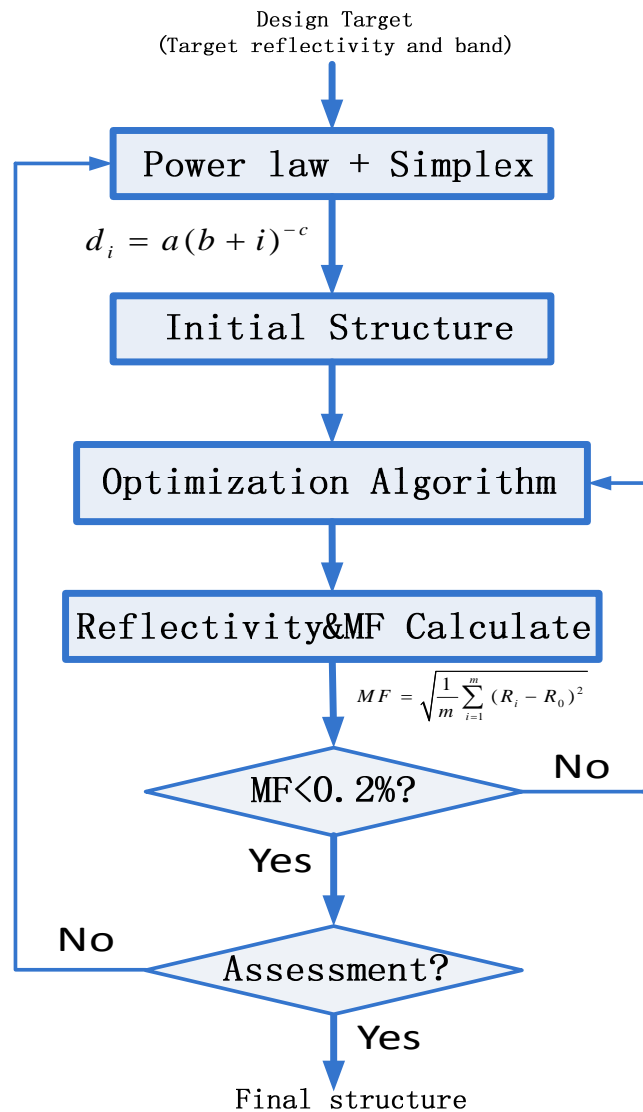


Fig. 3.2 Optimization Strategy for Numerical approach.

3.2.3 Optimization Algorithm

3.2.3.1 Obtaining initial structure by downhill simplex algorithm

The power law structure supermirror is considered as initial structure. Design of the power law structure is the purpose of this section. The power law structure can be expressed by following equation.

$$d_i = \frac{a}{(b+i)^c} \quad (3.2)$$

Where d_i is the thickness of i -th layer counted from the top. a , b and c are three parameters need to optimize. In order to demonstrate the optimization problem clearly, here I present an optimization process for broad angular bandwidth supermirror. Such process can be easily converted to optimize broad energy band case.

The layer number of the structure is N . The corresponding angular band is $[\theta_{\min}, \theta_{\max}]$ at fixed energy of 8.05keV. Obviously, the thickness of the top layer is corresponding to the Bragg reflection at θ_{\min} . That of the bottom layer is corresponding to the Bragg reflection at θ_{\max} .

$$d_1 = \frac{0.154}{2 \sin(\theta_{\min})} nm \quad (3.3)$$

$$d_N = \frac{0.154}{2 \sin(\theta_{\max})} nm \quad (3.4)$$

Three parameters shown in Eq. 3.2 should keep the thickness of all layer pairs within $[d_1, d_N]$ to maximize the integral reflectivity in target band. Meanwhile, those parameters should also promise the thickness distribution providing a response profile follows our design target.

Before the iterations of optimization, we firstly set the boundary conditions: the target band is set from 1.0 to 1.5deg. Layer number is set at 30. Target reflectivity is temporarily set at 50% to estimate highest reflectivity we can obtain. The initial values of those parameters are arbitrarily set as: $a=10$, $b=0$, $c=1$.

We use the simplex algorithm to optimize those three parameters and reduce the M.F. The principle and feature of this algorithm will be demonstrated later. Let's look at the optimization results firstly.

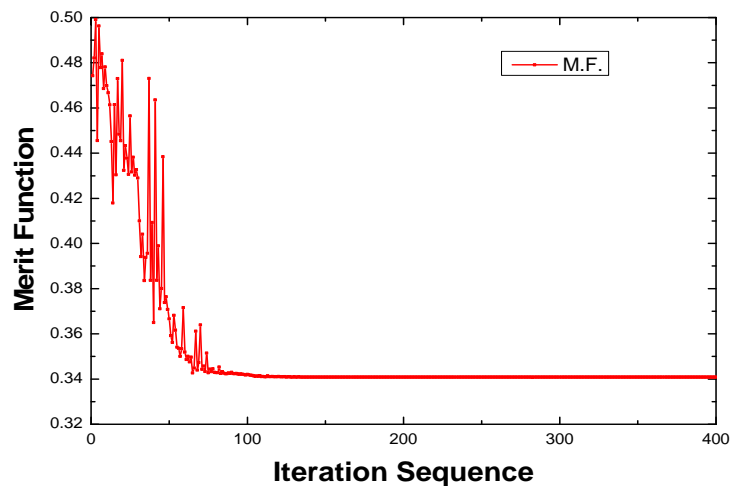


Fig. 3.3 Evolution of Merit Function.

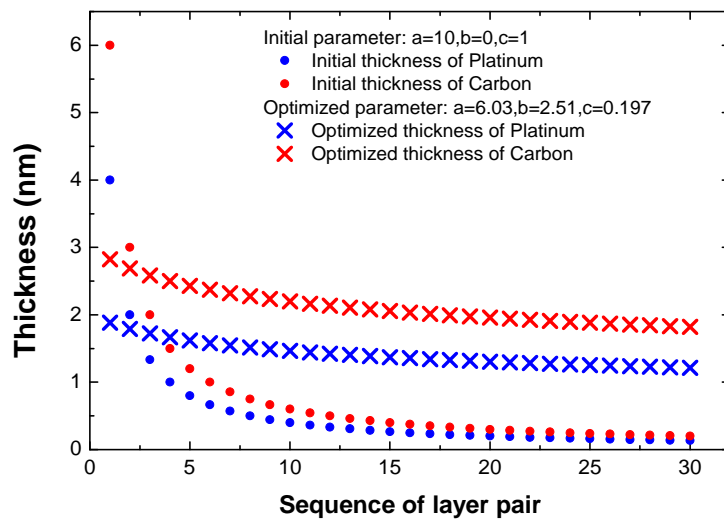


Fig. 3.4. Comparison between the initial and optimized power law structure.

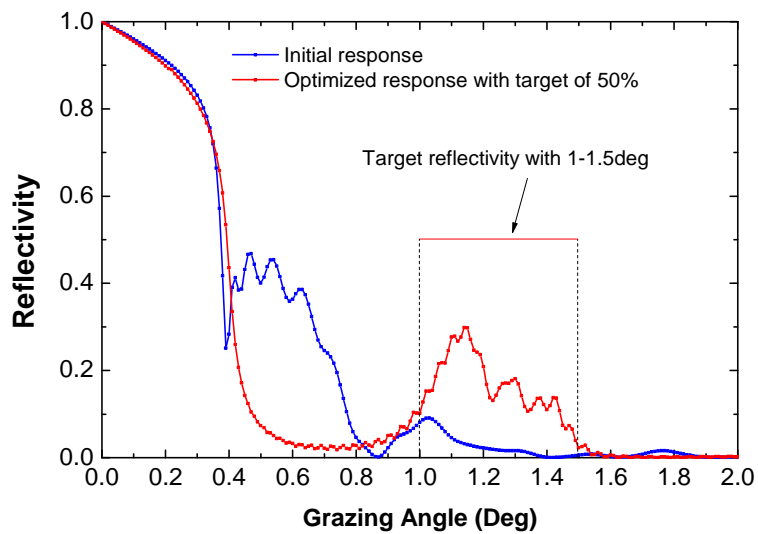


Fig. 3.5. Comparison between the initial and optimized reflectivity profile.

As is shown in Fig. 3.3, the simplex algorithm can significantly reduce the merit function. The initial parameters ($a=10, b=0, c=1$) conduct a M.F. of 48%. After 100 iterations, the M.F. is reduced to $\sim 34\%$. Then, the M.F. cannot be further reduced.

Fig. 3.4 shows the structure before and after optimization (100 iterations). The arbitrary initial parameters ($a=10, b=0, c=1$) conduct a structure (red and blue dots) which covers a very wide d-spacing from 10nm to 0.3nm. From Eq. 3.3-3.4 we calculate the corresponding angular band, which is approximately from 0.5deg to 15deg. It is far away from our design goal (1.0-1.5deg). Subsequently, the least of layers donate the reflectivity within target band. In Fig. 3.4, the blue line demonstrates the poor response profile of the corresponding structure.

The optimized parameters ($a=6.03, b=2.51, c=0.197, 100$ iterations) conduct a thickness distribution which is shown as the cross marks in Fig. 3.4. The thicknesses of the layers at the top and in the bottom of the structure are 4.71nm and 3.04nm, which correspond to an angular band from 0.99deg to 1.49deg. It is consistent with our design goal. And it demonstrates that all the layer pairs donate the reflectivity within target band. Subsequently, red line shown in Fig. 3.5 present a highest level of the reflectivity we can obtain with fixed layer number of 30 (it is consistent with the phenomenon shown in Fig. 3.3, the M.F. cannot be further reduced when the iteration sequence over 100).

In the optimization process above, the layer number was fixed at 30. However, the layer number is correlated with the integral reflectivity in target band we can obtain.

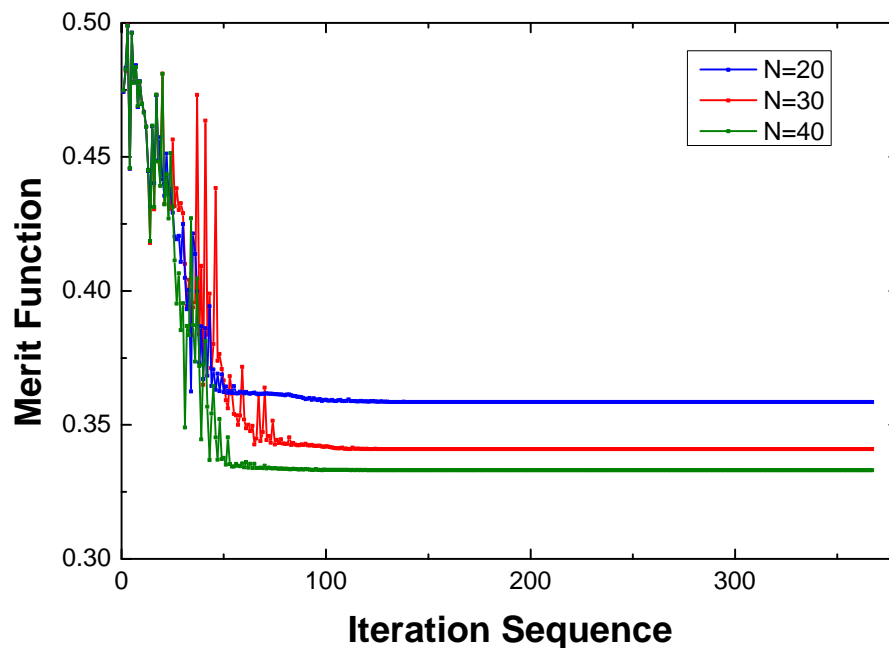


Fig. 3.6. Evolution of M.F with different layer pairs.

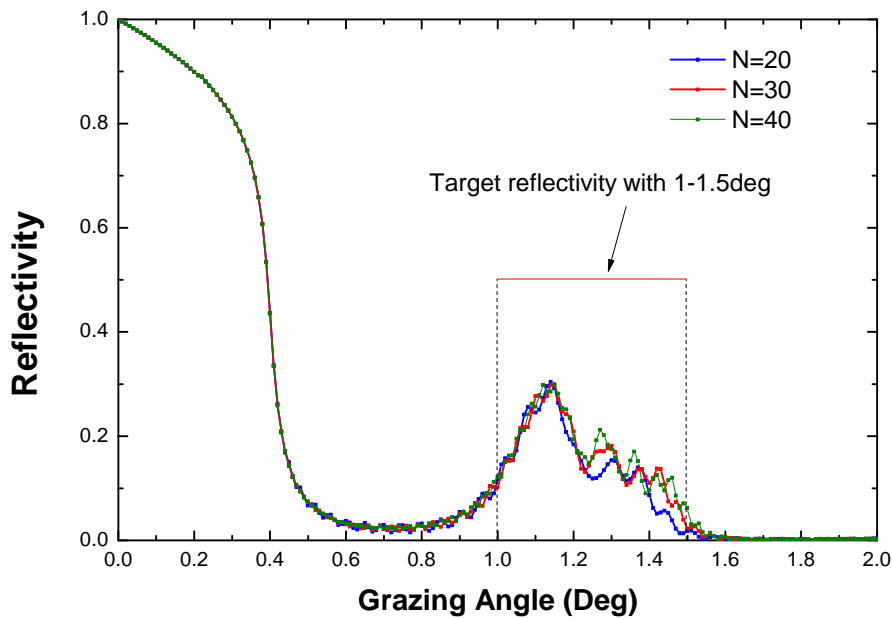


Fig. 3.7. Optimized reflectivity profiles for different layer pairs.

Fig 3.6 shows the evolution of M.F. for different layer pairs. Since in our optimization process the target reflectivity is set at 50%, the higher the layer number the lower the M.F. we can obtain. It is consistent with the reflectivity profiles shown in Fig. 3.7. Obviously, the integral reflectivity enhances a lot when the layer number increases from 20 to 30. However, it's not very different when the layer number increases to 40. Hence, we consider that the reflectivity begin to saturate when the layer number is higher than 30.

Considering the fact:

- 1, All of the layer pairs donate the reflectivity in target band
- 2, The reflectivity profile begin to saturate when the layer number exceeds 30

Conclusion has been made that the optimized structure shown in Fig. 3.4 is the best for our design goal.

Sometimes the flat reflectivity is necessary. But the reflectivity profiles shown in Fig. 3.7 are not flat due to the fact that the target reflectivity was set too high to be obtained. Actually, the average reflectivity we can obtain in target band is ~20% as is shown in Fig. 3.7.

In order to obtain a power law structure with flat top response, we set the target reflectivity at 20% and optimize the structure again,

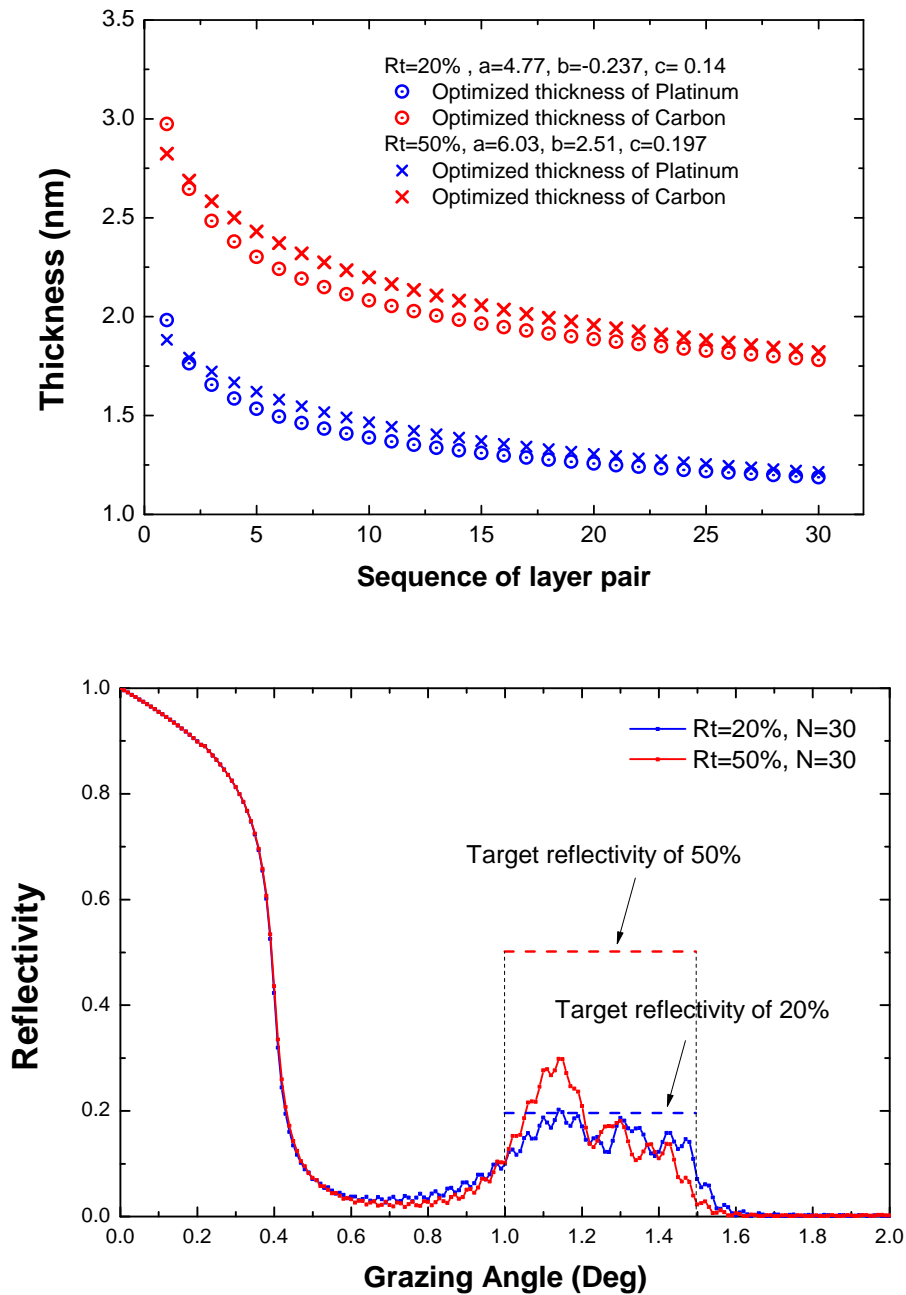


Fig. 3.8. Optimized thickness distribution for different target reflectivity (upper panel) and comparison of the optimized reflectivity profile with different target reflectivity (lower panel).

As is shown in figure above, the optimized reflectivity can be flat when the target is set at 20%. However, the integral reflectivity in target band is reduced. It is because the reflectivity of a single surface at larger grazing angle is lower than that at smaller grazing angle. Flat reflectivity (blue line) requires the enhancement of the reflectivity at larger grazing angle (1.4-1.5deg for example). And total number of layer pairs is fixed at 30. Subsequently the trade-off of reflectivity for grazing angles lead to a different thickness distribution (Shown in Fig. 3.8, most of layer become thinner) and thus reduce the integral reflectivity profile. But still, the blue line presents the highest reflectivity we can obtain. The open circles shown in Fig. 3.8 present the final structure we obtained from this optimization process, which is the initial structure for local optimization.

In summary, the design process is concluded as follows.

1. Following the scientific goal, target angular/energy band should be determined.
2. Set target reflectivity to 50% or higher, optimize the structure with different number of layer pairs, by means of downhill simplex algorithm. Figure out the appropriate layer number N by comparing the integral reflectivity.
3. Check the thickness of the top/bottom layer pair to confirm that all the layer pairs in the structure donate the reflectivity in target band.
4. If you need flat top reflectivity profile, set the target reflectivity to the average level of reflectivity obtained in step 2. Execute the iterations again to optimize the structure.
5. Check the reflectivity profile, output the designed structure as the initial structure for local optimization.

Demonstration of the Downhill simplex Algorithm:

In 1965, John Nelder and Roger Mead proposed this algorithm to minimize a merit function (M.F) in a many dimension-spacing. This algorithm is based on a concept of “Simplex”, which is a special polytype of N+1 vertices in N dimension. A line segment on a line, a triangle on a 2-dimension plane and a tetrahedron in a space of 3 dimensions are all examples of simplex.

For a problem to minimize a merit function with N+1 variables, this algorithm firstly simulate a simplex in N dimensions of which the coordinates of vertices correspond to variables. Then the M.F. at each vertices will be calculated. Following a well designed rule, some of vertices will be replaced by new points and the simplex will eventually contract to a merit point by iterations.

A popular variation of the downhill simplex algorithm is described as follows,

1. Order the corresponding value of the merit function at vertices.

$$MF(X_1) \leq MF(X_2) \dots \leq MF(X_j) \dots \leq MF(X_{n+1})$$

$$\text{In which } X_j = (x_{j,1}, x_{j,2}, \dots, x_{j,n})$$

2. Calculate X_0 , the center of gravity of all points except X_{n+1}

3. Reflection Process

Calculate a reflected point of X_{n+1} , defined as $X_r = X_0 + \alpha(X_0 - X_{n+1})$, in which α is called Reflection Coefficient (typical value is 1). If the M.F. of reflected point is better than the second worst, i.e., $MF(X_n)$, but not the best, then replace X_{n+1} by X_r and return to step

- 1.

4. Expansion Process

If the M.F. of reflected point is the best so far, then calculate an expansion point, defined as

$$X_e = X_0 + \gamma(X_0 - X_{n+1}) \quad . \quad \gamma \text{ is called Expansion Coefficient (typical value is 2). If the M.F. of}$$

expansion point is better than that of reflection point, replace X_{n+1} by X_e and return to step

1. Else, replace the worst point with the reflected point.

Else if the reflected point is still the worst point, then continue to step 5.

5. Contraction Process

In case when $MF(X_r) > MF(X_n)$, calculate a contraction point defined as

$$X_c = X_0 + \rho(X_0 - X_{n+1}),$$

in which ρ is "Contraction Coefficient" (typical value is -1/2). If the

MF of contraction point is better than that of the worst point X_{n+1} , then replace it and

return to step 1. Else, continue to step 6.

6. Reduction Process

For all but best point X_1 , replace them by $X_i = X_1 + \sigma(X_i - X_1)$, in which σ is called

"Reduction Coefficient" (typical value is 1/2). Return to step 1.

In order to demonstrate each step clearly, I assume a 2 dimensions case (2 variables) and the sketch of each step is plotted as follows.

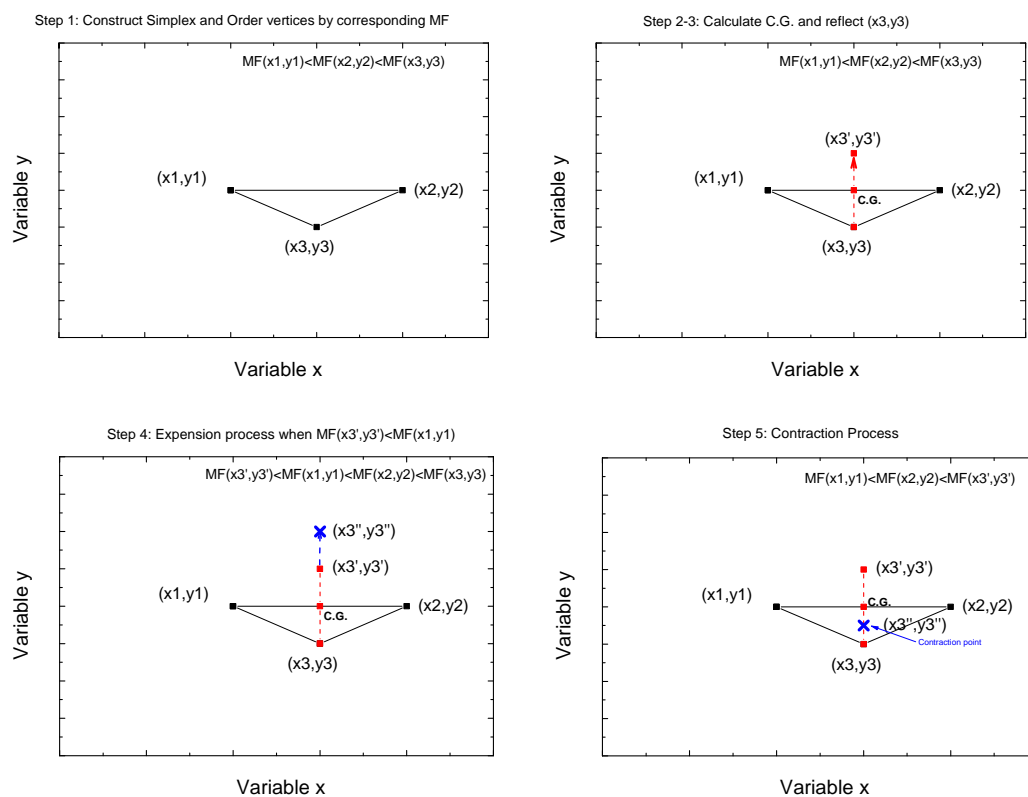


Fig. 3.9. Sketch of a Downhill simplex Algorithm, from step1 to step5.

Since the downhill simplex optimization move the variables toward the gradient direction, this method is very suitable for M.F. varies smoothly and is unimodal. Fortunately, the optimization of the power law structure satisfies this requirement.

3.2.3.2 Reducing the ripples by using Pattern Search algorithm

As has been described in Kozhevnikov's work, ripples of the reflectivity profile can be smoothed out by optimizing the thickness of each layer (Local optimization). A bunch of optimization algorithms are suggested in his paper, such as quasi-Newton, Levenberg-Marquardt and simplex. Since in numerical approach, the physical meaning is lost. Therefore the explanation of numerical approach itself is meaningless. However in this section, based on the initial structure introduced from last section, I'll optimize this structure by simplex algorithm and Pattern Search algorithm. The optimization results will be compared with each other. Conclusions will be made based on thus comparison. The basic principle and feature of Pattern Search algorithm are also attached at the end of this section.

The boundary conditions of local optimization process are described as follows.

1. The structure shown in Fig. 3.7 (open circles) is considered as initial structure.
2. The target band is 1.0-1.5deg, which is the same as introduced in last section.
3. The target reflectivity is temporarily set at 16%, which is corresponding to the average reflectivity within target band shown in Fig. 3.8 (blue line).

The optimization results are shown in following figures.

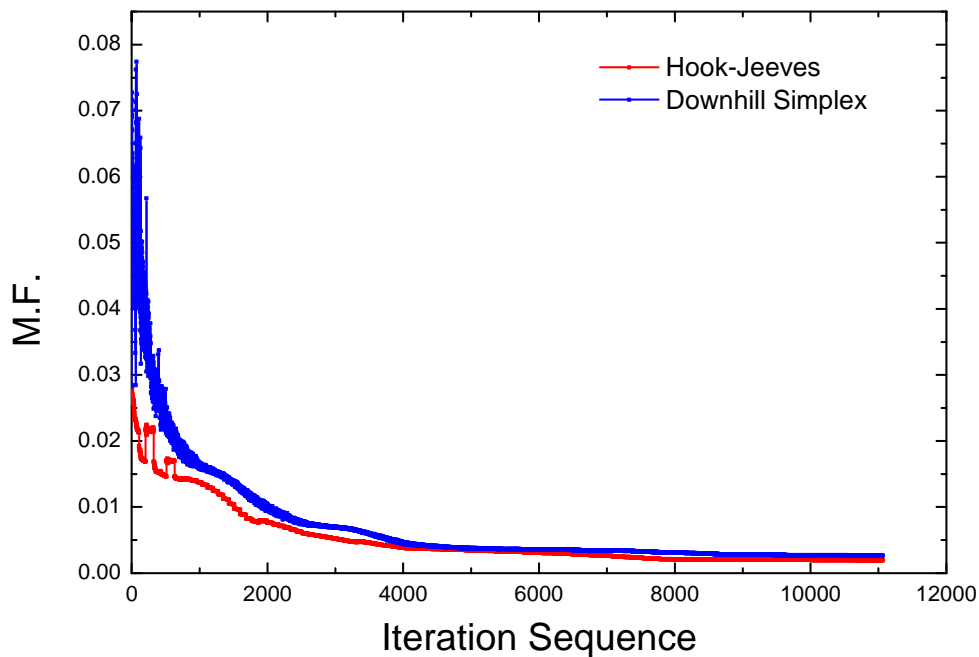


Fig. 3.10 Evolution of the M.F for different local optimization algorithm.

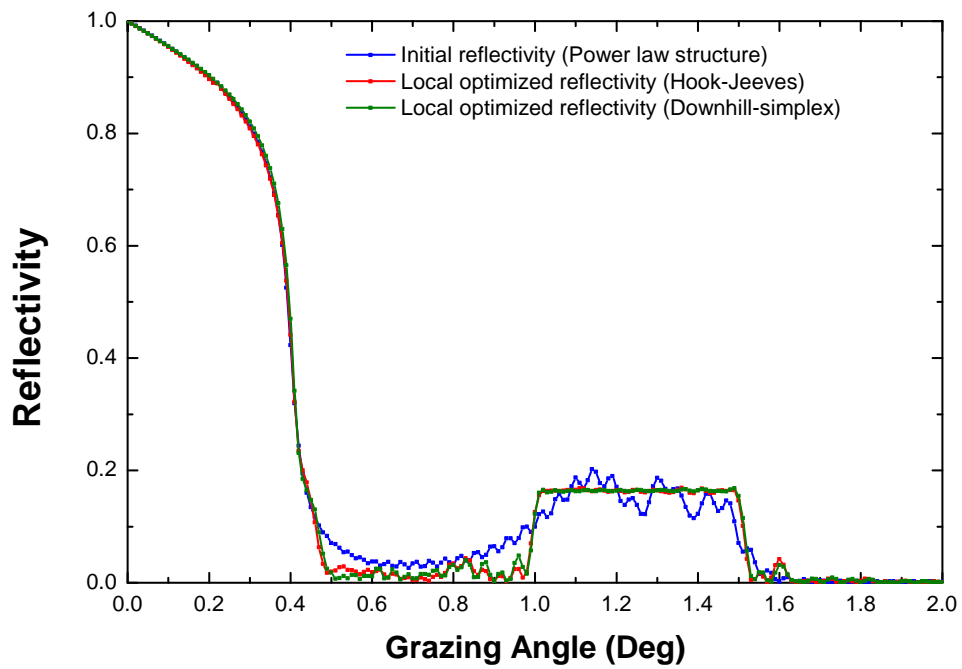


Fig. 3.11. Optimized reflectivity profiles from different optimization algorithm.

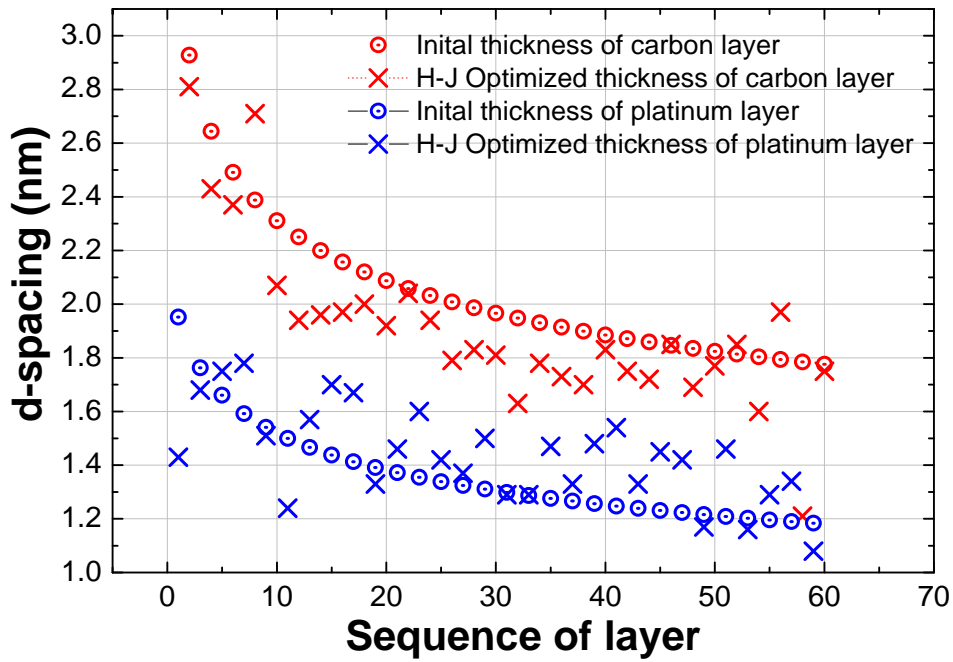


Fig. 3.12. Hook-Jeeves algorithm optimized thickness distribution (cross marks) and power law distribution

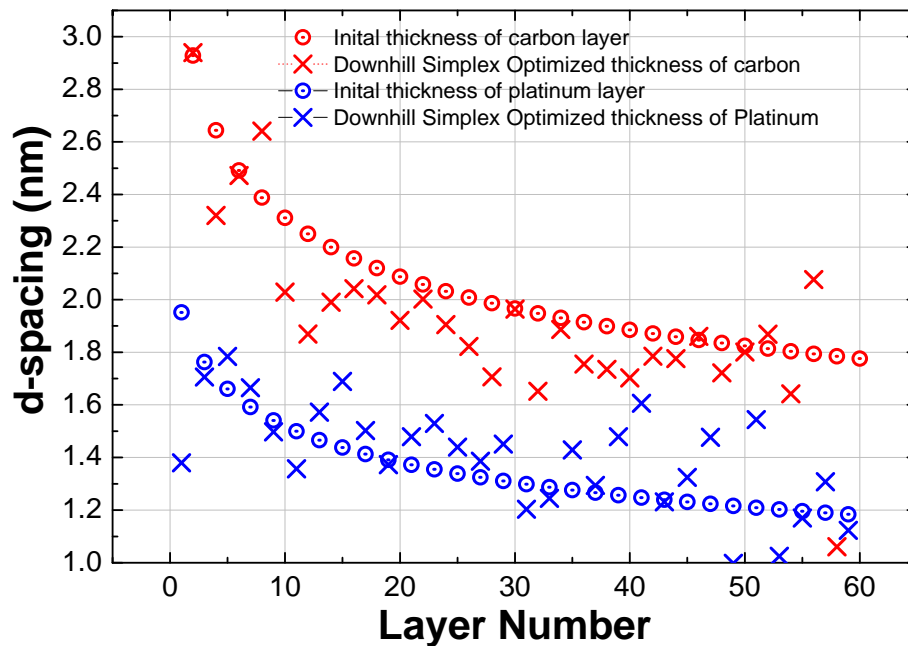


Fig. 3.13 Downhill Simplex algorithm optimized thickness distribution (cross marks) and power law distribution.

As is shown in Fig. 3.10, both of the algorithms can significantly reduce the M.F. by adjusting the thickness layer by layer. It is consistent with Kozhenikov's conclusion in his work. However, the convergence rate is different. The H-J method is faster to obtain the target.

Fig. 3.11 shows the initial and optimized reflectivity profiles. Both of the algorithms can produce a structure with very smooth and flat response profile within target band. It is consistent with the profiles shown in Fig. 3.10.

Fig. 3.12 and Fig. 3.13 demonstrate the thickness distribution optimized by H-J method is very similar with that by simplex method. Both of them vary seriously from initial point.

Considering that high convergence rate is important for us to reduce the optimization time, Hook-Jeeves algorithm has been selected.

Usually, not only the algorithm but the level of target reflectivity may affect the convergence rate and the final M.F.. For example, I use the pattern search method to optimize the thickness distribution with target reflectivity 14%, 16% and 18%, the evolution of M.F. and optimized reflectivity profiles are shown as follows.

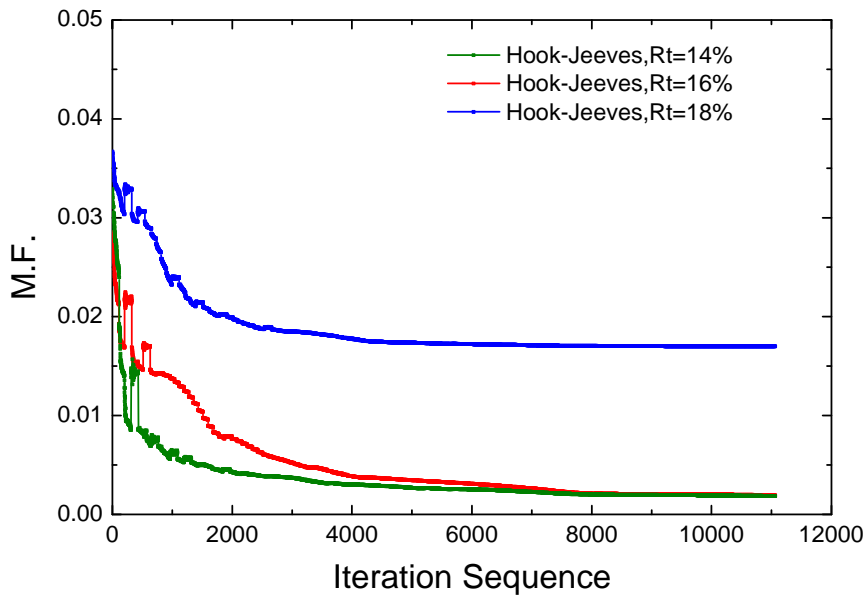


Fig. 3.14. Evolution of M.F. for different target reflectivity

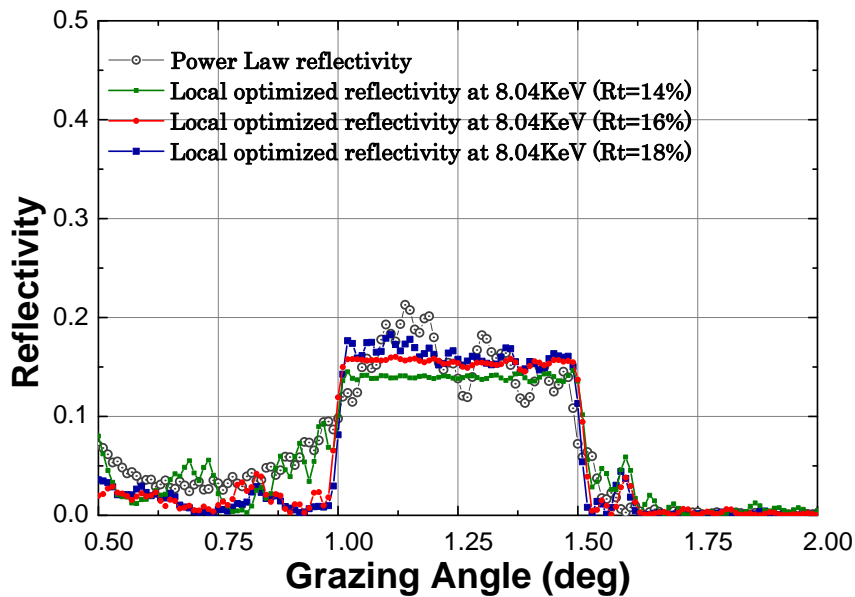


Fig. 3.15. Optimized reflectivity profiles for different target reflectivity.

Different target reflectivity may lead to different optimization result. When the target reflectivity is set at 14%, the convergence rate of M.F. is the highest and the final reflectivity profile we can achieve is very smooth and flat, almost the same as the reflectivity profile with 16% of optimization target. However when the target is set at 18%, the algorithm cannot enhance the level of response profile due to the fact that the target reflectivity exceeds average level of initial reflectivity (Gray line). It is consistent with the M.F. evolution shown in Fig. 3.14(blue line).

In summary , the local optimization process is concluded as follows.

1. The Downhill simplex algorithm and Hook-Jeeves algorithm can smooth the reflectivity profiles by adjusting the thickness layer by layer. But the convergence rates are different. Hook-Jeeves algorithm convergent faster.

2. Target reflectivity should be determined carefully. Usually when optimize the structure, we try different target to confirm the appropriate level.

Demonstration of the Pattern Search (Hook-Jeeves) algorithm:

The Pattern Search optimization was firstly introduced by Hook and Jeeves in 1961. It's a family of optimization method which can find the minimum of M.F. without gradient of the problem. Therefore, Pattern Search can be used to solve the problem which is not continuous or differentiable. The basic principles of the pattern search is described as follows,

1. Initialization

Set an initial point in n-dimension variable space as the beginning of pattern search:

$$X_0 = (x_{0,1}, x_{0,2}, \dots, x_{0,n}) = (x_{1,1}, x_{1,2}, \dots, x_{1,n}) .$$

Define an initial step: s_1 .

Terminate step: ε .

Define step reduction factor: Ra.

Initialize the sequence of pattern move: k=1

Initialize the sequence of variable: j=1

2. Exploratory search

Construct $x'_{k,i} = x_{k,i} + s_{k,i}$ (discrete step in positive direction)

$$\text{If } M.F.(x_{k,1}, x_{k,2}, \dots, x'_{k,j}, \dots, x_{k,n}) < M.F.(x_{k,1}, x_{k,2}, \dots, x_{k,j}, \dots, x_{k,n}) ,$$

set $(x_{k,1}, x_{k,2}, \dots, x'_{k,j}, \dots, x_{k,n}) = (x_{k,1}, x_{k,2}, \dots, x_{k,j}, \dots, x_{k,n})$ and go to step 3. (Successful exploratory)

Otherwise, replace $x'_{k,i} = x_{k,i} - 2s_{k,i}$ (discrete step in negative direction)

$$\text{If } M.F.(x_{k,1}, x_{k,2}, \dots, x'_{k,j}, \dots, x_{k,n}) < M.F.(x_{k,1}, x_{k,2}, \dots, x_{k,j}, \dots, x_{k,n}) ,$$

set $(x_{k,1}, x_{k,2}, \dots, x'_{k,j}, \dots, x_{k,n}) = (x_{k,1}, x_{k,2}, \dots, x_{k,j}, \dots, x_{k,n})$ and go to step 3. (Successful exploratory)

Otherwise, replace $x'_{k,i} = x_{k,i} + s_{k,i}$, (back to original point)

3. Switch to next variable

If $j < n$, set $j = j + 1$ and return to step 2. Otherwise, continue.

4. Terminal condition check

if $s_{k,j} < \varepsilon$ for all variables, end search and output $X_{final} = (x_{k,1}, x_{k,2}, \dots, x_{k,j}, \dots, x_{k,n})$

5. Test for total failure in all directions

If $M.F.(x_{k,1}, x_{k,2}, \dots, x_{k,j}, \dots, x_{k,n}) < M.F.(x_{k-1,1}, x_{k-1,2}, \dots, x_{k-1,j}, \dots, x_{k-1,n})$, continue to step 6.

Else if $M.F.(x_{k,1}, x_{k,2}, \dots, x_{k,j}, \dots, x_{k,n}) > M.F.(x_{k-1,1}, x_{k-1,2}, \dots, x_{k-1,j}, \dots, x_{k-1,n})$,

set $(x_{k,1}, x_{k,2}, \dots, x_{k,j}, \dots, x_{k,n}) = (x_{k-1,1}, x_{k-1,2}, \dots, x_{k-1,j}, \dots, x_{k-1,n})$, return to step 2.

Else if $M.F.(x_{k,1}, x_{k,2}, \dots, x_{k,j}, \dots, x_{k,n}) = M.F.(x_{k-1,1}, x_{k-1,2}, \dots, x_{k-1,j}, \dots, x_{k-1,n})$, set $s_{k,j} = s_{k,j} * Ra$ and return to

Step 2.

6. Pattern Move (Extrapolation search)

$$\text{Set } (x_{k+1,1}, x_{k+1,2}, \dots, x_{k+1,j}, \dots, x_{k+1,n}) = (2x_{k,1}, 2x_{k,2}, \dots, 2x_{k,j}, \dots, 2x_{k,n}) - (x_{k-1,1}, x_{k-1,2}, \dots, x_{k-1,j}, \dots, x_{k-1,n})$$

$s_{k+1,j} = s_{k,j} * \text{sign}(x_{k1,j} - x_{k-1,j})$ for all variables.

set $k=k+1, j=1$

return to step 2.

In order to demonstrate the search method clearly, a sketch of pattern search is given in 2-dimension variable case. The corresponding list of demonstration is also attached below.

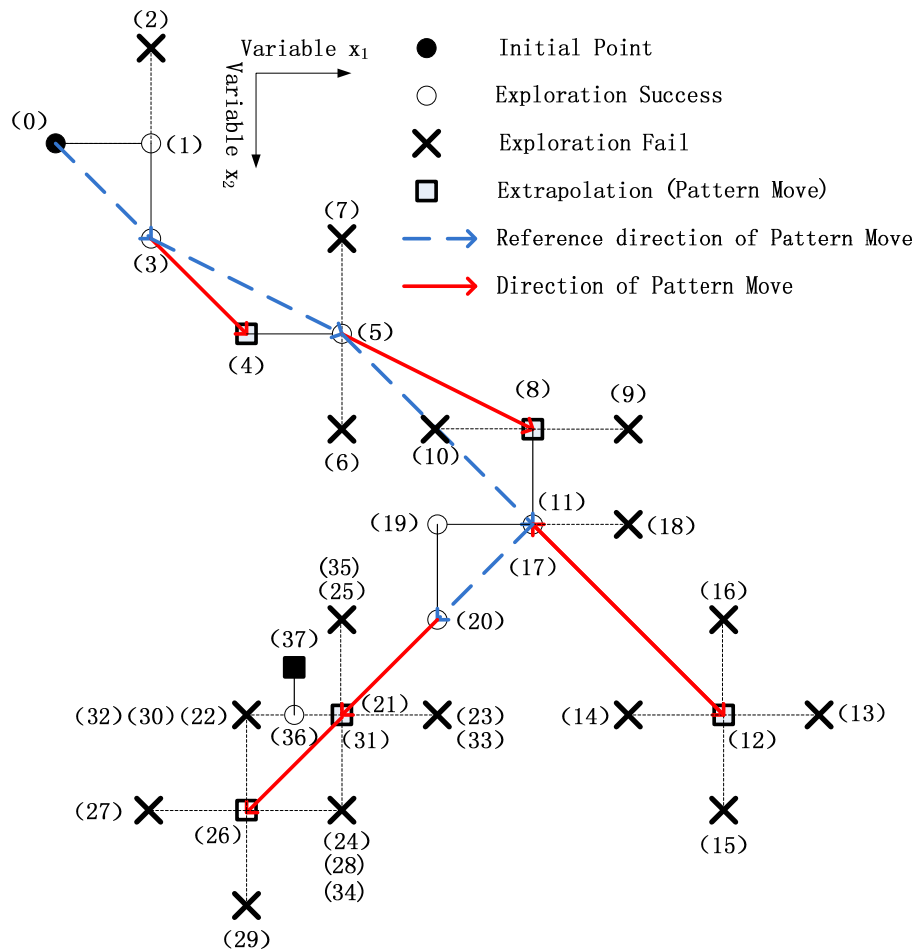


Fig. 3.16. Sketch of Hook-Jeeves algorithm (Pattern Search)

Table 3.1. Demonstration of Pattern Search method, corresponding to Fig. 3.16.

Iteration sequence	Numbering	Sequence of pattern move k	Sequence of Variable j	Comparison Point	Demonstration
1	(0)	0,1	-	-	Initialization
2	(1)	1	1	(0)	Success
3	(2)	1	2	(1)	Fail
4	(3)	1	2	(1)	Success
5	(3)	1	-	(0)	Compare with point k-1, Success
6	(4)	2	-	-	Pattern Move, But no comparison
7	(5)	2	1	(4)	Success

8	(6)	2	2	(5)	Fail
9	(7)	2	2	(5)	Fail
10	(5)	2	-	(3)	Compare with point k-1, Success
11	(8)	3	-	-	Pattern Move, But no comparison
12	(9)	3	1	(8)	Fail
13	(10)	3	1	(8)	Fail
14	(11)	3	2	(8)	Success
15	(11)	3	-	(5)	Compare with point k-1, Success
16	(12)	4	-	-	Pattern Move, But no comparison
16	(13)	4	1	(12)	Fail
17	(14)	4	1	(12)	Fail
18	(15)	4	2	(12)	Fail
19	(16)	4	2	(12)	Fail
20	(12)	4	-	(11)	Compare with point k-1, Fail
21	(17)	4	-	-	Previous pattern move Failed, Return to the point before pattern move
22	(18)	4	1	(17)	Fail
23	(19)	4	1	(17)	Success
24	(20)	4	2	(19)	Success
25	(20)	4	-	(11)	Compare with point k-1, Success
26	(21)	5	-	-	Pattern Move, But no comparison
27	(22)	5	1	(21)	Fail
28	(23)	5	1	(21)	Fail
29	(24)	5	2	(21)	Fail
30	(25)	5	2	(21)	Fail
31	(21)	5	-	(20)	Compare with point k-1, Success
32	(26)	6	-	-	Pattern Move, But no comparison
33	(27)	6	1	(26)	Fail
34	(28)	6	1	(26)	Fail
35	(29)	6	2	(26)	Fail
36	(30)	6	2	(26)	Fail
37	(26)	6		(21)	Compare with point k-1, Fail
38	(31)	6	-	-	Previous pattern move Failed, Return to the point before pattern move
39	(32)	6	1	(31)	Fail
40	(33)	6	1	(31)	Fail
41	(34)	6	2	(31)	Fail
42	(35)	6	2	(31)	Fail
43	(31)	6	-	(21)	(30) is equal to (20), execute step-reduction: $S_{k,j}=S_{k,j} * Ra$
44	(36)	6	1	(31)	Success
45	(37)	6	2	(31)	Success, step size $S < \epsilon$, execute terminal condition. Search accomplish.

3.3 Design examples

3.3.1 Broad angular bandwidth supermirror

A broad angular bandwidth supermirror has been designed as an example to demonstrate the optimization algorithm in last section. The designed structure and its corresponding reflectivity is shown as follows,

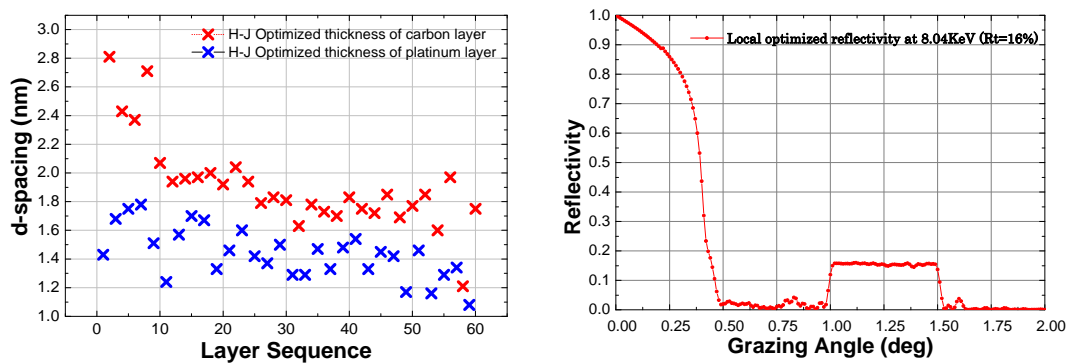


Fig. 3.17. Optimized thickness distribution of a broaden angular bandwidth supermirror and its corresponding reflectivity profile.

The angular response of optimized structure is very flat and smooth in target band (1.0-1.5deg) at 8.05keV, which demonstrates that the numerical approach is a success. However from a practical point of view, the supermirror is not always working under the designed energy point. If the oscillation of the profile is very sensitive for incident energies, then the numerical approach is meaningless.

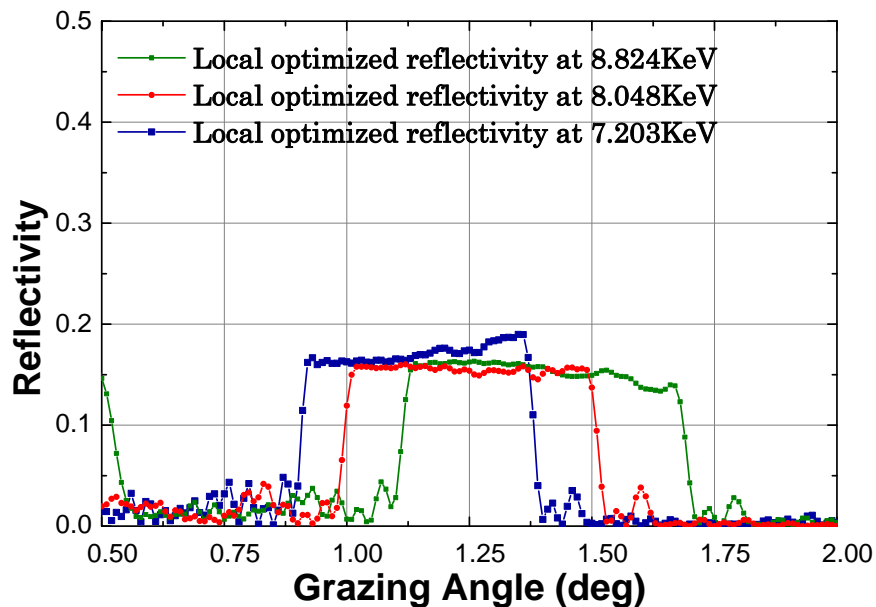


Fig. 3.18. Robustness check for incident energies of 7.203keV, 8.048keV and 8.824keV.

On the other hand, if the response is sensitive for the thickness errors, then the structure is very difficult to be fabricated which may prevent the numerical approach from applications. Many

previous works pointed out that the thickness of each layer cannot be deposited precisely in non-periodic structures. The thickness drifts randomly due to many experimental reasons such as the diffusion between the bi-layers, instability of the deposition rate and so on. This problem certainly oscillates the reflectivity profile, and thus leads to the failure of fabrication of designed structure without ripples of response. Therefore it is necessary to investigate the robustness of the reflectivity profile for incident energy of X-rays as well as the fabrication difficulty.

In order to check the robustness of the reflectivity profiles for incident energies, we shifted the incident energy $\pm 10\%$ and calculated the corresponding reflectivity profiles of the designed structure. The calculated results clearly demonstrated that although the top of the reflectivity profile slightly sloped, the ripples are not sensitive for incident energies.

Then we investigate the relation between the thickness error in production and the standard deviation of the reflectivity response. we assume that random thickness error happens in each layer, which follows the Gaussian distribution characterized by sigma. We calculated the standard deviation of the reflectivity response for different amplitude of thickness randomization, as is shown in following figure.

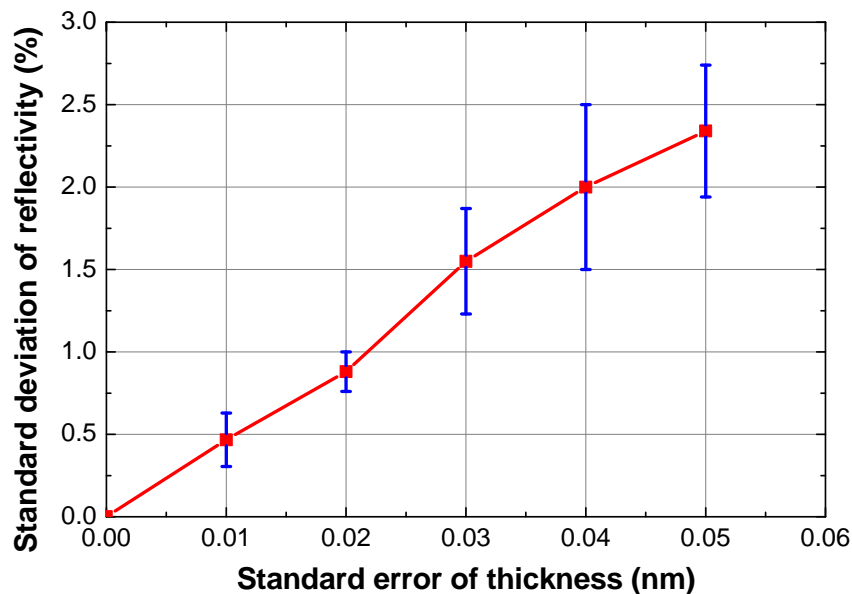


Fig. 3.19. Relationship between the standard deviation of reflectivity response and the randomization amplitude of individual layer thicknesses.

For each amplitude, we made 10 sets of layer thickness. The error bar shown in figure above is given by the scatter of standard deviation of reflectivity response of 10 sets. As is shown in this figure, if the standard deviation of the measured reflectivity response from design is supposed to be better than $\pm 1\%$, then the thickness controlling precision should be better than $\pm 0.02\text{nm}$. It is not a severe requirement which will be demonstrated in the section of fabrication.

3.3.2 Broad energy bandwidth supermirror

As an example of broad energy bandwidth supermirror, we planned to design an applicable one for real mission. In HXT of the ASTRO-H telescope, the boundary conditions were set as 45 cm diameter, 12-m focal length and 10-80keV range of interest. In general, the nominal incident angle $\theta(r)$ of a mirror located at the radius r is determined by the focal length of FL, as $\tan(4\theta) \sim r / FL$. Thus, 0.28deg of grazing angle and 10-55keV of target band are used as typical boundary conditions in broad energy bandwidth supermirror design.

As is demonstrated in section 2.1.3.2, the layer number of the power structure has been finally determined at 123. The thickness distribution shown in Fig. 2.12 satisfies our boundary conditions and is very suitable to be an initial structure for local optimization:

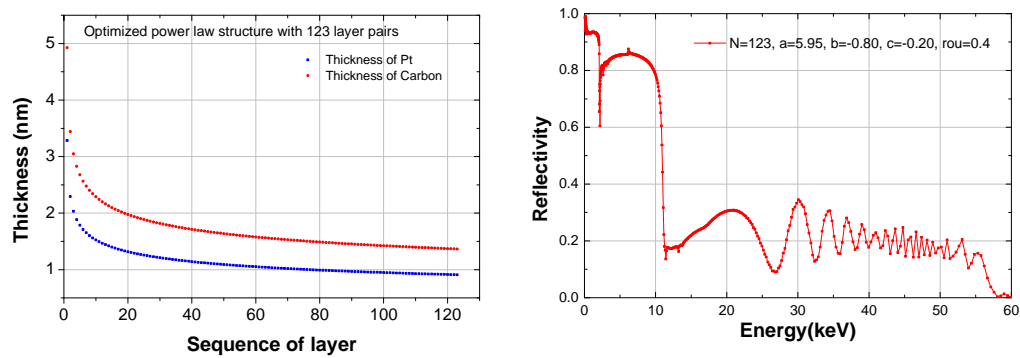


Fig. 3.20. An optimized power law structure for local optimization.

Our major goal is to achieve the highest level of reflectivity with a very flat profile. Before the start of the local optimization process, it is necessary to confirm that the target profile is achievable with boundary conditions. In Fig. 3.21, optimized reflectivity profiles are shown for the target flat profiles with different levels of reflectivity at 15, 18, 20, 22, 24 and 30%. The level of reflectivity can be higher than 20% by increasing the target reflectivity in some energy ranges, but the achieved flatness of the reflectivity profile becomes progressively worse. An attempt with 24% target reflectivity fails to keep 24% reflectivity after 35keV. Fig. 3.22 clearly demonstrates that the convergence of M.F. differs, depending on the target reflectivity.

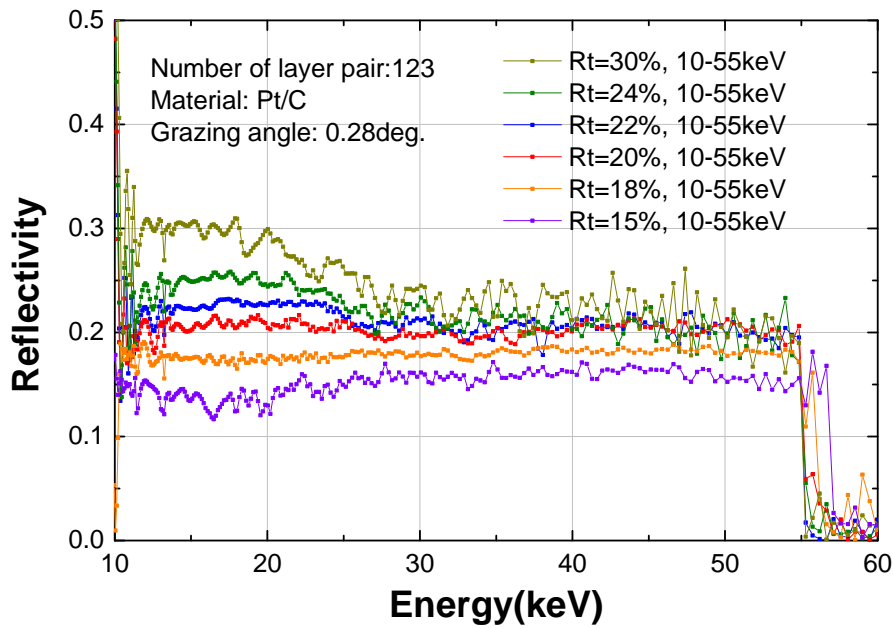


Fig. 3.21. Local optimized reflectivity profiles for different target reflectivities.

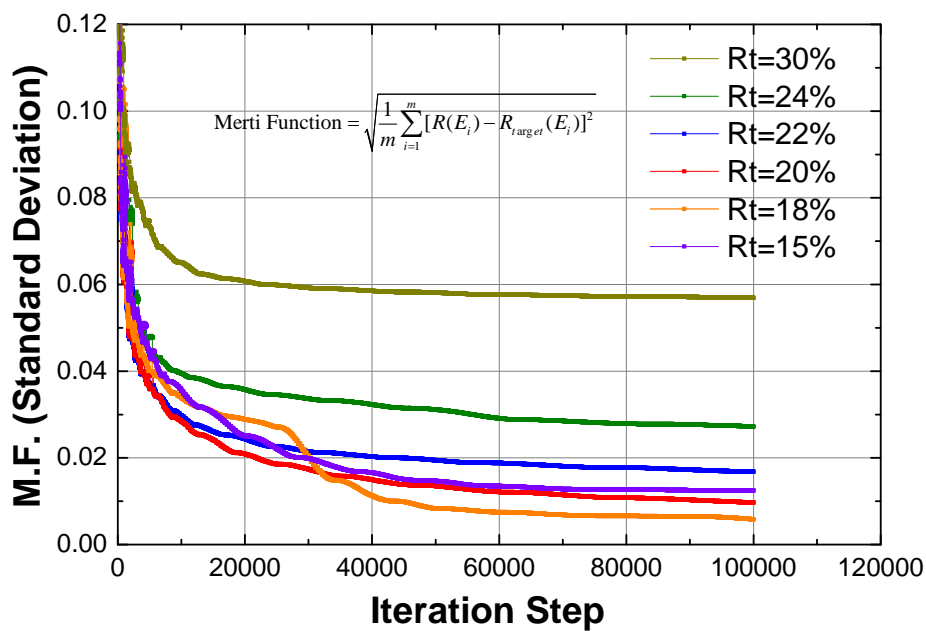


Fig. 3.22. Evolution of the corresponding merit function along with the number of iterations

If we raise the target reflectivity above 20%, for example, the M.F. cannot be improved to be smaller than 1.5%, and only the reflectivity in the low energy band (<30keV) can be enhanced significantly over 20%, which is not favorable for our purpose (flatness). Therefore, it is concluded that a target reflectivity of 20% is appropriate. Eventually, for 20% target reflectivity, the M.F. can be better than 0.7% within $2E^5$ iterations. The optimized structure and its profile are shown in following figure.

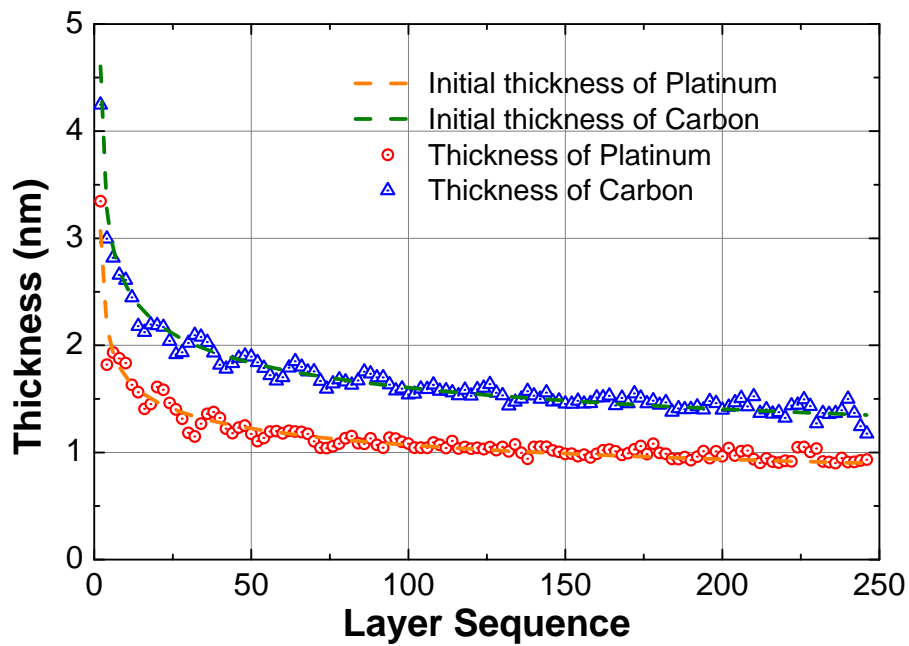


Fig. 3.23. Thickness distribution of supermirror structure. Dashed lines are the initial smooth thickness distribution following the power law. The blue triangles show the optimized thickness distribution of carbon. Red open circles show those of platinum.

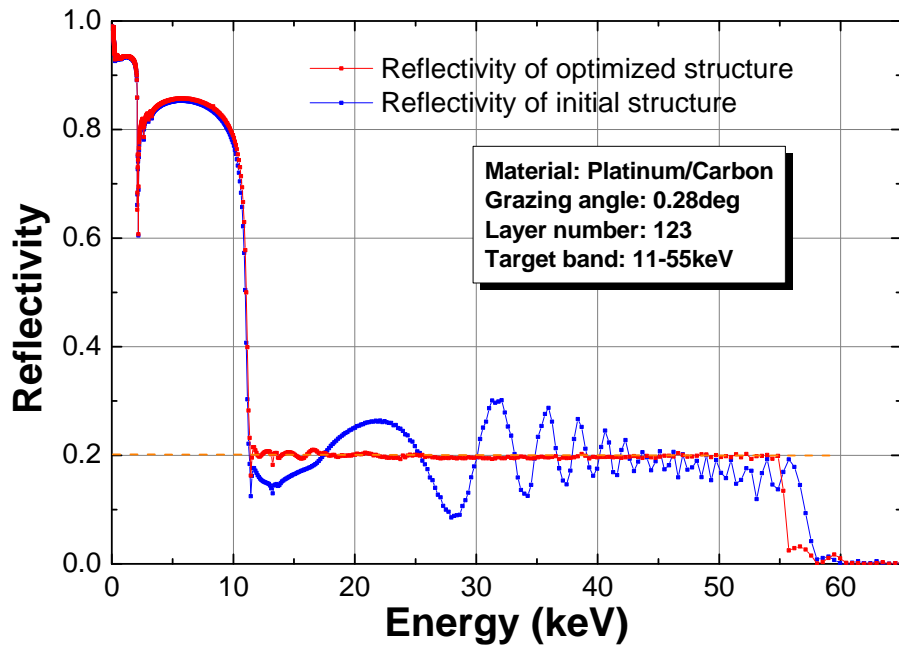


Fig. 3.24. Energy response profiles of the initial power law structure (blue) and optimized structure (red). The orange dotted line is the target reflectivity level at 20% between 12 and 55keV.

The design method introduced above can successfully achieve a flat top response. Then, we begin to apply it to an arbitrary sloped energy response as the target profile. As an example, a declining response, such as the supermirror design for ASTRO-H, is chosen as the target and the optimization result of the reflectivity profile is shown with a red line in Fig. 3.25.

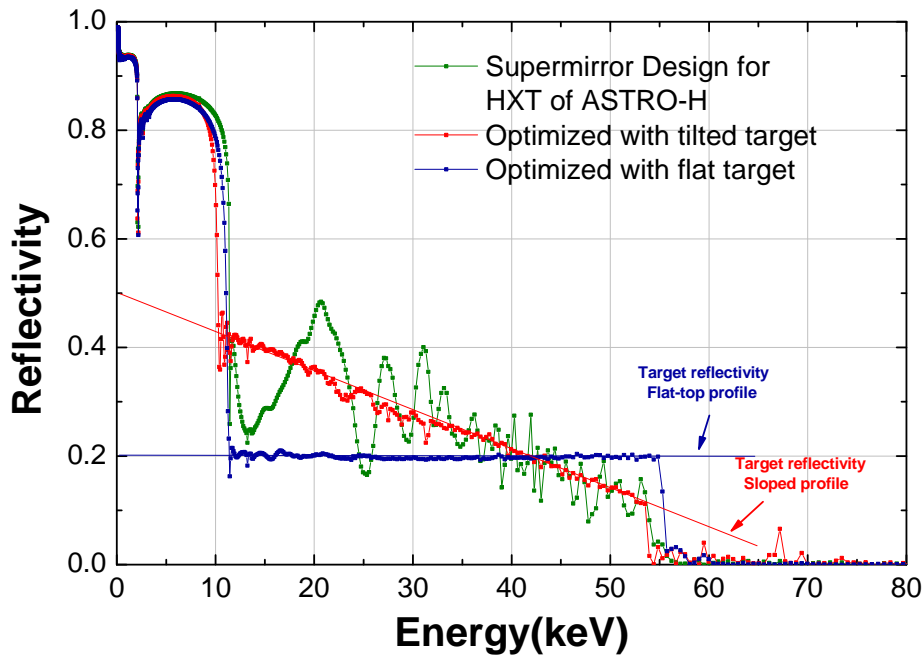


Fig. 3.25. Optimization result of a sloped response profile. The reflectivity profile of the red line is optimized from a supermirror design for HXT of ASTRO-H (green line) with the sloped target profile shown with the red dashed line. The blue data is the same profile of the red one in Fig. 3.24 with the flat target profile shown with the blue dashed line.

A supermirror structure with a sloped reflectivity profile can be obtained by our present design method with much smaller oscillation than the current ASTRO-H HXT structure (green line in Fig. 3.25) designed by the block method. In this case, the M.F. of the red line we can achieve is smaller than 1% within 2E5 iterations.

The integrated reflectivity of the red line is larger than the flat one shown with the blue line, because low energy X-rays are more easily reflected than high energy X-rays. Both of the profiles are optimized by our process with minimum oscillations.

In addition to nominal incident case, reflectivity at offset grazing angles is important for our application, because the field of view of telescopes is limited by the response at off-axis angles, where the incident angle differs from the nominal angle $\theta(r)$ according to the optical design of telescopes.

The response profiles designed so far are calculated for on-axis incident X-rays of the telescope. The response profile for off-axis X-rays has to be examined to know the field of view of telescopes. Since we did not optimize the energy responses for all grazing angles simultaneously, the possibility of serious oscillation for the response may become outstanding at large off-axis angles. In order to examine such a problem, the reflectivity profiles are calculated for various grazing angles, as shown in Fig.3.26.

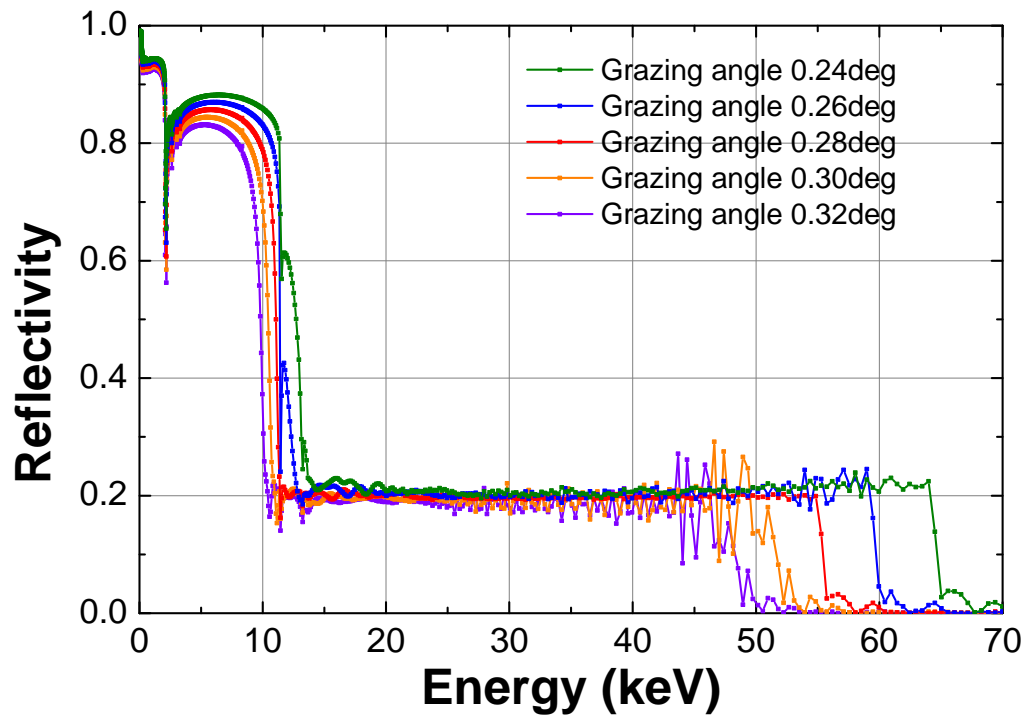


Fig. 3.26. Robustness check for the grazing angles. Reflectivity profiles of the supermirror structure optimized at 0.28deg are calculated with 5 different grazing angles ranging from 0.24 to 0.32deg.

The designed supermirror structure mostly keeps consistent energy response with different grazing angles, though the high energy end of the response slides toward low energies for large incident angles of 0.30 degrees or larger. At the same time, some oscillations seem to evolve in the high energy side at large grazing angles. It could be due to the mis-matching of secondary peaks, because they were carefully suppressed by the tuning of the structure at 0.28 degrees but may start to misfit each other. We are able to conclude that the supermirror structure designed for 0.28 degrees provides a similar flat response in most of the energy range, except at high energy ends.

Fidelity of the fabricated thickness distribution to the optimized design structure should also be examined carefully. The standard deviation of the reflectivity profile from the target profile has been calculated for different amplitudes of thickness randomization (Fig. 3.27). For each amplitude, we made 100 sets of layered structures. The error bars are given by the scatter of σ of 100 sets.

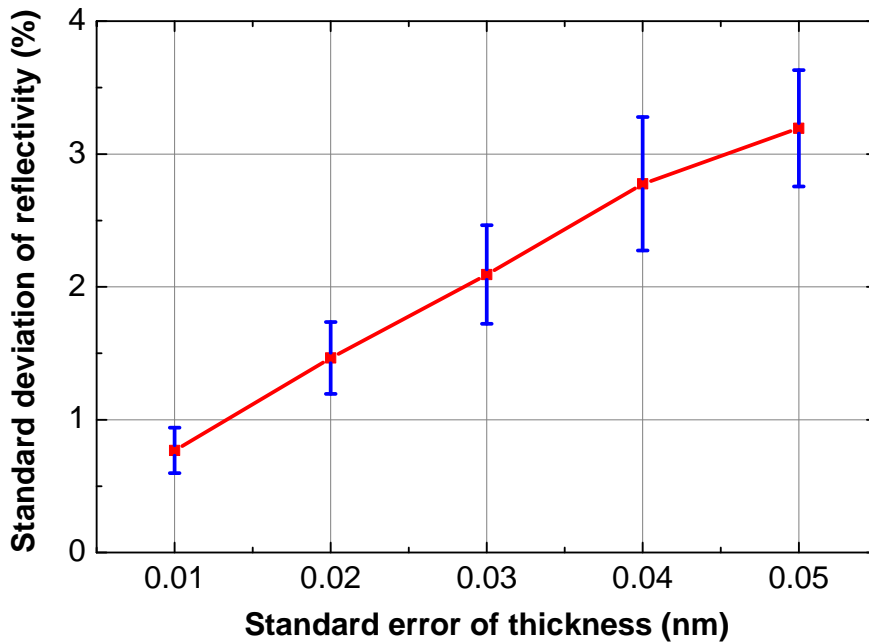


Fig. 3.27. Standard deviation of reflectivity response versus the randomization amplitude of individual layer thicknesses. Error bars are given by the scatter of standard deviation of reflectivity response of 100 sets.

Fig. 3.27 illustrates that the fluctuation of the reflectivity profile directly correlates with the thickness controlling precision, i.e., sigma of Gaussian distribution. For example, if we want to get a lower reflectivity oscillation of 1.5%, then the thickness controlling precision of $\sim 0.02 \pm 0.005 \text{ nm}$ is needed to fabricate corresponding structures. The thickness controlling precision can be obtained by our fabrication process, which will be introduced in following chapters.

3.4 Comparison between presented design and previous design

In order to demonstrate the great advantage of the supermirror structure introduced in this chapter for hard X-ray telescope applications, here I calculated two response profiles (effective area) of hard X-ray telescopes with different supermirror coating for comparison. Since my design target is a flat response, block structure supermirror designed for ASTRO-H is no longer suitable in this case. Therefore, I assume two telescopes of which the structures (grazing angles of each mirror shell) are the same as HXT of ASTRO-H, but for each telescope, the coating on the surface of all the mirror shells are power law structure (Fig. 3.20) and local optimized structure (Fig. 3.23). The calculation results are shown as follows.

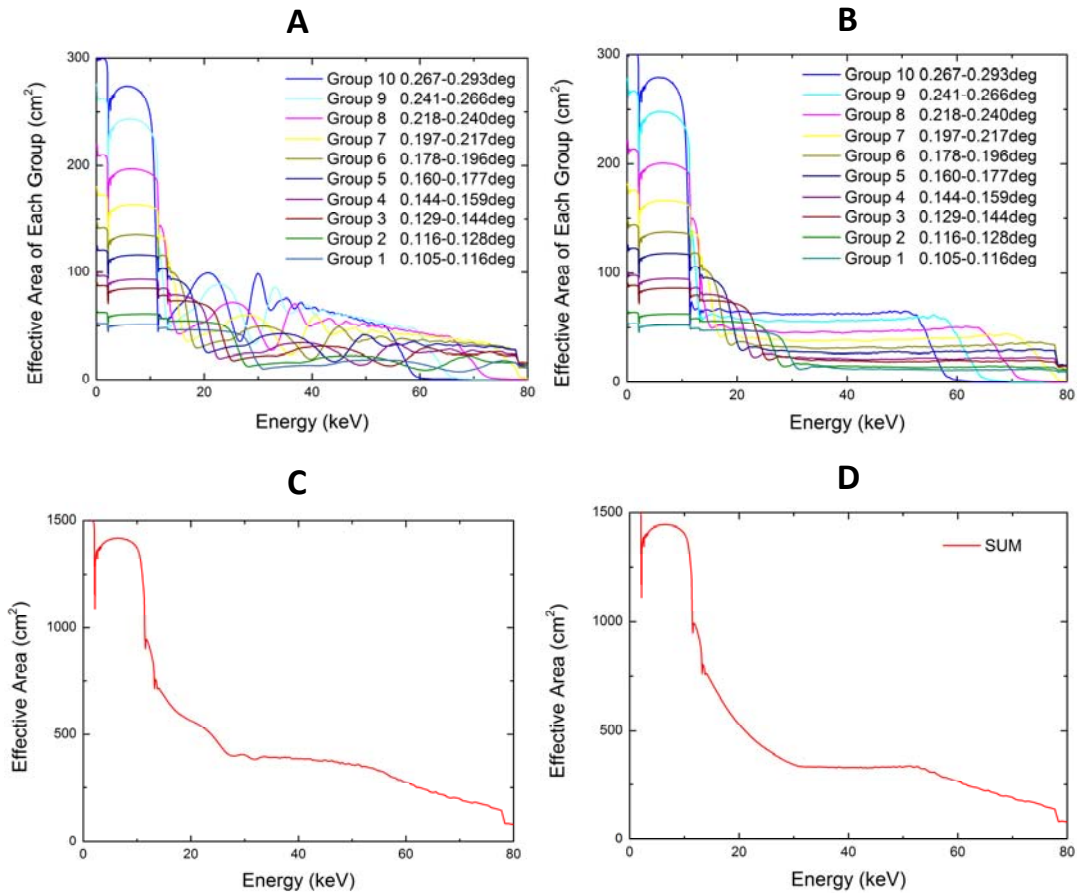


Fig. 3.28. Calculated effective areas (one reflection) of telescopes with different coating.

Panel A and B demonstrate the calculated effective area profiles for each mirror group. Panel A corresponds to power law coating and panel B corresponds to local optimized supermirror coating. As are shown in those panels, lines in B are orderly distributed while these in panel A are disorderly distributed. Subsequently the power law coating is difficult to provide smooth total effective area, as is shown in panel C. And panel D, corresponding to local optimized supermirror, is ideal to prohibit ripples which is a great convenience for calibration process of telescopes. In order to demonstrate how much ripples I can avoid from my design, profile shown in panel D is divided by that shown in panel C. Following figure clearly demonstrates that about 10% ripples can be smeared out once the telescope selects my design.

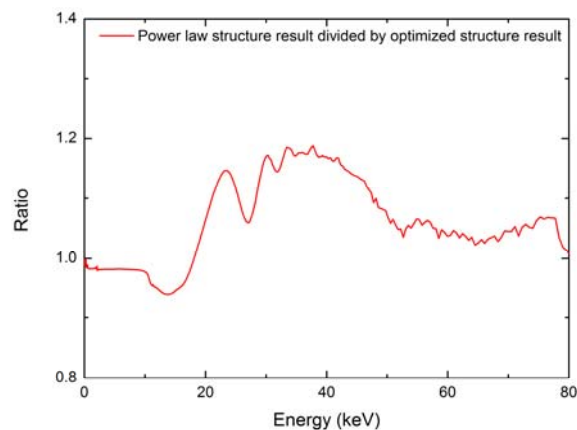


Fig. 3.29. Ratio between the effective area of my design and power law design.

Chapter 4.

Fabrication of the supermirror structures

4.1 Fabrication processe

4.1.1 Deposition system

We use a DC-magnetron sputtering system to deposit supermirrors on a substrate such as a float glass for example. Sputtering is a process that a solid material (target) ejects atoms toward a substrate, due to the bombardment of energetic particles. In case of DC-magnetron sputtering process, the orthogonal electric and magnetism fields continuously ionize an Argon gas at low pressures, drive the Ar^+ strike the target surface, knock out the atom of the target and let it fly toward the substrate, as is shown in following figure.

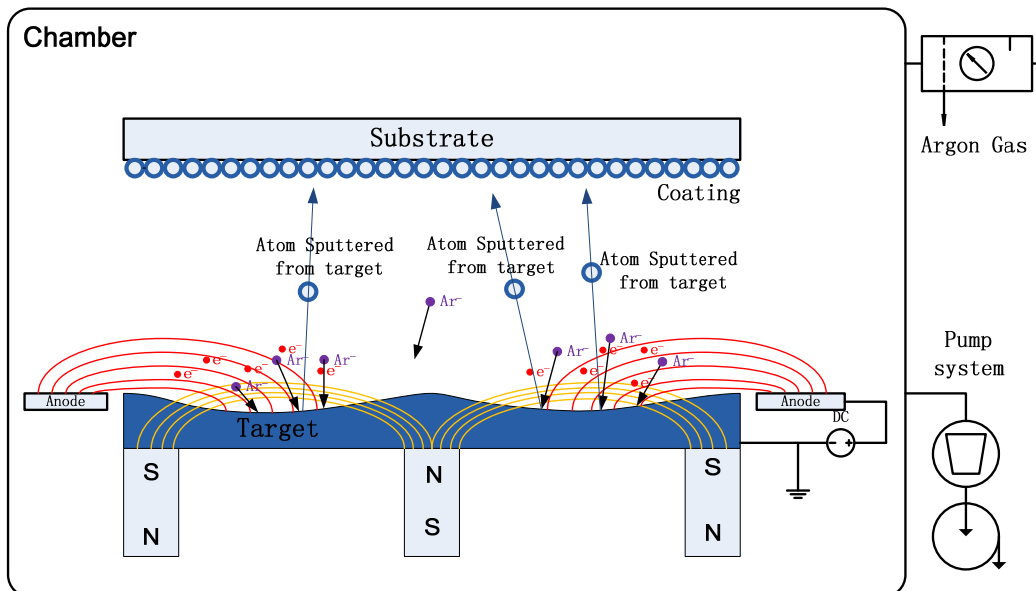


Fig. 4.1. Sketch of a DC-Magnetism sputtering system

The sputtering process only can be realized in a very low pressure condition ($\sim 1 \times 10^{-4}$ Pa) due to the fact that the Argon gas turns out to conduct electricity in this pressure. When the argon gas is ionized by the electric fields, ionized electrons are firstly driven toward the target. Then, since the magnetism fields are orthogonal with electric field, Lorentz force begins to affect the path of electrons when they accumulate speed. Eventually, the electrons are trapped by the fields and move helically near the surface of the target, continuously ionize the argon gas, produce a large number of nucleus of Ar. The nucleus are also driven by the electric and magnetism field, but the Lorentz force is negligible due to the fact that the nucleus are much heavier than electrons. Eventually the nucleus of Argon gas strike the surface and produce flow of materials.

The number of ionized nucleus is strongly correlated with the pressure of Argon gas. The lower the pressure is, the lower the sputtering rate. However, lower pressure lead to several desirable features. For example, lower pressure may reduce the possibility of collision between the atom of Argon gas and that of sputtered materials. That means the direction and incident energy of sputtered atom can be improved and subsequently raise the quality of coating layer. Practically,

the best pressure is determined at the lowest level that the plasma can be produced stably in front of the target (4×10^{-4} Pa). The corresponding parameters such as the distance between the target and the substrate, the voltage of electricity potential and the current should also be optimized to promise the best coating quality.

In order to fabricate supermirror structures for telescope application, DC-Magnetron sputtering system at Nagoya University is designed to deposit the multilayer on the outer surface of a cylindrical glass mandrel for replica mirrors of X-ray telescopes. It can also be used for small flat glass substrates as test samples. Two sputtering sources of Platinum and Carbon are located on the left and right sides of the vacuum chamber.



Fig. 4.2. DC-Magnetron sputtering system at Nagoya University. Left panel shows the Pt target.

As is shown in the figure, a big rotary stage is located inside the chamber. On the stage there are four sample holders which can spin in designated rate. When sputtering, samples are stick on the surface of a sample holder. The rotary stage rotates and moves the sample at the position that in front of a sputtering source. Then, the sample is exposed to the flow of sputtering material. By adjusting the spin speed of the holder, the thickness of individual layers is controlled. Therefore, a layered structure of a supermirror can be finally fabricated.

The biggest advantage of this DC-Magnetron sputtering system is its stability and high deposition rate (~ 0.1 nm/s for Platinum). The thickness error will be better than 0.02 nm for each layer. It will be demonstrated in following sections.

4.1.2 X-ray measurement system

The angular/energy response of a fabricated sample can be measured by X-ray reflectometers located in laboratories at Nagoya University and the Institute of Space and Astronautical Science. A reflectometer consists of an X-ray generator, a double crystal monochromator, several slits, a sample stage which is movable in X-Y dimension and rotatable in θ dimension. The sketch of a reflectometer and its components are plotted in following figure.

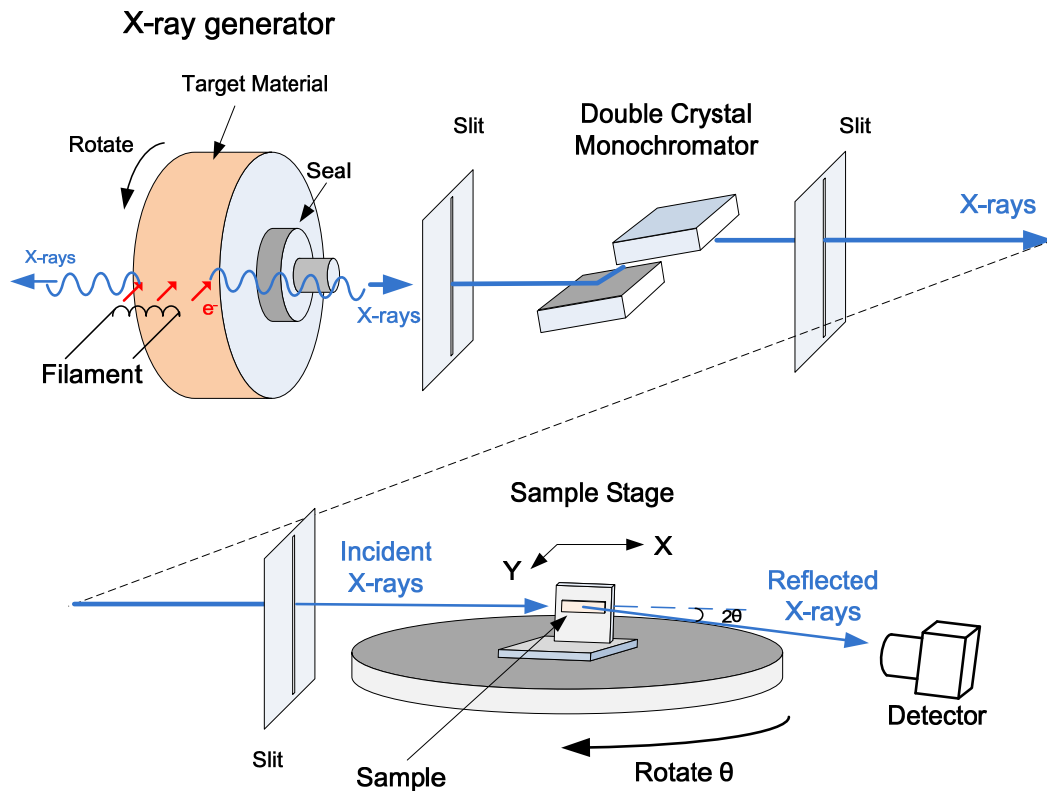


Fig. 4.3 Sketch of an X-ray reflectometer and its components

As is shown in figure above, thermal electrons (5-60kV) are produced by a filament and hit the surface (1mmX10mm) of a selected metal target (Copper, typically) which spins fast ($\sim 6000\text{rpm}$) to avoid high temperature in small area. At this time the characteristic and Bremsstrahlung X-rays are produced and emit perpendicularly to the direction of the electrons' velocity. Due to the fact that the grazing angle of the emission X-rays is small, the X-ray generator can finally provide a 1mmX1mm X-ray source.

When measuring the angular response of a sample, X-ray energy should be fixed. Therefore the double crystal monochromator (DCM, typically made by Germanium) is necessary to purify the spectrum by means of Bragg reflection. By adjusting the grazing angle of X-rays, characteristic line is selected to pass the DCM, and others are filtered.

In case of measuring the energy response of a sample, DCM is no longer necessary and removed from the beam line. The energy response can be measured by a CdZnTe detector due to its energy resolution ($\sim 10\%$ at 8keV).

Fabricated sample is mounted on the sample stage which provide 3 dimensions (X,Y and θ) to align the sample with the incident X-rays. When measuring, the stage can rotate to adjust the

grazing angles (θ) while the detector may rotate (2θ) as well to receive the reflected X-rays. The Cadmium Zinc Telluride detector is a semiconductor one which absorbs the X-rays by means of electron/hole pair.

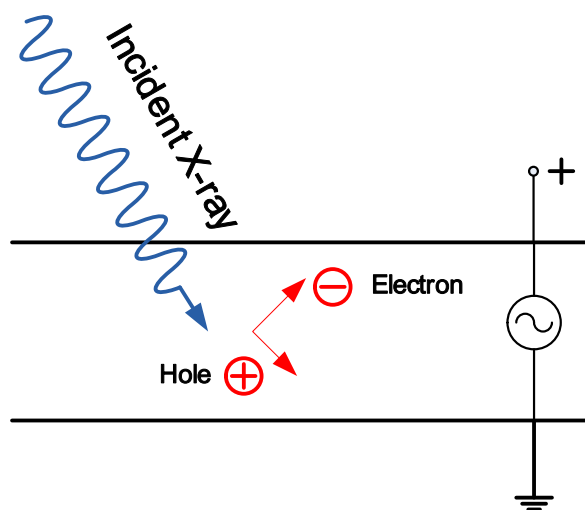


Fig. 4.4 Sketch of a CdZnTe detector.

When high energy X-ray photon comes in, the electrons are knocked out from its original position, subsequently creates Electron-hole pairs. With the bias voltage, the electron/hole pairs move to the anode at the surface and bottom of the crystal. The current pulse is magnified by an amplifier and detected by an oscillator. As we know that the energy of X-ray photon is proportional to the number of pairs, and the number of pairs is in proportion with the height of pulse. Therefore the incident energy of X-rays can be identified by measuring the pulse height. Since the number of the pairs N follows poisson distribution. And the standard deviation of poisson distribution follows the root square of N . Therefore the width of the response ΔE is proportional to the root square of E . Typically energy resolution is $\sim 10\%$ of incident energy at 8keV.

Following figure shows the reflectometer in ISAS lab.

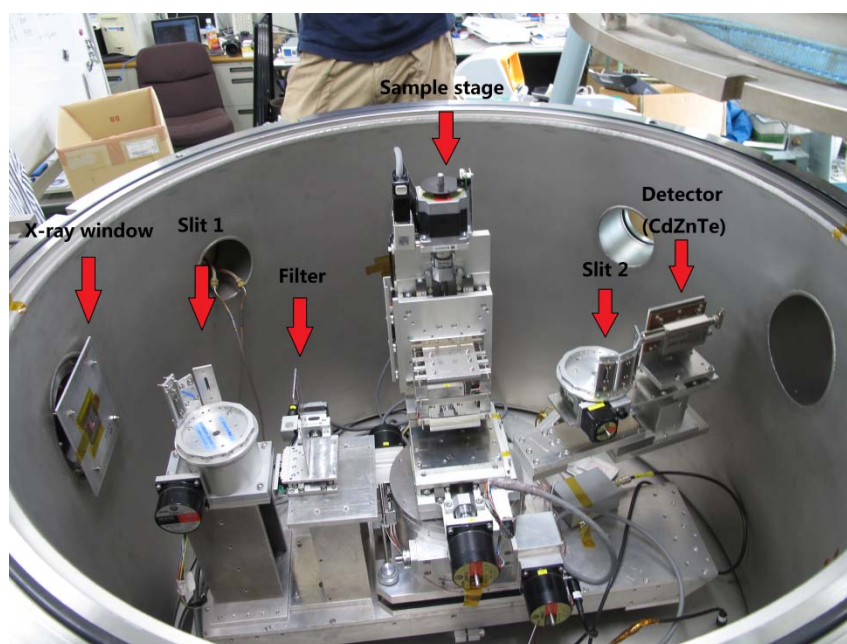


Fig. 4.5 X-ray reflectometer in ISAS Lab.

4.1.3 Calibration and thickness controlling

Thickness controlling is essential for supermirror fabrication process. As is mentioned in section 4.1.1, it is realized by controlling the exposure time by means of adjusting the spin rate of the sample holder. However in order to learn the relations between the spin rate and the thickness of deposited layer, a calibration process is necessary.

In this process we firstly fabricate a periodical multilayer with constant d-spacing. Then we measure the angular response of this fabricated sample by using the reflectometer. The measured reflectivity profile is fitted by a calculated model. From the model, the d-spacing, Gamma and interfacial roughness of the fabricated sample can be estimated, and thus the relation between the spin rate and the thickness can be determined.

The model is a reflectivity profile calculated by Parrat's algorithm and D-W factor. Four parameters (d-spacing, Gamma, roughness of the interface from Pt to C and that from C to Pt) are necessary to calculate the model.

The relation between those parameters and the reflectivity profile are demonstrated in following figures.

1. Reflectivity profiles for different d-spacings.

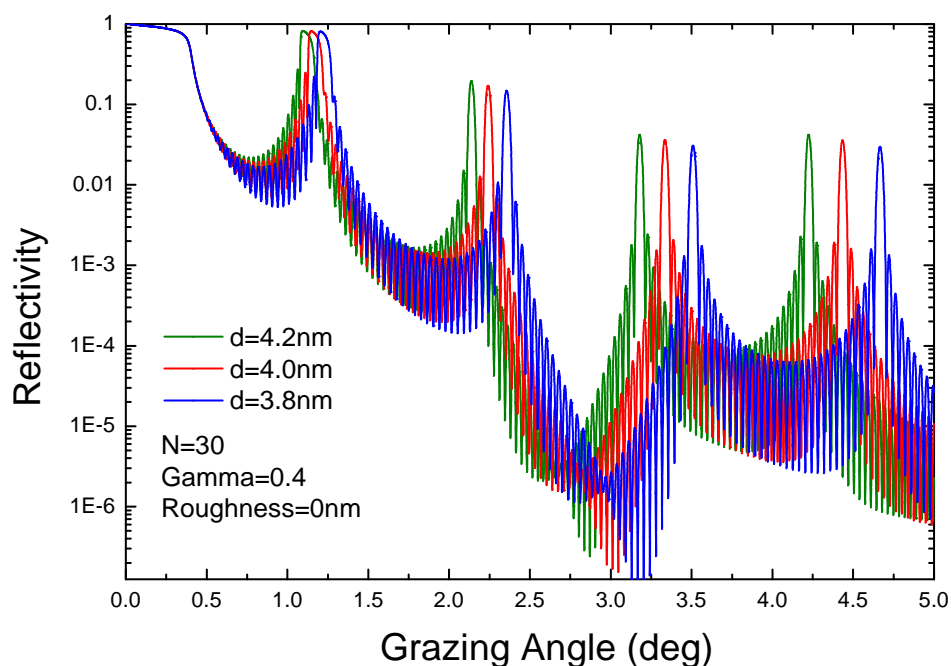


Fig. 4.6 Reflectivity profiles calculated by Parratt's algorithm for different d-spacing

The position of Bragg peaks are determined by the d-spacing which can be calculated from the Bragg's equation. Especially for high order Bragg peaks, the drifts of the position become significant for a constant difference of d-spacing. By comparing the position of calculated reflectivity with that of measured reflectivity, the d-spacing of fabricated structure can be determined.

2. Reflectivity profiles for different Gamma.

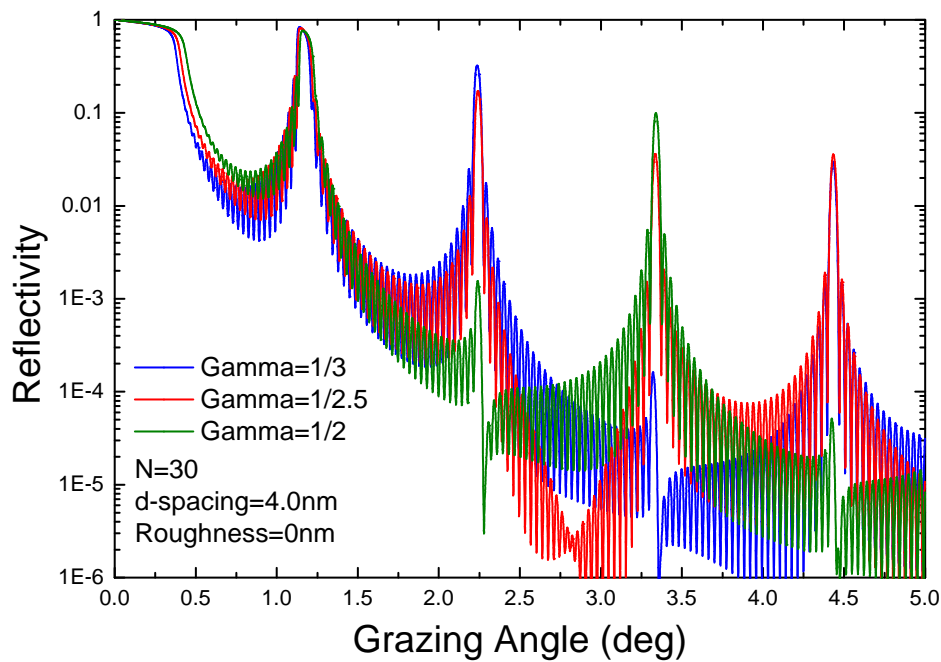


Fig. 4.7 Reflectivity profiles calculated by Parratt's algorithm for different Gamma.

An independent value of Gamma may suppress the intensity of a specific area of reflectivity profile, and thus significantly affect the intensity ratios between Bragg peaks. As is shown in figure above, when the Gamma is equal to 1/3, the third order Bragg peak is vanished. Similar phenomenon happens between second and third order peak when Gamma is equal to 1/2.5, as well as that of the second order Bragg peak when Gamma is equal to 1/2.

This phenomenon is called "the extinction of Bragg peaks" and can be explained in following figure.

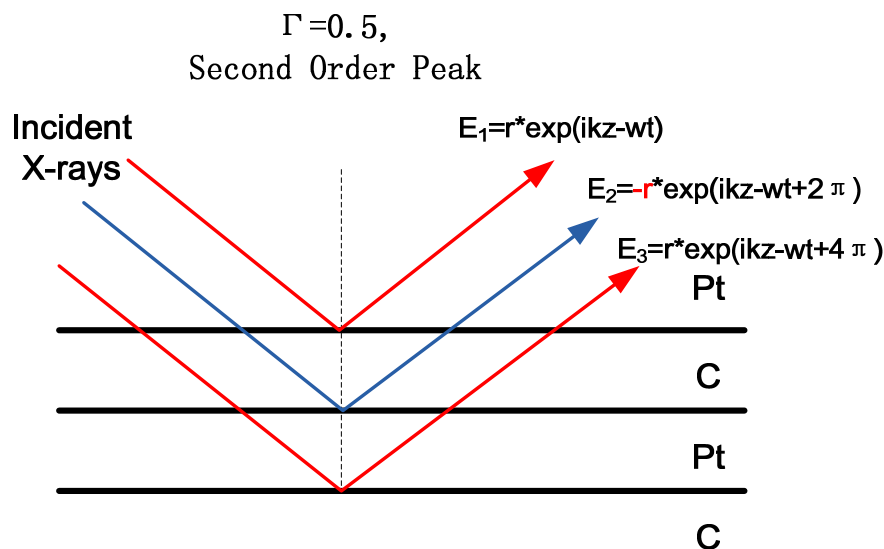


Fig. 4.8 Extinction of second order Bragg peak when Gamma=1/2.

Figure above shows one period of multilayer when Gamma is equal to 0.5. We assume that the

grazing angle of incident X-rays is at the angle of second peak. Due to the second order reflection, the X-rays reflected by all the boundaries may have the same phase at the first boundary (i.e., surface of the multilayer). However when the X-ray hit the first and third boundaries, it transmit from high-z material to low-z material which lead to a positive Fresnel reflectivity, while what happens at the second boundary is opposite. Therefore the final reflectivity (sum of three) is minimized. When Gamma is equal to 0.5, the extinction phenomenon happens at second, fourth and subsequent Bragg peaks.

Similar phenomenon can be understood in the same way when gamma is equal to 1/3, 1/4 and so on. It provides an opportunity to determine the Gamma value by examining the intensity ratio between Bragg peaks and fitting process. In real case, the ratio and absolute value of Bragg peak may also be affected by the interfacial roughness.

3. Reflectivity profiles for different interfacial roughness.

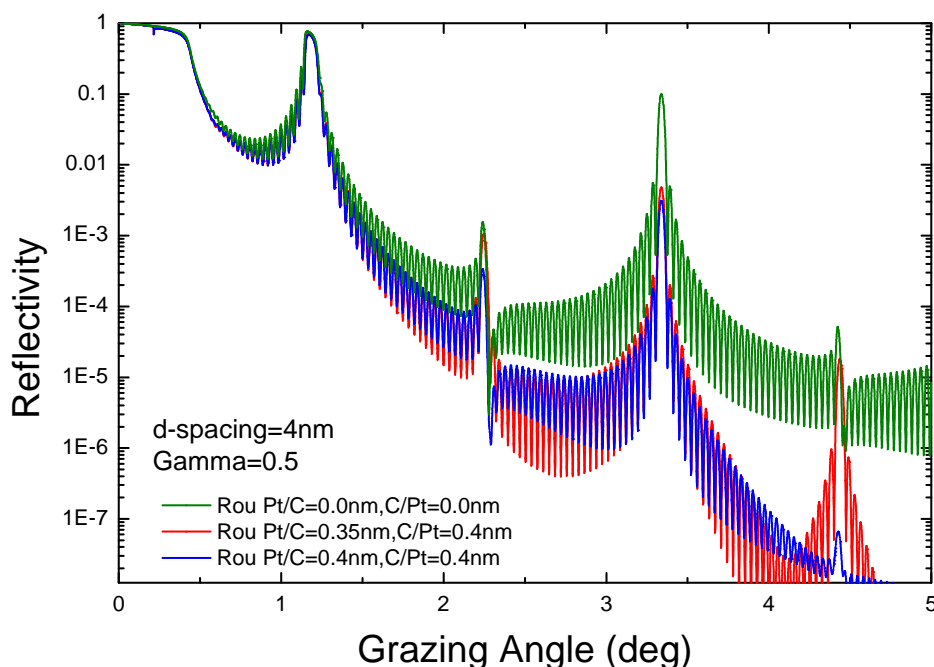


Fig. 4.9 Reflectivity profiles for different interfacial roughness.

As is shown in figure above, we assume X-rays reflected by a supermirror structure of which the d-spacing is 4nm and Gamma is 0.5. The interfacial roughness may significantly reduce the reflectivity at large grazing angle due to the essence of D-W factor (see Chapter 2.1.2.). Moreover, when the roughness of the Pt/C boundary is different from that of C/Pt boundary, the extinction phenomenon is destroyed. The second and fourth order Bragg peaks are recovered which can be explained by Fig. 4.8: Reflected of the first and second boundary is no longer equal due to the difference of reflectivity, which may lead to increasing of the final reflectivity at the surface.

Overall, there are four parameters which need to be determined in fitting process. When adjusting the parameters, the Gamma and roughness should be carefully balanced to obtain a convincing fitting result. A fitting example is shown in following figure.

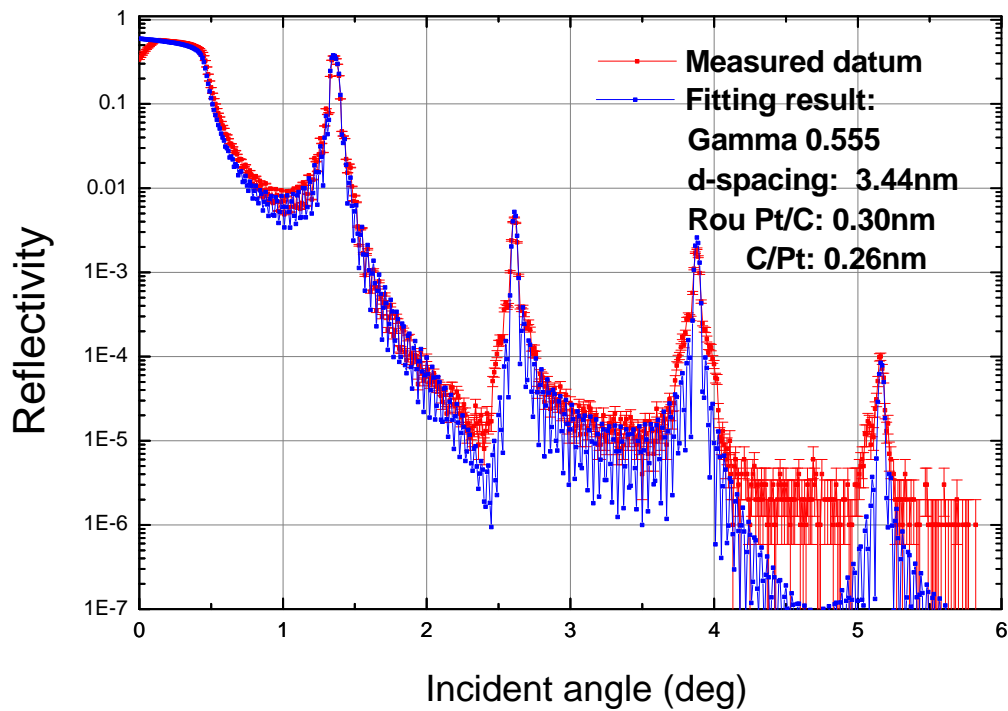


Fig. 4.10 An example of fitting result. Red line means the measured data and blue line demonstrates the fitting model.

Considering the fitting process is operated manually, and it's important for fabrication process, we usually fabricate 6 samples with different d-spacing. The fitted thicknesses of those samples for the corresponding spin rate of sample holder are plotted and considered together to estimate the sputtering rate. The detail of this process will be demonstrated in following section.

4.2 Fabrication and testing results

4.2.1 Broad angular bandwidth supermirror

The design process of the broad angular bandwidth supermirror has been demonstrated in Chapter 3.3.1. An example of designed structure and its corresponding reflectivity are shown in following figures, the same as Fig. 3.17.

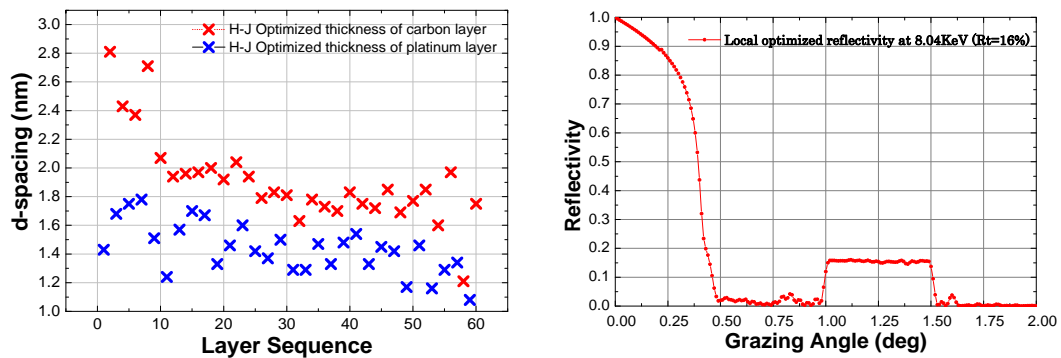
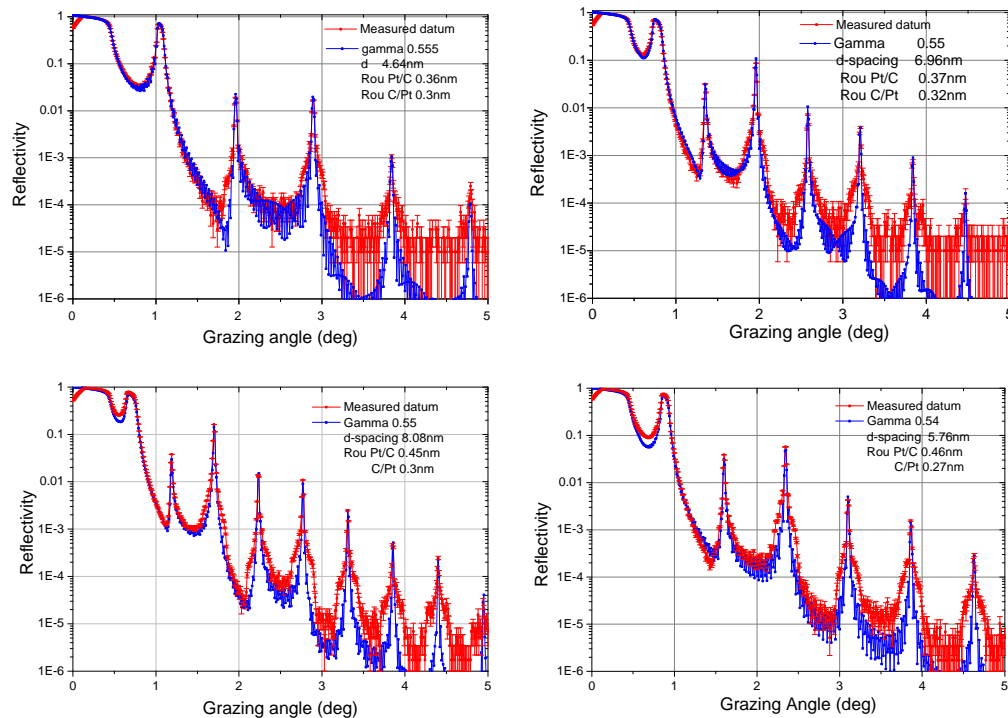


Fig. 4.11 A designed structure of broad angular bandwidth supermirror and its corresponding reflectivity.

In order to fabricate this structure, I fabricated 6 calibration samples and measured the angular response at 8.05keV. The testing datum and the fitting results are shown in following figures.



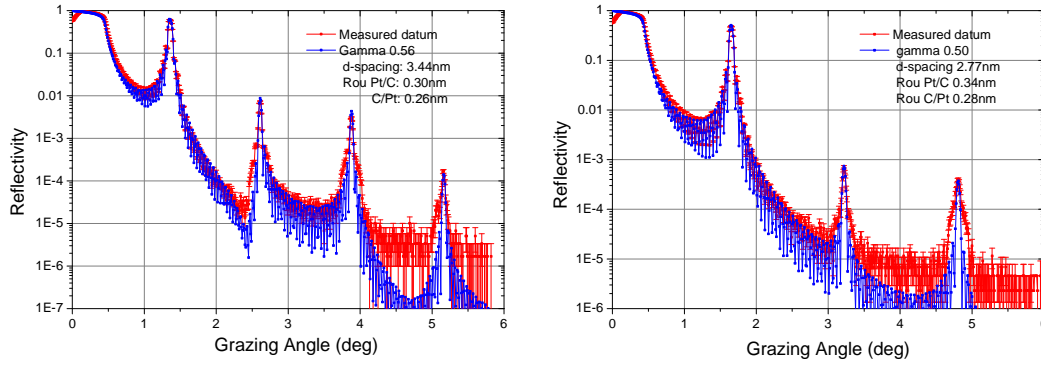


Fig. 4.12 Testing and fitting results of calibration samples.

From those fitting results, we can determine the individual thickness of Pt layer and C layer of each calibration sample. They are plotted against the corresponding spin rate.

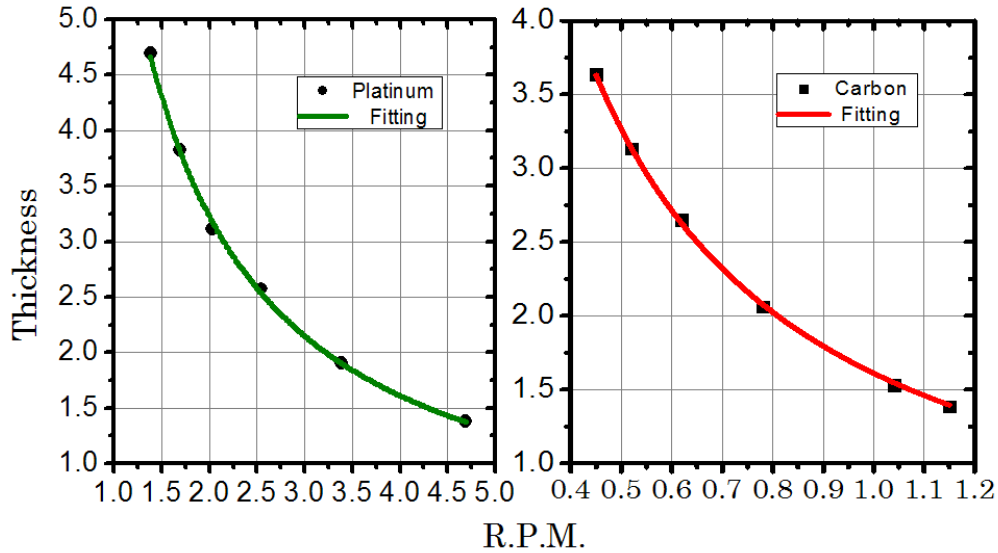


Fig. 4.13 Thickness of multilayer against rotation speed (R.P.M.). Curves are the best fit curve of reverse proportion. Standard deviation from the model is $\sim 2.5\%$

R.P.M. is the rotation speed of the sample holder in our DC magnetron sputtering system. The green line and red line represent the models of the reverse-proportional function of R.P.M.. Scatter around these lines corresponds to the standard deviation of 2.5%. This suggests the thickness accuracy of 0.02nm for a layer thickness of 1nm, for example. The random error between the data point and fitting curve may due to the controlling precision of the sample holder or error of fitting process, which is very small (2% for 1nm) and can be neglected for supermirror fabrication process.

After the calibration process, the relation between the deposition rate and rotation speed has been understood accurately. Then, the designed structure shown in Fig.4.11 has been converted into the spin rate and input our sputter system. The reflectivity curve of the designed structure has been finally measured.

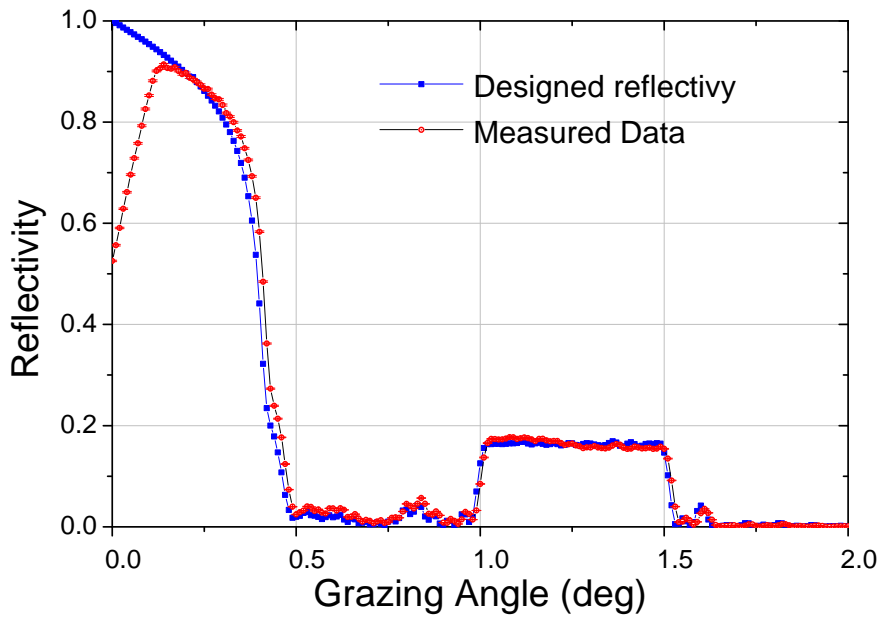


Fig. 4.14 Measured reflectivity (red line) and design result (blue line). Reflectivity vs. grazing angle. In target band (1.0deg-1.5deg), the standard deviation of measured data from design result is 0.76%

In figure above, the red curve is the measured data, and the blue line is the designed response. In target band from 1.0deg to 1.5deg, the deviation of the measured reflectivity from the design value is 0.76%. In order to learn the relation between the thickness error in production and the standard deviation of the reflectivity response, we assume that random thickness error happens in each layer, which follows the Gaussian distribution characterized by sigma. We calculated the standard deviation of the reflectivity response for different amplitude of thickness randomization

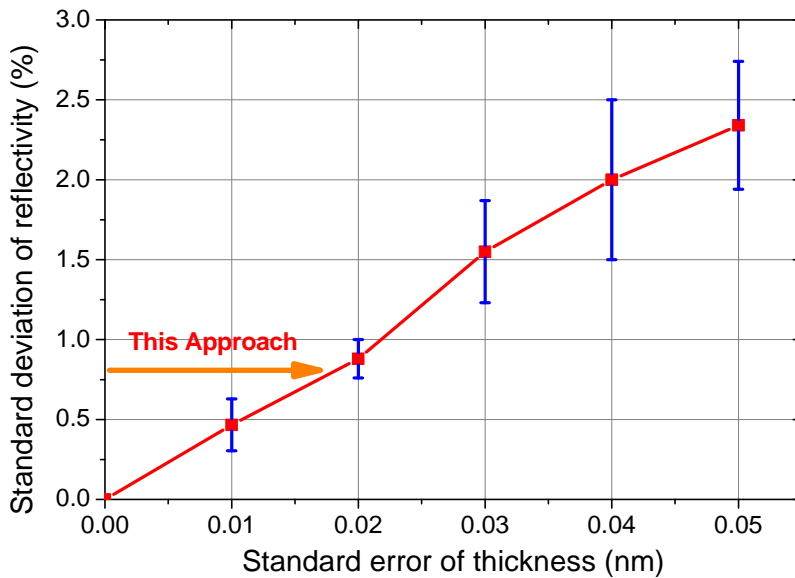


Fig. 4.15 Relationship between the standard deviation of reflectivity response and the randomization amplitude of individual layer thicknesses. Standard deviation of reflectivity response of the measured sample is 0.76%, which suggests our deposition system can be as accurate as 0.02nm in layer thickness.

For each amplitude, we made 10 sets of layer thickness. The error bar shown in Fig. above are

given by the scatter of standard deviation of reflectivity response of 10 sets. As shown in Fig. 4.15 the thickness control of our fabrication process should be as good as 0.02nm, since the standard deviation of the reflectivity response with our supermirror is 0.76%. From Fig.4.13, we confirmed the accuracy of thickness control is 2.5%, which corresponds to 0.02nm or so. It is consistent with the results in Fig.4.15.

From figures above, conclusion has been made that the fabrication of a broad angular bandwidth supermirror is successful. The design and fabrication process are correct and promise for other applications. In following sections I'll introduce other examples to support this conclusion.

4.2.2 Broad energy bandwidth supermirror

In Chapter 3.3.2, we introduced a design structure of broad energy bandwidth supermirror which is very suitable for telescope application. In this section I would like to introduce the calibration and fabrication result of this sample. The designed structure and its corresponding response is shown in following figure.

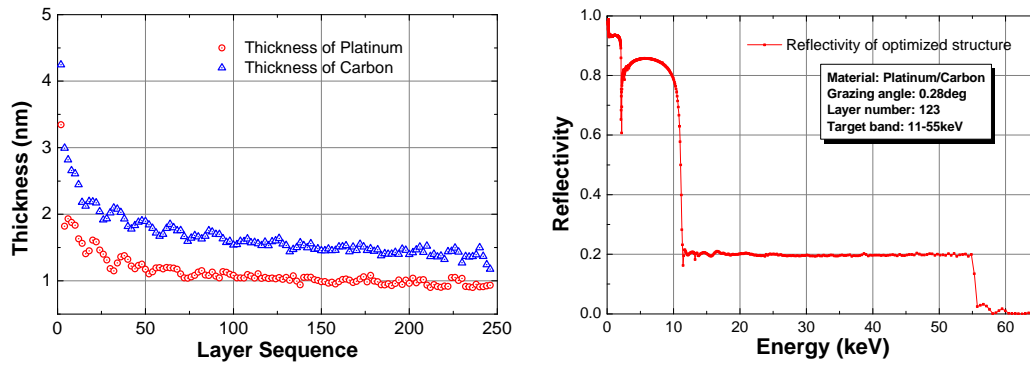
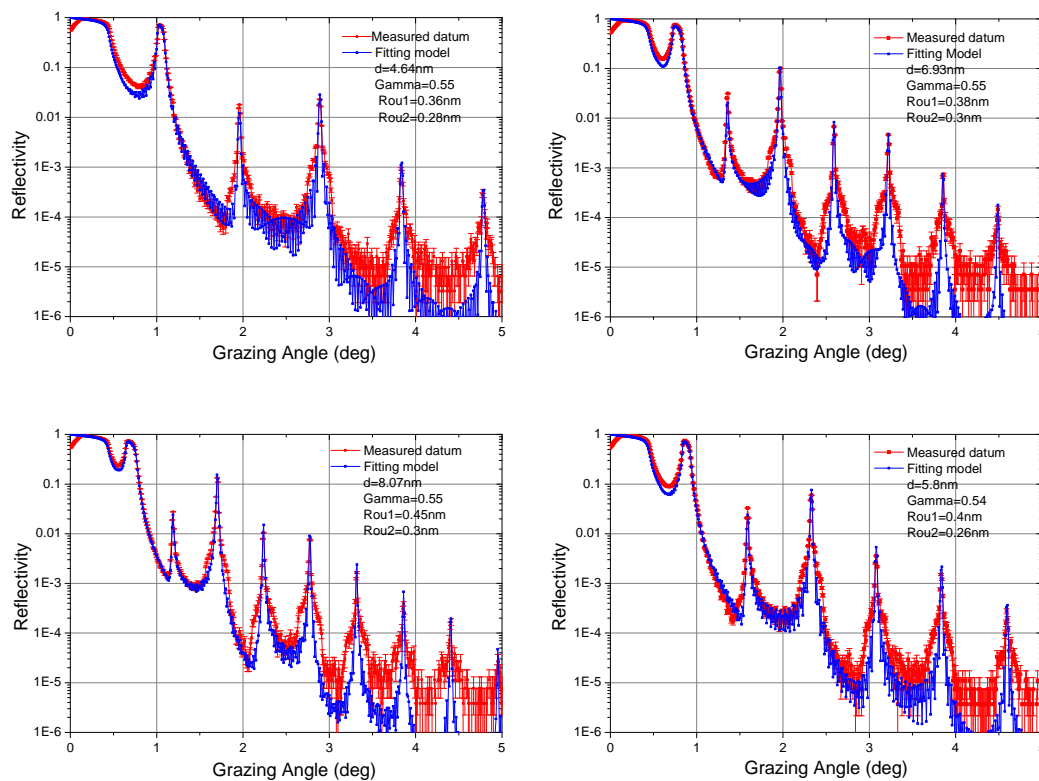


Fig. 4.16 Designed thickness distribution and its corresponding energy response.

Still, the first step is to fabricate calibration samples and measure the reflectivity. The testing and fitting results are shown in following figures.



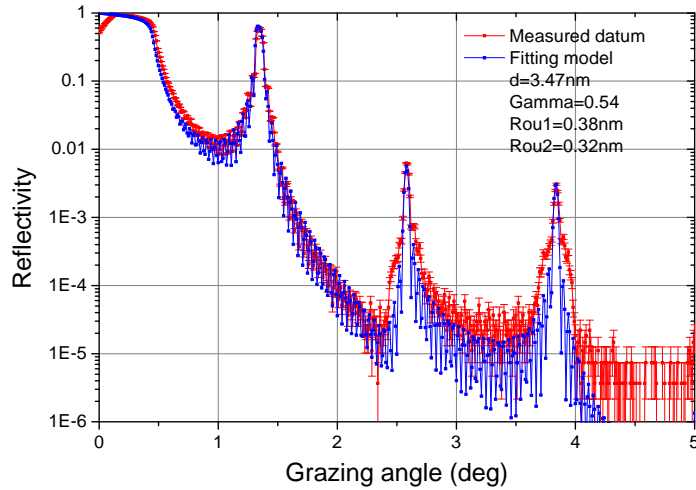


Fig. 4.17 Testing and fitting results of calibration samples.

There are 5 calibration samples. The individual thickness for each sample has been calculated from the fitting results and plotted against the corresponding spin speed of the sample holder.

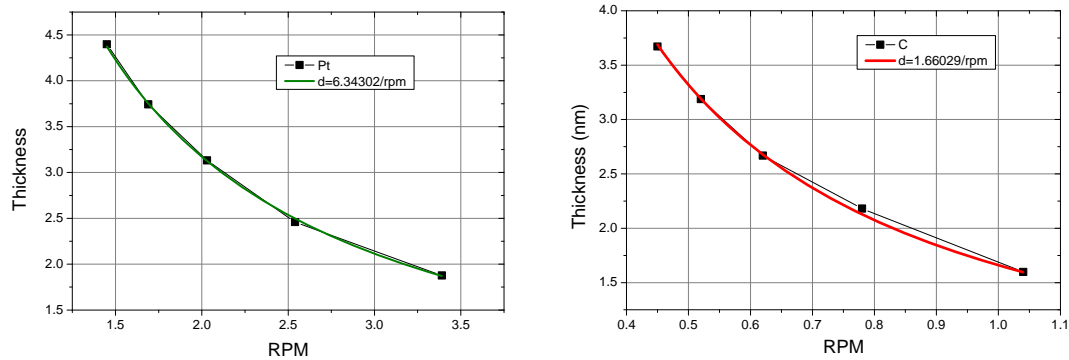


Fig. 4.18 Thickness of multilayer against rotation speed (R.P.M.). Curves are the best fit curve of reverse proportion. Standard deviation from the model is $\sim 3\%$.

After the calibration process, the designed structure shown in Fig.4.16 has been converted into the spin rate and input our sputter system. The sample has been finally fabricated. Though it is designed to provide flat response against energy, we firstly measure the angular response of the fabricated sample with a collimated X-ray beam of the Cu-K α line (8.05keV) to examine the structure in detail. The scan step is set at 0.01deg, which corresponds to ~ 0.3 keV of energy step at 0.28deg of grazing angle.

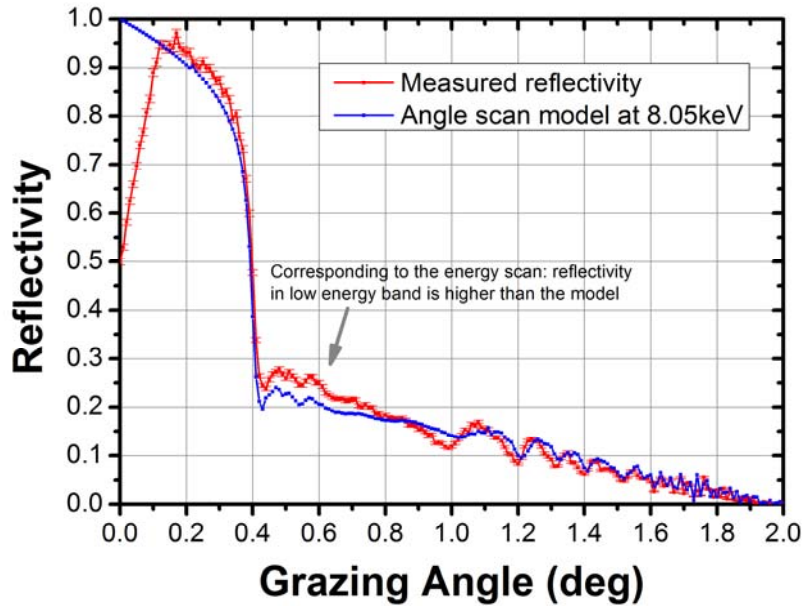


Fig. 4.19 Reflectivity v.s. grazing angle at 8.05keV. The red line is the measured profile and the blue line is the calculated profile.

In Fig. 4.19, the reflectivity at 8.05keV is plotted against the grazing angles. The reflectivity declines quickly with grazing angles, while the reflectivity profile against energy is designed with a flat top. This is because 8keV X-rays cannot reach to the bottom part of layers, which were designed for 50keV or more and are responsible for the reflectivity at larger angles in this case. The measured reflectivity profile is very close to the calculated profile in large grazing angles (>1deg). In the small grazing angle range (0.4deg~1.0deg), the measured reflectivity profile has a steeper slope than the model.

The energy response is also measured with continuum X-rays produced by an X-ray generator. The energy resolution ($\Delta E / E$ in 6% at 30keV) of the CdZnTe detector increases with the X-ray energy. Therefore, it is not appropriate to compare the measured reflectivity with the designed one directly. For this problem, we first measure three energy response profiles of the detector for different fluorescence lines. Cu-K α line at 8.05keV, Mo-K α line at 17.5keV and ^{241}Am line at 59.5keV are selected to get those profiles because these lines present the energy resolution of the detector within the target band of our supermirror. The pulse height distribution thus measured is fitted by Gaussian distribution and the energy resolution is derived by this fitting process (10.2% at 8.05keV, 7.5% at 17.5keV and 3.9% at 59.5keV). Assume that the square of the width of response profile is in proportion to the energy, i.e., $\Delta E^2 \propto E$, therefore the evolution of the detector response profile for incident energy can be obtained. Then, the expected profile has been calculated by the convolution of the designed response profile with the detector response to compare with the measured result, as is shown in following figure.

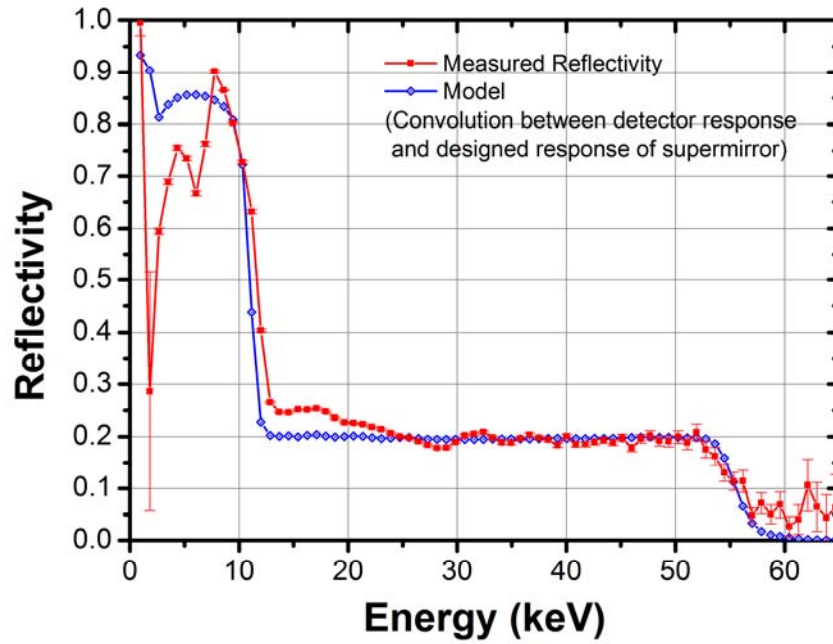


Fig. 4.20 Reflectivity against X-ray energy at 0.28deg grazing angle. The red line shows measured reflectivity. The blue line corresponds to the expected profile, which is the convolution of the designed profile with the detector response.

In the energy range higher than 30keV, the measured profile (red line) is almost the same as the calculated one (blue line). Below 30keV, however, the measured reflectivity profile is steeper than the model. It is with the same tendency as the deviation of angular scan result below 1.0deg shown in Fig. 4.19. This phenomenon will be discussed in following sections.

4.2.3 Side lobe suppressed multilayer

In the Chapter 2.3.2.2, I introduced a sidelobe suppressed multilayer, which can provide better reflectivity profile to reflect the X-rays. This structure can be fabricated by the fabrication process I established. The structure and corresponding response is shown in following figure firstly.

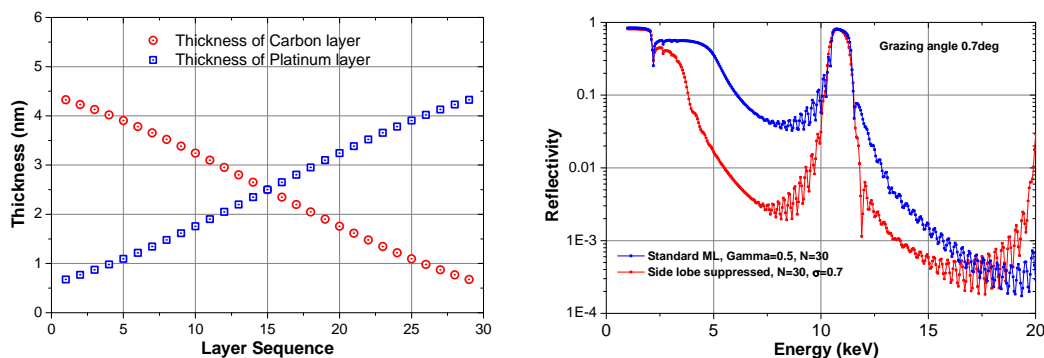


Fig. 4.21 Designed sidelobe suppressed multilayer and its corresponding response. In right panel, the blue line is corresponding to a standard multilayer, and the red line is the response of the structure shown in left panel.

A sample of the designed structure is fabricated by our DC magnetron system to demonstrate the feasibility of the designed structure. We also fabricate a standard multilayer with the same layer number and Bragg peak position for comparison. The multilayers are deposited on a float glass (30mm*70mm). The fabrication process is the same as that mentioned in our previous sections. The fabrication and testing result is shown in following figure.

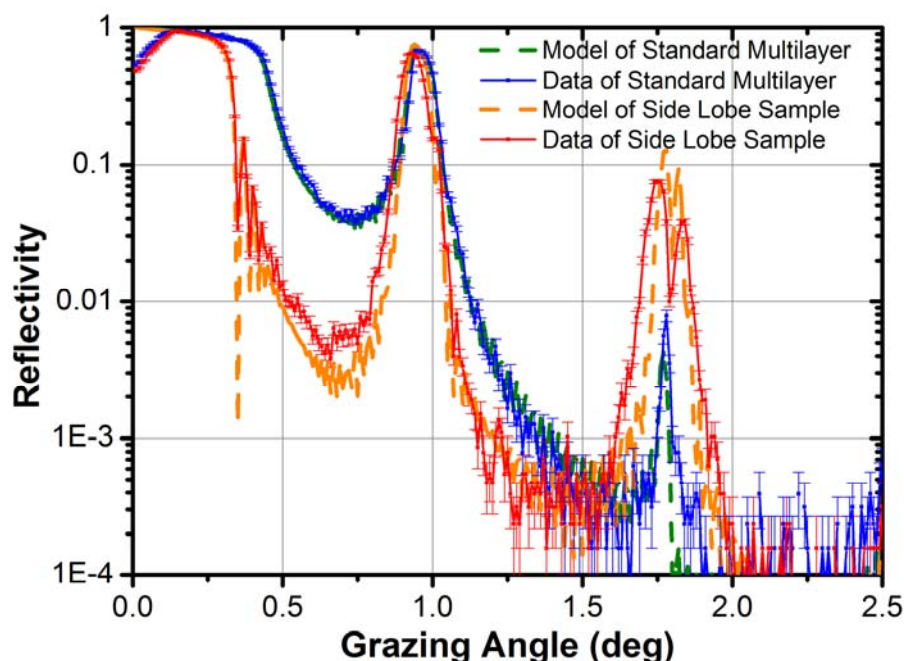


Fig. 4.22 Angular response of the side lobe suppressed sample (red line) and standard multilayer sample (blue line). The dot lines are corresponding to the calculated reflectivity profiles. The energy of incident X-ray is corresponding to Cu-K α line (8.05keV).

The angular response of the fabricated samples were measured with a collimated X-ray of the Cu-K α line (8.05keV). The scan step was set at 0.01deg, which was able to provide high resolution to look deep into the detail of the reflectivity profile. As is shown in Fig. 4.22, the red line shows the measured response profile, corresponding to the structure shown in Fig. 4.21. The orange dash line is the calculated reflectivity of this structure. The second order Bragg peak is slightly broadened due to the problem in thickness controlling. However, the angular region around the first order Bragg peak is important for the purpose of this paper. Comparing with the measured reflectivity of the standard multilayer (blue line), it can be concluded that the designing and fabrication is a success.

In summary, the side lobe response of the X-ray multilayer can be suppressed when the thickness ratio (γ) follows a designed distribution to provide a Gaussian window on the structure. The only parameter of the window function, i.e. σ , is determined by the lower limit of the layer thickness at the boundary of the structure. Such design can be realized by conventional deposition process, and have potential applications in future.

Chapter 5. Discussion and Summary

5.1 Summary of results

Supermirror is a layered structure of which the thickness distribution evolves for depth, which can reflect X-rays with a designate energy/angular response. It plays a crucial importance for hard X-ray telescope to enhance the effective area as well as ground-based applications. However, most of the supermirror design methods are based on empirical rules. Moreover, due to the fabrication difficulties, numerical design and fabrication of a hard X-ray supermirror with flat top and smooth response for telescope application has not been granted. To the questions of designing and fabrication of supermirrors, my doctoral thesis is presented into two parts.

1. Theoretical analysis of a block structure supermirror.

A block structure supermirror is a layered structure which consists of several periodic blocks with different d-spacing. It can provide a broad bandwidth energy response. This kind of the structure is easy to fabricate which is a great advantage from a practical point of view. However the design method is based on several empirical rules and has not been well explained. In order to understand X-ray propagation behavior in this structure, I granted my theoretical work. This work is based on Igor. V. Kozhenikov's theory which well explained X-ray propagation behavior in a depth-graded structure, but not applicable for block structures. In my work, I developed Igor's theory and applied it to analyze the X-ray propagation in a block structure. From my theoretical work, the oscillation of reflectivity profile can be well described. Moreover, a design rule can be concluded to provide a smooth reflectivity profile, which is a confirmation and development of empirical design rules. Based on my theory, I also invented a multilayer structure which can provide a better response profile (side lobe suppressed multilayer). It is an improvement for the performance of a periodic multilayer, which is attractive and promising for ground-based X-ray optics.

2. Experimental study of a supermirror structure with flat top and smooth response profile.

This kind of the supermirror may provide great advantages in energy/angular response for less oscillation and extremely flatness, as is shown in Fig. 3.28. However, such structure is difficult to design and fabricate due to its non-periodical thickness distribution. No work reported so far can successfully obtain a real supermirror structures for hard X-ray telescope applications. In order to improve the response of our telescopes, I established a design and fabrication process to obtain a non-periodic structure with perfect angular/energy response. Firstly, I established a numerical optimization method to adjust the thickness of the structure layer by layer. Such method may effectively smooth out the ripples and obtain an extremely flat response profile. From a practical point of view, in order to check the fabrication difficulties and the robustness of reflectivity for different boundary conditions, evaluation process has been established to confirm feasibility of designed structure. Secondly, I granted a fabrication process to fabricate such structures. By using the established process, I fabricated 3 samples. First one is a broad angular bandwidth supermirror with 30 layer pairs, ~20% flat top response within 1.0-1.5deg. Second one is a broad energy bandwidth supermirror with 123 layer pairs, ~20% flat top response within 10-55keV. The last one is a multilayer structure with side lobes suppressed energy/angular response. The fabricated samples are tested by X-ray reflectometers in the laboratories located in Nagoya University and ISAS. The testing results demonstrated that the fabricated samples successfully

provided designed response profiles, and the fabrication process is a success.

5.2 Re-construction of layered structure

Although the testing results demonstrated that the fabricated samples can successfully provide designed response, there are still some discrepancies which should be explained, as is shown in following figures.

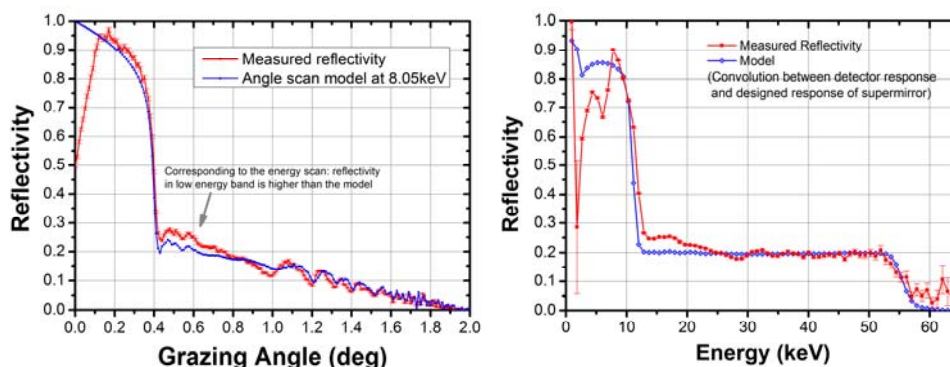


Fig. 5.1 Measured angular response and energy response and their corresponding fitting model of a fabricated supermirror.

As is shown in reflectivity profiles, the total reflection angle/energy of measured profiles is larger than the model. Moreover, the slope of the measured profiles is steeper than the model. Due to the fact that a thickness drift of all layer pairs was observed in many previous works and it may lead to similar phenomena, we firstly assume that it is cause by the thickness drift of all layer pairs. In order to prove this point of view, we calculate a reflectivity model of a thickness drifted structure and compare it with the measured profile.

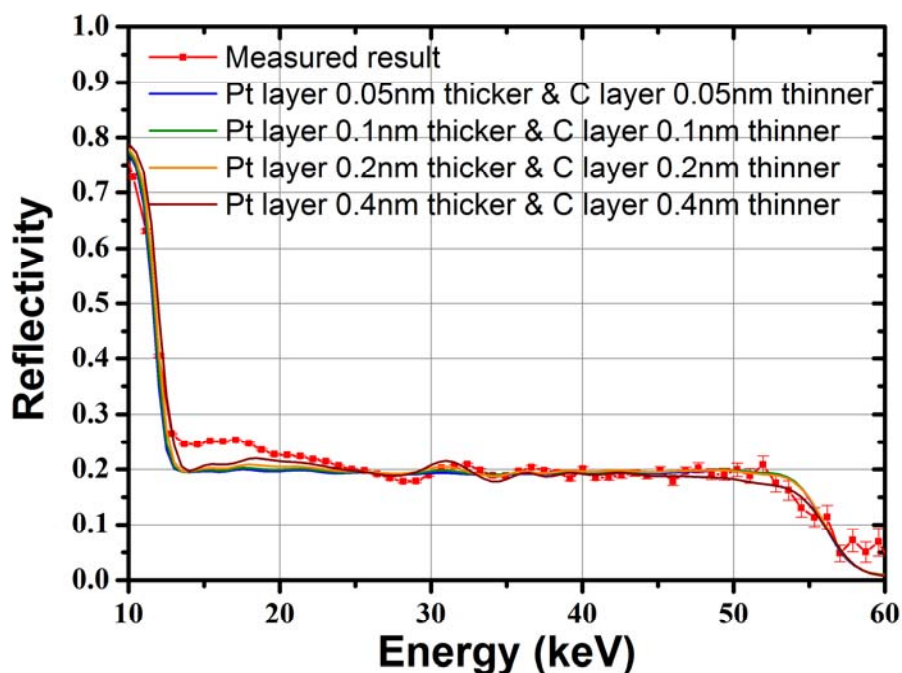


Fig. 5.2 Comparison between the measured energy response and calculated models (thickness drift model)

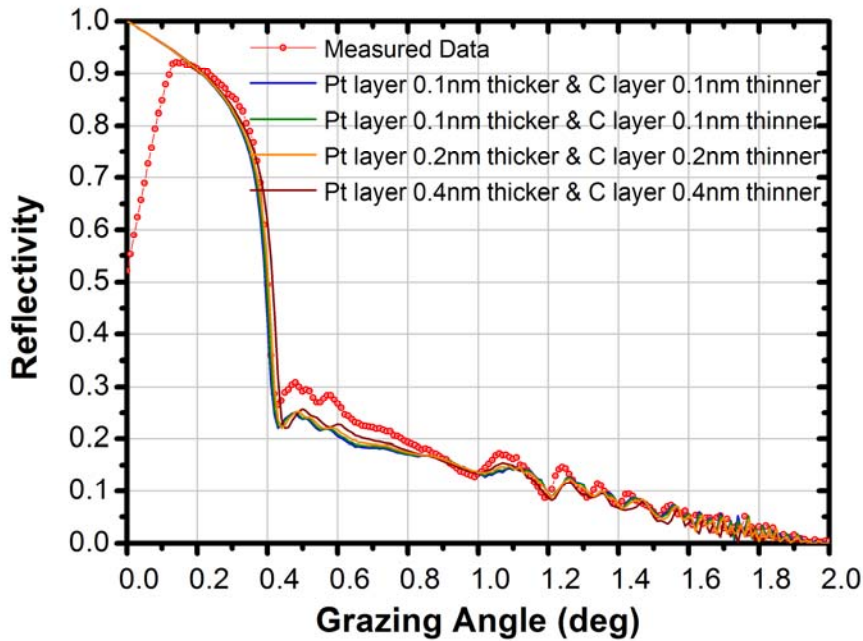


Fig. 4.3 Comparison between the measured angular response and calculated models (thickness drift model)

As are shown in figures above, we keep the d-spacing of layer pairs to keep the stop-band of reflectivity profile. Consequently when the thickness of Pt layer is thicker, that of C layer is thinner. The total reflection area of the models depend by shifting the thickness of Pt, which is closer to the measured one. However, the slope of the modified model at low energy/angular area is not steeper than that of original one. These results suggest that the thickness drift is not the reason we are looking for.

Another assumption is that the drift of Gamma may lead to a steeper slope of the model. Therefore we calculated the corresponding model and compare it with the measured profile in the same way.

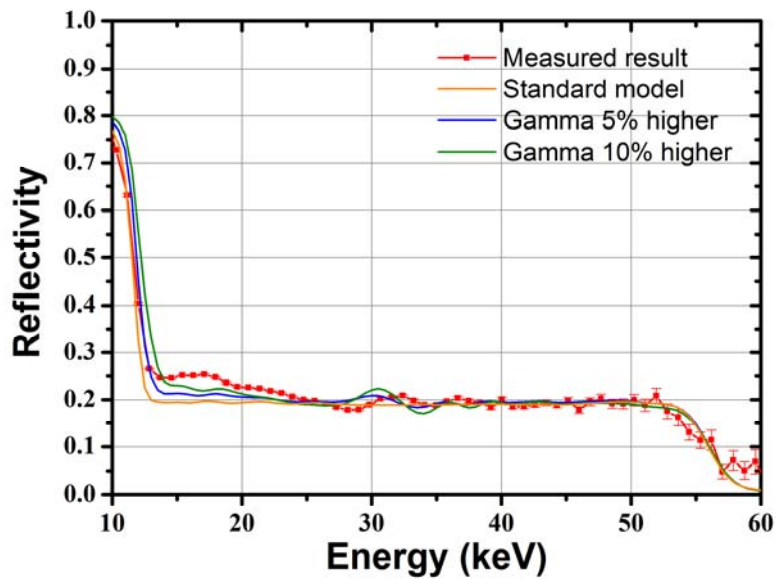


Fig. 5.4 Comparison between the measured energy response and calculated models (Gamma drift model)

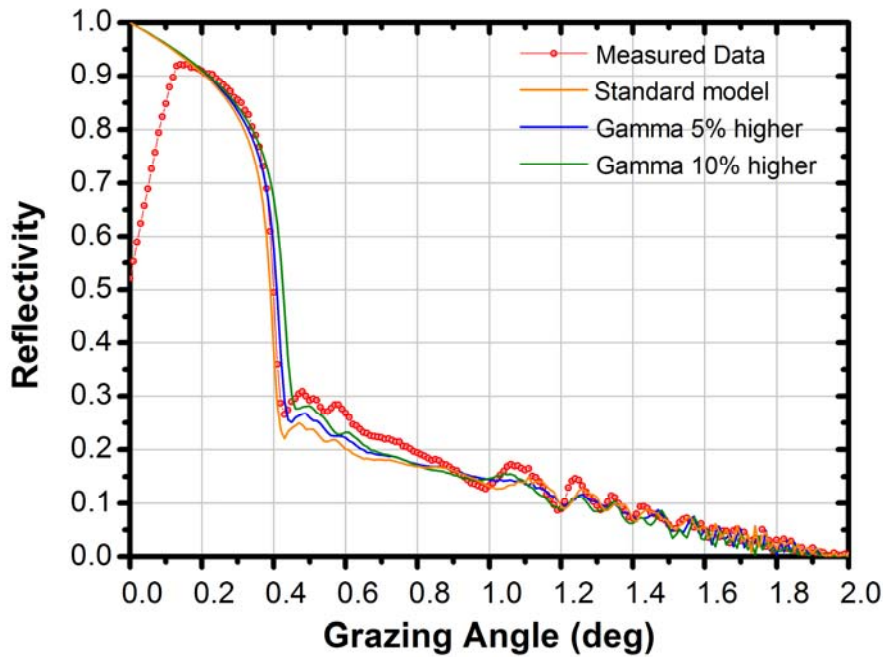


Fig. 5.5 Comparison between the measured angular response and calculated models (Gamma drift model)

The calculation results shown in the figures above still give a negative conclusion. The drift of Gamma is not the reason which leads to a steeper reflectivity profile at low energy/angular area. Then we begin to consider that the random thickness might be responsible for the higher slope of measured profile. In order to prove this idea, we try to use the optimization process to find a possible thickness distribution with the measures response profile. We set the designed structure as the initial structure and the measured reflectivity as the target reflectivity. When we only set the angular response as target reflectivity, the fitting result is shown in following figures.

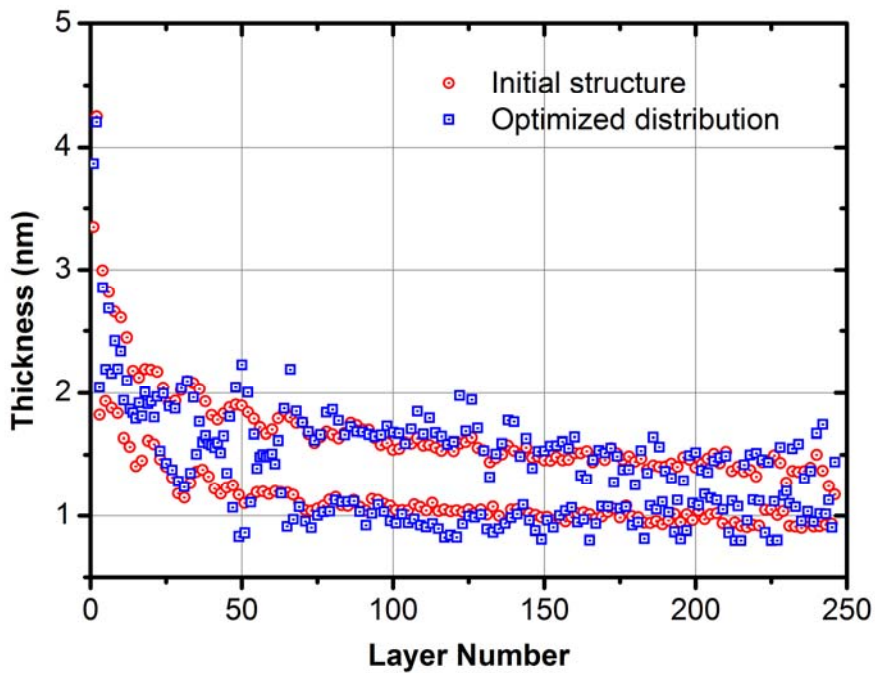


Fig. 5.6 Thickness distribution we found when we fit the angular response. The red line is the designed structure (in this case it is considered as initial structure)

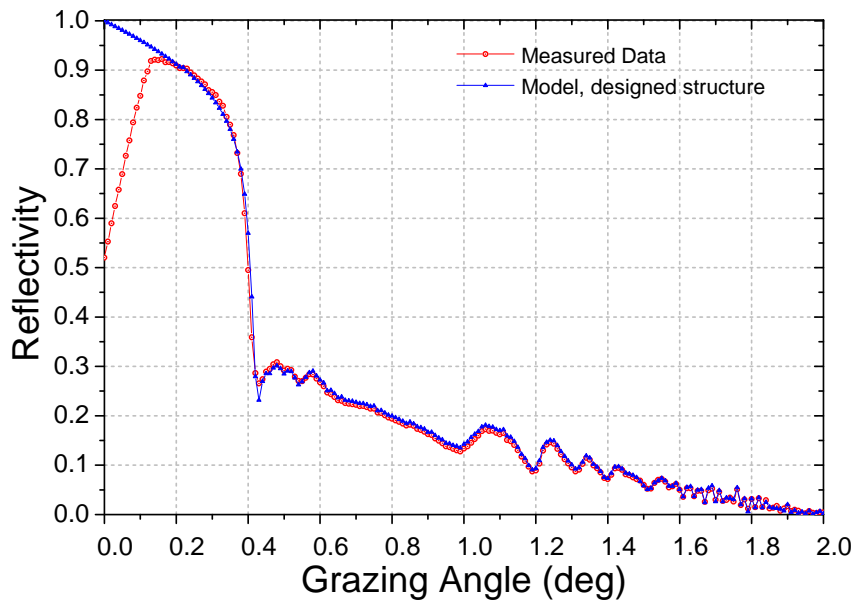


Fig. 5.7 Fitted angular reflectivity profile (blue line) and measured reflectivity (red line)

As is shown in Fig. 5.7, the angular response of the mode is very similar with the measured one. However, the fitted thickness distribution is very different from original one ($>0.1\text{nm}$ difference) as is shown in Fig. 5.6. It is caused by the fact that the structure for one response profile is usually not unique. If we calculate the energy response of this structure, the reflectivity of the model is far away from measured one. It confirmed this conclusion:

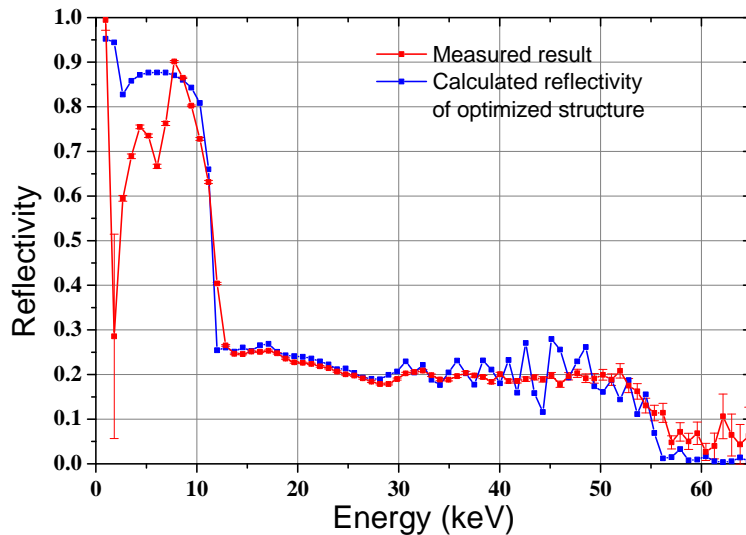


Fig. 5.8 Fitted energy reflectivity profile (blue line) and measured reflectivity (red line)

Obviously, the structure shown in Fig. 5.6 cannot provide correct energy response, thus it is not the correct structure we are looking for.

In order to find the correct structure, we move a further step to fit the reflectivity profile. We fit the angular and energy reflectivity simultaneously. The merit function is defined as, $MF=MF1+MF2$. The evolution of MF, the best fit of the structure and its corresponding response profiles are shown as follows.

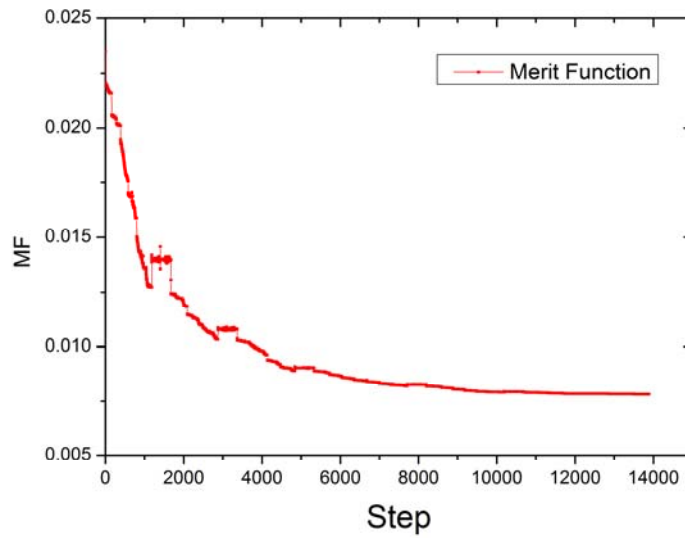


Fig. 5.9 Evolution of M.F. The fitting process was obtained by H-J algorithm.

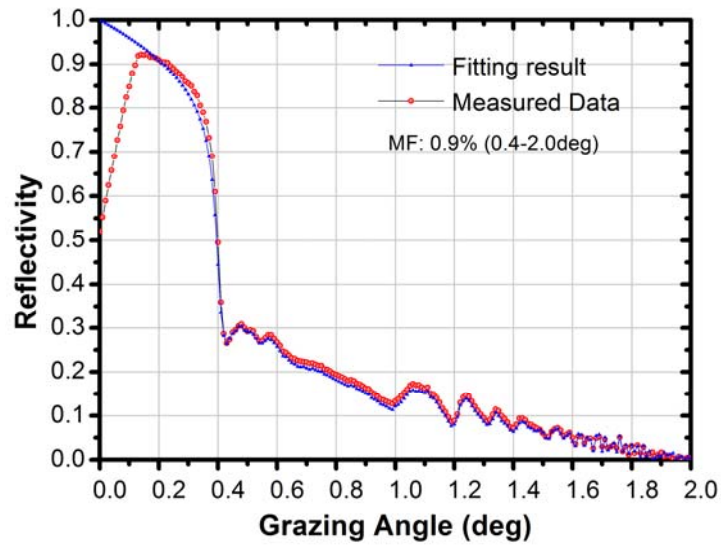


Fig. 5.10 Fitted angular response (blue line) and measured profile (red line).

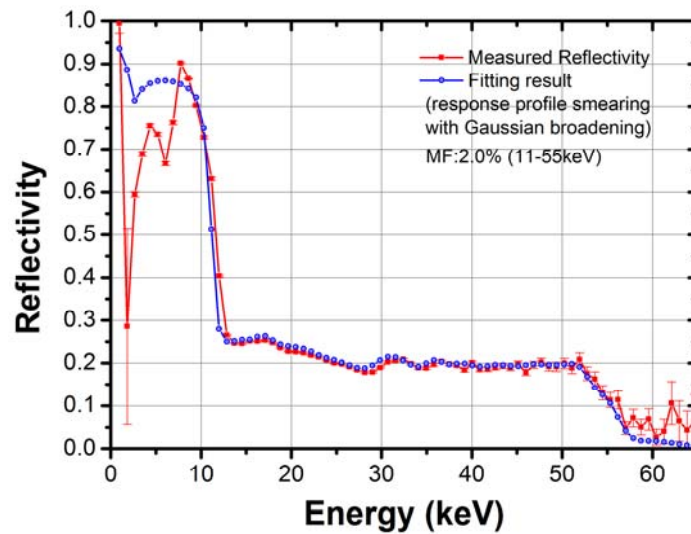


Fig. 5.11 Fitted energy response (blue line) and measured profile (red line).

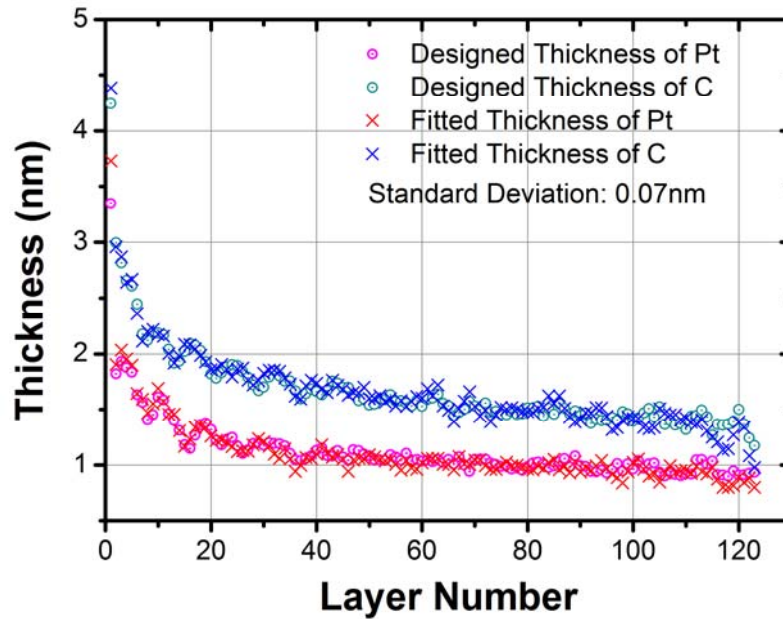


Fig. 5.13 Fitted thickness distribution (cross mark) and original design (open circle).

As is shown in figures above, we find a structure which has similar distribution of designed structure, and can provide reasonable energy and angular response profiles. We consider that the structure shown in Fig. 5.13 is close to real case, the random thickness error may lead to steeper slope of reflectivity profiles at low energy/angular range. This fitting process is promising and helpful for us to determine the fabricated structure in future.

However, the thickness is too large (0.07nm) to be consistent with the conclusion mentioned in previous sections (better than 0.02nm). Moreover, considering the fitting results shown in Fig. 5.10 and Fig. 5.11, there are some systematical errors between the measured profile and fitting model. Therefore we consider to introducing another parameter to help us to eliminate the systematical error, which will be introduced in next section.

5.3 Density issue

As has been introduced in first chapter, the density may significantly affect the optical constant, i.e., proportional to δ and β . A higher density of a metal is usually not realistic due to the strong atomic force between atoms. However when I fit the reflectivity profile, an interesting phenomenon happens. If I set the density of platinum higher than usual case, the fitting process became much faster (comparing with Fig. 5.9). The thickness deviation of the fitted layer from initial one was significant reduced.

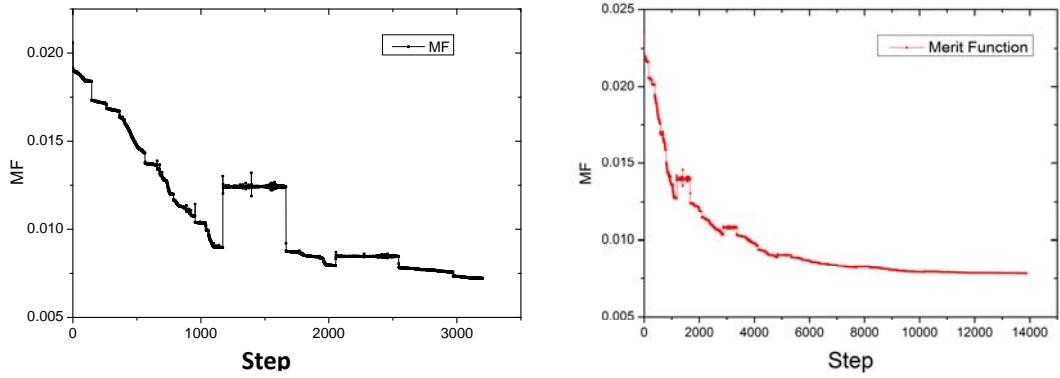


Fig. 5.14 M.F. comparison.

(L) Evolution of M.F. when density is set as 105%.

(R) Evolution of M.F. when density is set as 100%.

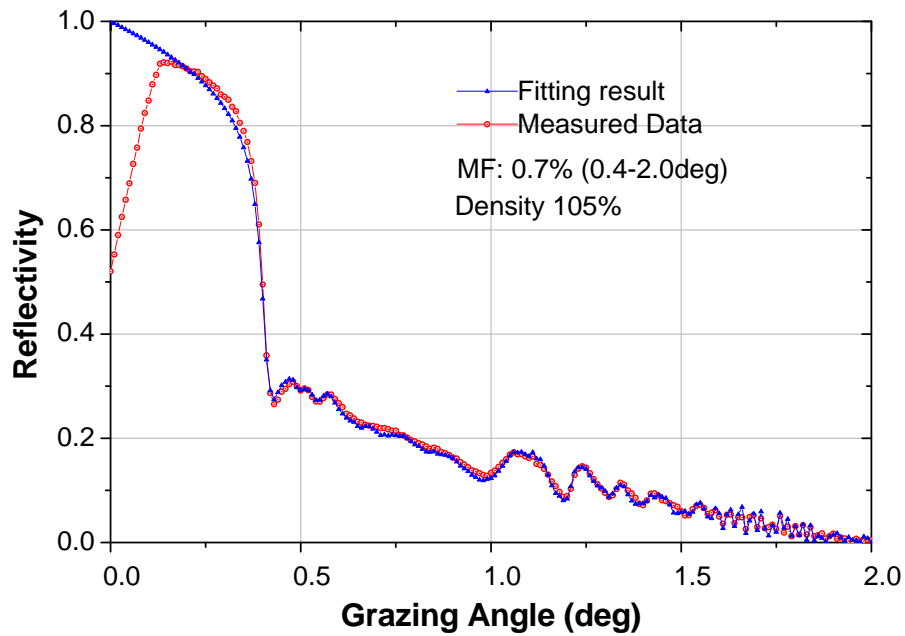


Fig. 5.15 Fitted angular response (blue line) and measured profile (red line)

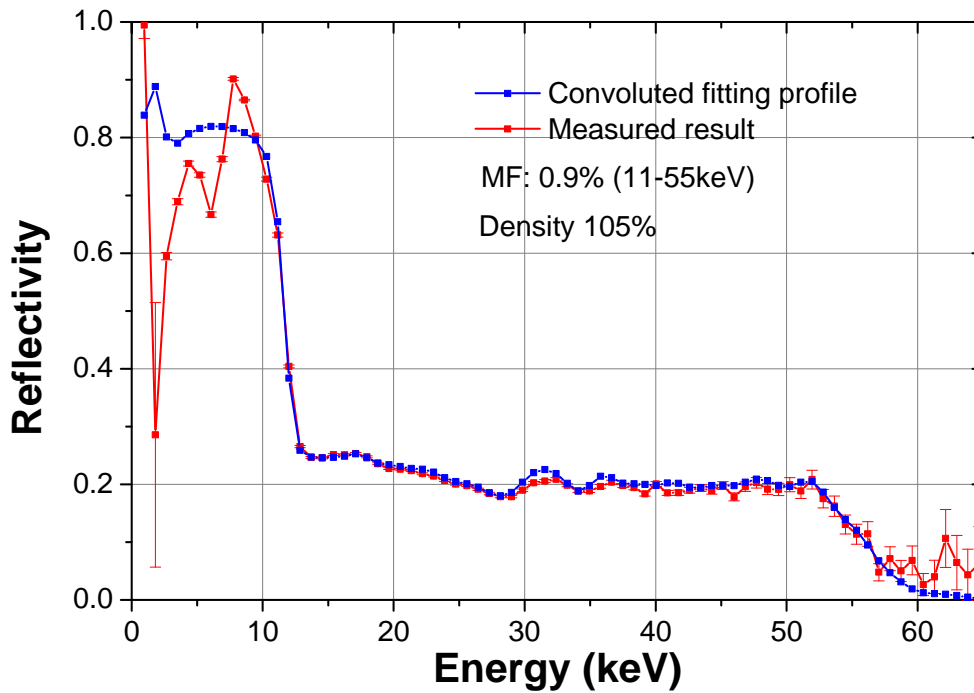


Fig. 5.16 Fitted energy response (blue line) and measured profile (red line)

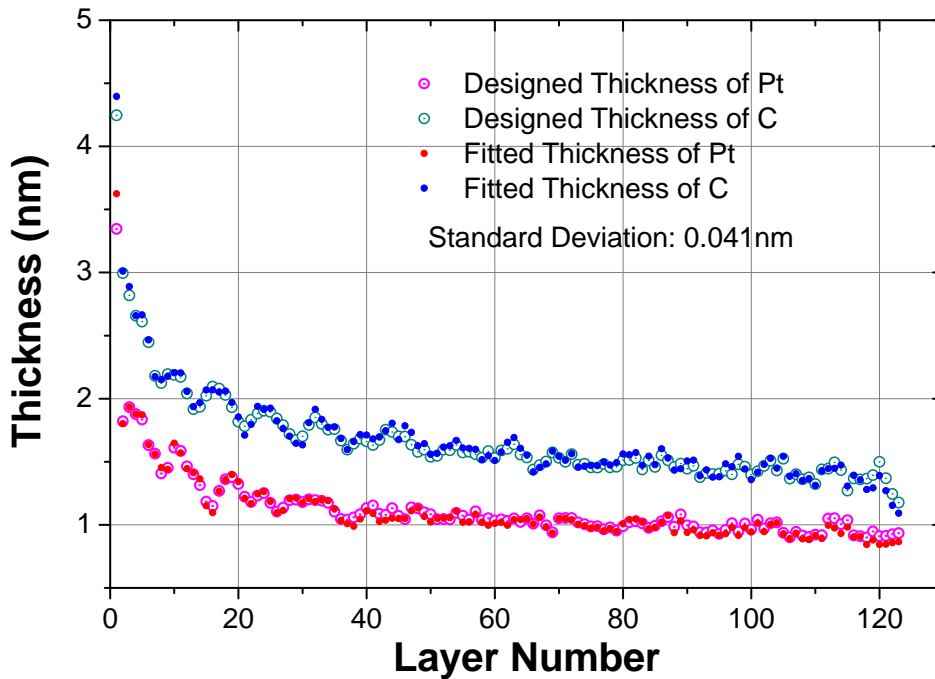


Fig. 5.17 Fitted thickness distribution and original distribution.

As is shown in Fig. 5.15, when the density of platinum is set 5% higher, the convergence rate of M.F. is 4-5times faster than that in Fig. 5.9. Moreover, the standard deviation of the fitted thickness from initial one can be reduced to 0.041nm, which is quite consistent with our conclusions. The standard deviation between the measured result and fitting model is significantly reduced (~0.5% lower). Moreover when I apply the same assumption to broad angular bandwidth supermirror, I also can find consistent result (comparing with Fig.4.14):

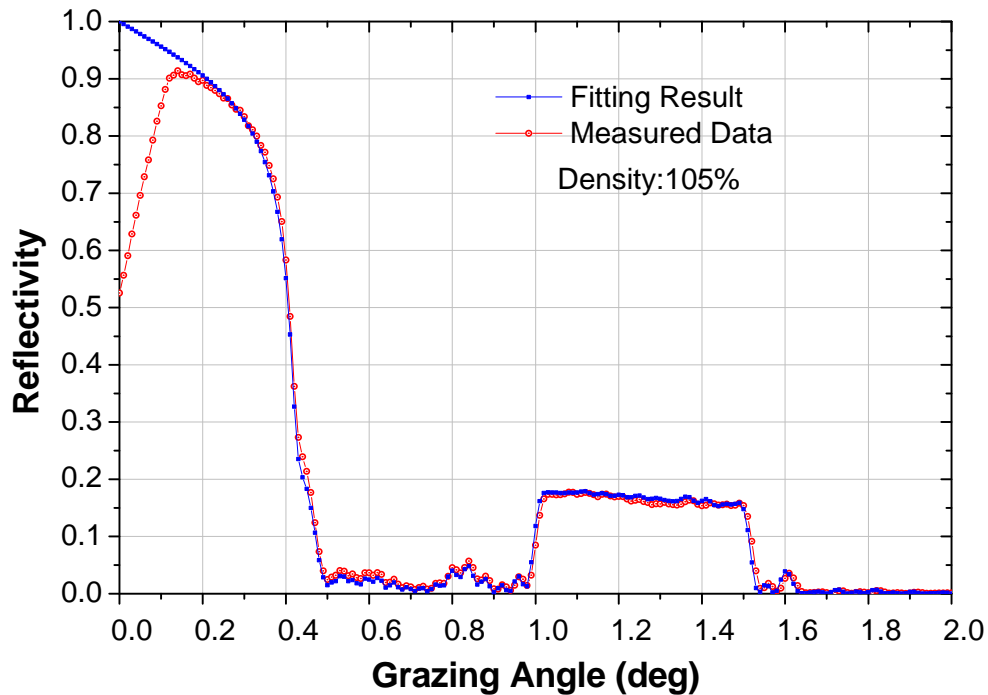


Fig. 5.18 Measured reflectivity profile (red line) and calculated reflectivity profile with 5% higher density assumption.

The total reflection region and decreasing tendency of calculated reflectivity from designed structure is consistent with the measured profile, which is better than the result shown in Fig. 4.14. If we take 5% higher density into account, it is possible to design and fabricate the supermirror structure to provide a really flat top response. Such further efforts of designing and fabrication are left for future works.

5.4 Future work

1. Theoretical analysis of the power law structure supermirror should be the next emphasis of theoretical work. Since it has been proved that the ripples of reflectivity profile of a block mirror is directly correlated with the Laplace transformation of the structure function, the power law mirror may also satisfy this principles. The empirical equation which describe power law structure should be thoroughly understood, which is essential for multilayer design.
2. As is described at the end of Chapter 2.2.2, the reflectivity of a supermirror at a specified energy point is proportional to the “equivalent layer number” times “reflectivity of one surface”. Although this conclusion based on “vector model” which may lead to a higher calculated reflectivity than real case, it is still very useful to evaluate the quality of multilayer structure. For example, the integral of “equivalent layer number” within target energy band gives us the information that “how many surfaces in the structure donate the reflectivity within designed band”. This concept may lead to a concept of “efficiency of the structure”, which allows us to compare the designed reflectivity profiles with different target.
3. Since the design and fabrication processes of non-periodic multilayer have been established, it can be applied to real missions.
4. Density issue is essential for the nature of very thin material (below 1nm). And it’s necessary

to be understood thoroughly for multilayer design in future (when design the structure, the abnormal density should be taken into account). My suggestion of the experiment is described as follows

- a) Fabricate single layer samples with different thicknesses (roughly, just change the spin speed of sample holder).
- b) Measure the angular reflectivity profile of each sample.
- c) Measure the layer thickness of each sample by using TEM.
- d) By using the measured thicknesses, the reflectivity profiles can be fitted for density and roughness. Then the fitted density of the materials for thicknesses can be understood

Acknowledgements

I would like to thank my advisor Prof. Kunieda Hideyo who taught and supported my research in these years. His wide mind, free style and encouraging attitude always spread positive energies and create excellent research conditions which helped me to merge into the research with great interesting. At the time when I fell into difficulties and adversities, his activities pushed me keeping on pace and overcoming hard situations. It was memorable that he became a patient English teacher when pointing out delicate mistake in my paper again and again. His attitude in research and skill in communication impressed me a lot and positively affect my research in future.

I would like to thank Dr. Keisuke Tamura who taught me skills for X-ray measurement. His abilities in adjusting the measurement system and his knowledge in data processing impressed me and ignite my interest in measurement processing.

I want to thank Prof. Zhanshan Wang in Tongji University who discussed with me in terms of the theoretical work and supported my ideas. His encouraging words and positive mind are memorable.

I would like to thank Prof. Matumoto Hironori and Prof. Ishibashi Kazunori who took care of my life, especially at the time of emergency and difficulty, their help and concern spread the feeling of warmth that let me understand that I'm not lonely.

Thanks for Dr. Takuya Miyazawa's help that let me understand how to fabricate multilayer structure. Thank Dr. Mori who always kindly answers my questions and encourages me.

I would like to Thank Mr. Yosuke Ishida. I never forget the first night I came to Japan in 2009, we discussed a lot until midnight. I never forget his help in my first year of doctoral course. He is a bright window for me to get information. Although he graduated one year after my enrollment, we kept in touch and good relations.

Finally, I would like to thank my family, my father and mother who gave me my life, raised me up and supported my study for 22years. I still remember when I'm a kid, my father brought me to his lab, gave me a small motor, and teach me why it can move with the electricity power. That ignite my curiosity kept my mind in research. They are always with me.

Appendices

A.1 Calculation of reflectivity

-- Matrix Algorithm (Abeles matrix formalism)

We firstly assume that the E-M wave propagating in a no-absorption material, i.e., no current. Secondly we assume E-M wave is time independent plane wave. Therefore, the expression of Electrical field and Magnetic field is

$$\vec{E} = \vec{E}_0 \exp i(\vec{k} \cdot \vec{r} - \omega t) \quad (6.1)$$

$$\vec{B} = \vec{B}_0 \exp i(\vec{k} \cdot \vec{r} - \omega t) \quad (6.2)$$

Here, assume that \vec{E}_0 is perpendicular to \vec{k}

Therefore, Maxwell's equations can be expressed as

$$\nabla \times \vec{E} = i\omega\mu\vec{H} \quad (6.3)$$

$$\nabla \times \vec{H} = -i\omega\varepsilon\vec{E} \quad (6.4)$$

$$\nabla \cdot \vec{E} = 0 \quad (6.5)$$

$$\nabla \cdot \vec{H} = 0 \quad (6.6)$$

Then, the Helmholtz equation can be derived as follows,

$$\begin{aligned} \nabla \times (\nabla \times \vec{E}) &= \nabla(\nabla \cdot \vec{E}) - \nabla^2 \vec{E} \\ \text{and } \nabla(\nabla \cdot \vec{E}) &= 0, \nabla \times (\nabla \times \vec{E}) = \omega^2 \mu \varepsilon \vec{E} \\ \text{so} \\ \nabla^2 \vec{E} + k^2 \vec{E} &= 0 \\ \text{and } k &= \omega \sqrt{\mu \varepsilon} \end{aligned} \quad (6.7)$$

From the results above, we eliminate ω in Eq. 6.3,

$$\vec{B} = -\frac{i}{\omega} \nabla \times \vec{E} = -\frac{i}{k} \sqrt{\mu \varepsilon} \nabla \times \vec{E} \quad (6.8)$$

From Eq. 6.1, we solve $\nabla \times \vec{E}$:

$$\begin{aligned}\nabla \times \vec{E} &= \nabla \times [\vec{E}_0 \exp i(\vec{k} \cdot \vec{r} - \omega t)] \\ &\text{and apply property} \\ \nabla \times (\varphi \vec{f}) &= (\nabla \varphi) \times \vec{f} + \varphi \nabla \times \vec{f} \\ \text{so}\end{aligned}\tag{6.9}$$

$$\begin{aligned}\nabla \times \vec{E} &= \nabla \exp i(\vec{k} \cdot \vec{r} - \omega t) \times \vec{E}_0 + \exp i(\vec{k} \cdot \vec{r} - \omega t) (\nabla \times \vec{E}_0) \\ &\text{since } E_0 \text{ is constant, } \nabla \times \vec{E}_0 = 0, \text{ then} \\ \nabla \times \vec{E} &= \nabla \exp i(\vec{k} \cdot \vec{r} - \omega t) \times \vec{E}_0 = i\vec{k} \times \vec{E}\end{aligned}$$

And apply Eq. 6.8,

$$\vec{B} = \sqrt{\mu\varepsilon} (\vec{s}_0 \times \vec{E})\tag{6.10}$$

Where \vec{s}_0 is a unit vector. The direction of this vector is the same as that of \vec{k} .

Therefore, \vec{B} , \vec{E} and \vec{n} are perpendicular with each other.

Eventually we get the ratio between \vec{E} and \vec{B} :

$$\left| \frac{\vec{E}}{\vec{B}} \right| = \frac{1}{\sqrt{\mu\varepsilon}} = v\tag{6.11}$$

Since we know $c = 1/\sqrt{\mu_0\varepsilon_0}$, therefore

$$\begin{aligned}\left| \frac{\vec{E}}{\vec{B}} \right| &= \frac{c}{n} = \frac{1}{n\sqrt{\mu_0\varepsilon_0}} \\ \text{and } n &= \sqrt{\frac{\mu\varepsilon}{\mu_0\varepsilon_0}}\end{aligned}\tag{6.12}$$

Usually, Eq. 6.12 is written as

$$\begin{aligned}\left| \frac{\vec{H}}{\vec{E}} \right| &= n \frac{\sqrt{\varepsilon_0\mu_0}}{\mu_r} \\ \text{and consider } \frac{\sqrt{\varepsilon_0\mu_0}}{\mu_r} &\text{ as a unit of refractive index } n.\end{aligned}\tag{6.13}$$

Therefore

$$\left| \frac{\vec{H}}{\vec{E}} \right| = n\tag{6.14}$$

Here, we calculated the ratio between magnetizing field and electric field of a E-M wave propagating in a no-absorption material. If the material is metal, looking at Eq. 6.18, the Eq. 6.14 is still correct and should be amended as follows,

$$\left| \frac{\vec{H}}{\vec{E}} \right| = \tilde{n} \quad (6.15)$$

Where \tilde{n} is the complex refractive index of the metal.

When we calculate the reflectivity of a surface, the boundary condition at the surface is critical.

Therefore, Eq. 6.15 is a “bridge” to calculate the reflectivity.

Now we consider the Fresnel equations. As is well known to all, the Fresnel equations derived from boundary condition.

Assume an E-M wave propagate through a surface with normal incident angle θ_0

For p-light, the magnetism field is parallel with the surface. We define the tangential component of magnetism field and electric filed are \vec{H}_t and \vec{E}_t , Therefore

$$\vec{H}_t = \vec{H}, \quad \vec{E}_t = \vec{E} \cos(\theta)$$

Because of the relationship from Eq. 6.15,

$$\vec{H} = \vec{H}_t = \tilde{n}(\vec{s}_0 \times \vec{E}) = \tilde{n}[\vec{s}_0 \times \vec{E}_t / \cos(\theta)] = \frac{\tilde{n}}{\cos(\theta)} (\vec{s}_0 \times \vec{E}_t)$$

Hence we define the equivalent optical constant for p-light:

$$\eta_p = \frac{\tilde{n}}{\cos(\theta)} \quad (6.16)$$

Similarly we can derive the equivalent optical constant for s-light

$$\eta_s = \tilde{n} \cos(\theta) \quad (6.17)$$

Eventually Fresnel's reflectivity expression can be simplified as follows,

$$r_p = \frac{\eta_{1p} - \eta_{2p}}{\eta_{1p} + \eta_{2p}} \quad (6.18)$$

$$r_s = \frac{\eta_{1s} - \eta_{2s}}{\eta_{1s} + \eta_{2s}} \quad (6.19)$$

Since Eq. 6.18 and Eq. 6.19 have the same form, in the following sections of this paper, the reflectivity of a single surface is written as

$$r = \frac{\eta_1 - \eta_2}{\eta_1 + \eta_2} \quad (6.20)$$

Now we consider a single layer reflection,

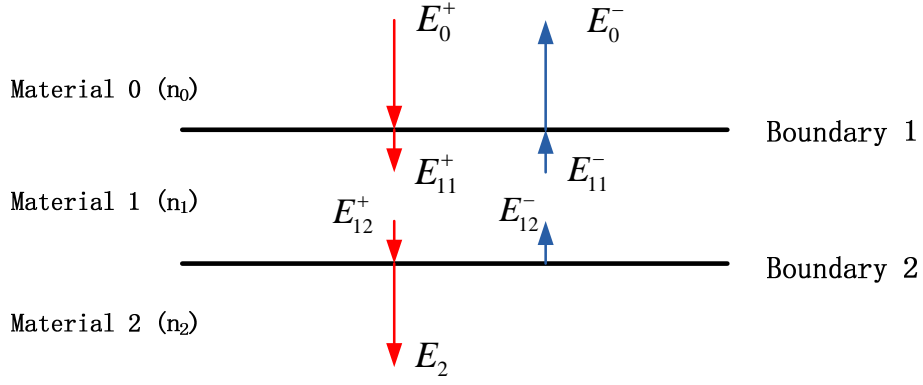


Fig. 6.1 Single layer reflection

As is shown in figure above, we assume the incident electric field and magnetism field are expressed as

$$E_0 = E_0^+ + E_0^- = E_{11}^+ + E_{11}^-$$

$$H_0 = H_0^+ + H_0^- = \eta_1 E_{11}^+ - \eta_1 E_{11}^-$$

In addition, we assume the thickness of the single layer is d , then the phase shift can be derived,

$$\delta_1 = \frac{2\pi}{\lambda} n_1 d_1 \cos(\theta_1)$$

$$E_{12}^+ = E_{11}^+ e^{-i\delta_1}, \quad E_{12}^- = E_{11}^- e^{i\delta_1}$$

Therefore

$$E_0 = E_{12}^+ e^{i\delta_1} + E_{12}^- e^{-i\delta_1}$$

$$H_0 = \eta_1 E_{12}^+ e^{i\delta_1} - \eta_1 E_{12}^- e^{-i\delta_1}$$

Hence, the equations above can be written as Matrix form:

$$\begin{bmatrix} E_0 \\ H_0 \end{bmatrix} = \begin{bmatrix} e^{i\delta_1} & e^{-i\delta_1} \\ \eta_1 e^{i\delta_1} & -\eta_1 e^{-i\delta_1} \end{bmatrix} \begin{bmatrix} E_{12}^+ \\ E_{12}^- \end{bmatrix} \quad (6.21)$$

In material 2, there is no upper ward E-M wave. Therefore the boundary condition can be derived

$$E_2 = E_{12}^+ + E_{12}^-$$

$$H_2 = \eta_1 E_{12}^+ - \eta_1 E_{12}^-$$

Thus,

$$E_{12}^+ = \frac{1}{2} E_2 + \frac{1}{2\eta_1} H_2$$

$$E_{12}^- = \frac{1}{2} E_2 - \frac{1}{2\eta_1} H_2$$

And it can also be written as Matrix form,

$$\begin{bmatrix} E_{12}^+ \\ E_{12}^- \end{bmatrix} = \begin{bmatrix} 1/2 & 1/2\eta_1 \\ 1/2 & -1/2\eta_1 \end{bmatrix} \begin{bmatrix} E_2 \\ H_2 \end{bmatrix} \quad (6.22)$$

Eventually, Eq. 6.21 and Eq. 6.22 are combined together, then

$$\begin{aligned} \begin{bmatrix} E_0 \\ H_0 \end{bmatrix} &= \begin{bmatrix} e^{i\delta_1} & e^{-i\delta_1} \\ \eta_1 e^{i\delta_1} & -\eta_1 e^{-i\delta_1} \end{bmatrix} \begin{bmatrix} 1/2 & 1/2\eta_1 \\ 1/2 & -1/2\eta_1 \end{bmatrix} \begin{bmatrix} E_2 \\ H_2 \end{bmatrix} \\ &= \begin{bmatrix} \cos \delta_1 & (i/\eta_1) \sin \delta_1 \\ i\eta_1 \sin \delta_1 & \cos \delta_1 \end{bmatrix} \begin{bmatrix} E_2 \\ H_2 \end{bmatrix} \end{aligned} \quad (6.23)$$

Here,

$$\begin{bmatrix} \cos \delta_1 & (i/\eta_1) \sin \delta_1 \\ i\eta_1 \sin \delta_1 & \cos \delta_1 \end{bmatrix}$$

Is defined as “Characteristic Matrix” of one layer.

Up to now, the major goal is to calculate the reflectivity of a single layer.

Looking at Fig. 6.1, there are boundary conditions,

$$\begin{aligned} H_0 &= \eta_0 E_0^+ - \eta_0 E_0^- \\ \eta_0 E_0 &= \eta_0 E_0^+ + \eta_0 E_0^- \end{aligned}$$

Hence,

$$r = \frac{E_0^-}{E_0^+} = \frac{\eta_0 - H_0 / E_0}{\eta_0 + H_0 / E_0} \quad (6.24)$$

In Eq. 6.24, H_0 / E_0 is defined as “Combination Admittance”. The Eq. 6.23 can be derived as

$$\begin{aligned} \begin{bmatrix} E_0 \\ H_0 \end{bmatrix} &= \begin{bmatrix} \cos \delta_1 & (i/\eta_1) \sin \delta_1 \\ i\eta_1 \sin \delta_1 & \cos \delta_1 \end{bmatrix} \begin{bmatrix} 1 \\ H_2 / E_2 \end{bmatrix} E_2 \\ &= \begin{bmatrix} \cos \delta_1 & (i/\eta_1) \sin \delta_1 \\ i\eta_1 \sin \delta_1 & \cos \delta_1 \end{bmatrix} \begin{bmatrix} 1 \\ \eta_2 \end{bmatrix} E_2 \end{aligned} \quad (6.25)$$

Here, E_2 is the electric field in substrate. η_2 is equivalent optical constant of substrate. Here we

define,

$$\begin{bmatrix} B \\ C \end{bmatrix} = \begin{bmatrix} \cos \delta_1 & (i/\eta_1) \sin \delta_1 \\ i\eta_1 \sin \delta_1 & \cos \delta_1 \end{bmatrix} \begin{bmatrix} 1 \\ \eta_2 \end{bmatrix} \quad (6.26)$$

The matrix $\begin{bmatrix} B \\ C \end{bmatrix}$ is called “the characteristic matrix of the combination of single layer and

substrate”. Then,

$$\begin{bmatrix} E_0 \\ H_0 \end{bmatrix} = \begin{bmatrix} B \cdot E_2 \\ C \cdot E_2 \end{bmatrix} \quad (6.27)$$

And eventually

$$\frac{H_0}{E_0} = \frac{C}{B}$$

The reflectivity expression Eq. 6.24 can be written as

$$r = \frac{\eta_0 - C/B}{\eta_0 + C/B}$$

where

$$\begin{bmatrix} B \\ C \end{bmatrix} = \begin{bmatrix} \cos \delta_1 & (i/\eta_1) \sin \delta_1 \\ i\eta_1 \sin \delta_1 & \cos \delta_1 \end{bmatrix} \begin{bmatrix} 1 \\ \eta_2 \end{bmatrix} \quad (6.28)$$

$$\delta_1 = \frac{2\pi}{\lambda} n_1 d_1 \cos(\theta_1)$$

for p-light, $\eta_1 = n_1 / \cos \theta_1$

for s-light, $\eta_1 = n_1 \cos \theta_1$

Until now, we derived the reflectivity of a single layer. Eq. 6.28 can be easily extended to calculate a multilayer structure. Here we assume an K-layer structure,

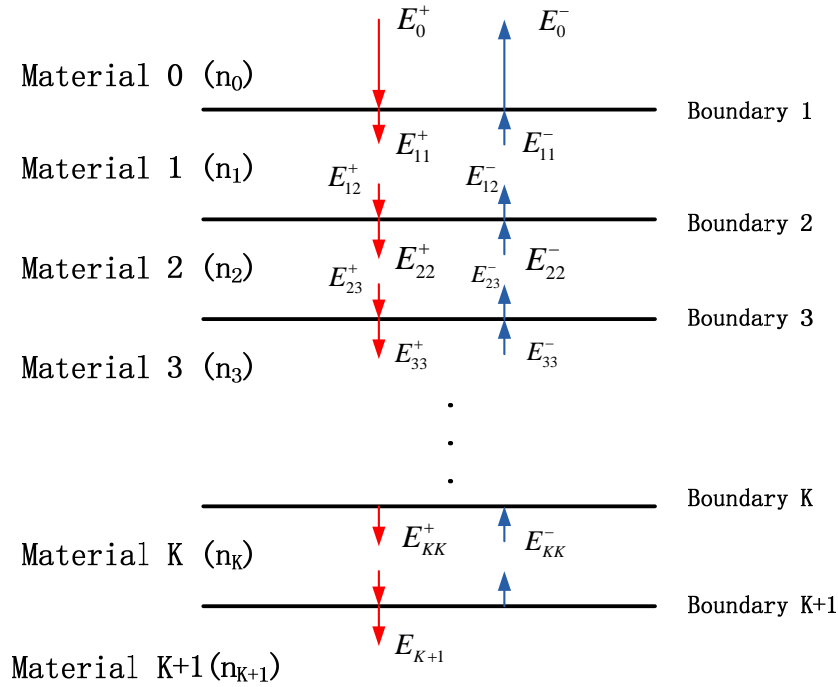


Fig. 6.2. Boundary conditions of a K-layer structure

In a K-layer structure, we apply Eq. 6.23.

For the first layer,

$$\begin{bmatrix} E_0 \\ H_0 \end{bmatrix} = \begin{bmatrix} \cos \delta_1 & (i/\eta_1) \sin \delta_1 \\ i\eta_1 \sin \delta_1 & \cos \delta_1 \end{bmatrix} \begin{bmatrix} E_{22} \\ H_{22} \end{bmatrix} \quad (6.29)$$

For the second layer,

$$\begin{bmatrix} E_{12} \\ H_{12} \end{bmatrix} = \begin{bmatrix} \cos \delta_1 & (i/\eta_1) \sin \delta_1 \\ i\eta_1 \sin \delta_1 & \cos \delta_1 \end{bmatrix} \begin{bmatrix} E_{33} \\ H_{33} \end{bmatrix} \quad (6.30)$$

And we apply the boundary condition on boundary 1:
$$\begin{bmatrix} E_{22} \\ H_{22} \end{bmatrix} = \begin{bmatrix} E_{12} \\ H_{12} \end{bmatrix}$$

Therefore we combine Eq. 6.29 and Eq. 6.30,

$$\begin{bmatrix} E_0 \\ H_0 \end{bmatrix} = \begin{bmatrix} \cos \delta_1 & (i/\eta_1) \sin \delta_1 \\ i\eta_1 \sin \delta_1 & \cos \delta_1 \end{bmatrix} \begin{bmatrix} \cos \delta_2 & (i/\eta_2) \sin \delta_2 \\ i\eta_2 \sin \delta_2 & \cos \delta_2 \end{bmatrix} \begin{bmatrix} E_{33} \\ H_{33} \end{bmatrix} \quad (6.31)$$

Hence, once we applied the recurrence relation to K+1 layer (substrate), then

$$\begin{bmatrix} E_0 \\ H_0 \end{bmatrix} = \left\{ \prod_{j=1}^K \begin{bmatrix} \cos \delta_j & (i/\eta_j) \sin \delta_j \\ i\eta_j \sin \delta_j & \cos \delta_j \end{bmatrix} \right\} \begin{bmatrix} E_{K+1} \\ H_{K+1} \end{bmatrix} \quad (6.32)$$

Similar with Eq. 6.26, the combined characteristic matrix of the multilayer can be expressed as

$$\begin{bmatrix} B \\ C \end{bmatrix} = \left\{ \prod_{j=1}^K \begin{bmatrix} \cos \delta_j & (i/\eta_j) \sin \delta_j \\ i\eta_j \sin \delta_j & \cos \delta_j \end{bmatrix} \right\} \begin{bmatrix} 1 \\ \eta_{K+1} \end{bmatrix} \quad (6.33)$$

Eventually the reflectivity of a K-layer structure can be derived as:

$$r = \frac{\eta_0 - C/B}{\eta_0 + C/B}$$

where

$$\begin{bmatrix} B \\ C \end{bmatrix} = \left\{ \prod_{j=1}^K \begin{bmatrix} \cos \delta_j & (i/\eta_j) \sin \delta_j \\ i\eta_j \sin \delta_j & \cos \delta_j \end{bmatrix} \right\} \begin{bmatrix} 1 \\ \eta_{K+1} \end{bmatrix} \quad (6.34)$$

$$\delta_j = \frac{2\pi}{\lambda} n_j d_j \cos(\theta_j)$$

for p-light, $\eta_j = n_j / \cos \theta_j$

for s-light, $\eta_j = n_j \cos \theta_j$

For an arbitrary multilayer structure with perfect surface, the reflectivity can be calculated easily by Eq. 6.34, by means of a computer algorithm.

Bibliography

1. M. C. Weisskopf et al., "Chandra x-ray observatory (CXO): overview," *proc. SPIE* 4012, 2-16 (2000)
2. F. Jansen et al., "XMM-Newton observatory," *A&A* 365, L1-L6 (2001).
3. A. F. Iyudin et al., "COMPTEL observations of 44Ti gamma-ray line emission from Cas A," *A&A* 284, L1-L4 (1994).
4. S. M. Owens et al., "Multilayer coated thin foil mirrors for InFOCuS," *Proc. SPIE* 4012, 619-625 (2000).
5. F. A. Harrison et al., "Development of the HEFT and NuSTAR focusing telescopes," *ExA* 20, 131-137 (2005).
6. H. Kunieda et al., "Hard X-ray Telescope to be onboard ASTRO-H," *Proc. SPIE* 7732 (2010)
7. K. D. Joensen et al., "Design of grazing-incidence multilayer supermirrors for hard x-ray reflectors," *Appl. Opt.* 34, 7935-7944 (1995).
8. I. V. Kozhevnikov et al., "Design of X-ray supermirrors," *Nucl. Instrum. Methods in Phys. Res. A* 460, 424-443 (2001).
9. X. Cheng et al., "Design of X-ray super-mirrors using simulated annealing algorithm," *Opt. Commun.* 265, 197-206 (2006).
10. C. Morawe et al., "Design and fabrication of depth-graded x-ray multilayers," *Nucl. Instrum. Methods in Phys. Res. A* 493, 189-198 (2002).
11. L.G. Parratt, "Surface Studies of Solids by Total Reflection of X-Rays" , *Phy. Rev.* 95, 359-369 (1954)
12. T. Okajima et al., "Characterization of the supermirror hard X-ray telescope for the InFOC μ S balloon experiment", *Appl. Opt.*, 41, 5417-5426 (2002).
13. H. Jiang et al., "Determination of the evolution of layer thickness errors and interfacial imperfections in ultrathin sputtered Cr/C multilayers using high-resolution transmission electron microscopy," *Opt. Express* 19 011815 (2011).
14. K. Yamashita et al., "New design concept of multilayer supermirrors for hard x-ray optics," *Proc. SPIE* 3766, 327 (1999)
15. K. Yamashita, "Development of Pt/C multilayer supermirrors for hard x-ray optics," *Nucl. Instrum. Methods in Phys. Res. A* 529, 59-62 (2004).
16. Y. Tawara et al., "Development of a multilayer supermirror for hard x-ray telescopes," *Proc. SPIE* 3444, 569-575 (1998).
17. I. V. Kozhevnikov and C. Montcalm, "Design of x-ray multilayer mirrors with maximal integral efficiency," *Nucl. Instrum. Methods in Phys. Res. A* 624, 192-202 (2010).
18. E. Spiller, "Characterization of multilayer coating by x-ray reflection," *Revue Phys. Appl* 23, 1687-1700 (1988)
19. A. R.S. Bahai et al., "Multi-Carrier Digital Communications theory and applications of OFDM" (Sprigner, 2004), Chap. 1.
20. D. L. Windt, "IMD—software for modeling the optical properties of multilayer films," *Comput. Phys* 12, 360-370 (1998)
21. H. Maury et al., "Design and fabrication of Supermirrors for (2-10keV) high resolution X-ray

- plasmas diagnostic imaging”, Nucl. Instrum. Methods in Phys. Res. A 621, 242-246 (2010)
22. F. Bridou et al., “Design and fabrication of X-ray non-periodic multilayer mirrors: Apodization and shaping of their spectral response”, Nucl. Instrum. Methods in Phys. Res. A 680, 69-74 (2012).
 23. K. Yamashita, “Multilayer X-ray optical systems for future X-ray astronomy missions,” in Workshop Proceedings: The Next Generation of X-Ray Observatories, M. J. Turner and M. G. Watson, eds., Special Report XRA97/02 (Leicester X-ray Astronomy Group, Leicester, UK, 1997), pp. 115-121
 24. Y. Tawara et al., “Multilayer supermirror coating for hard-x-ray telescope,” in Multilayer and Grazing Incidence X-Ray/EUV Optics III, R. B. Hoover and A. B. Walker, Jr., eds., Proc. SPIE 2805, 236-243 (1996)
 25. K. Tamura et al., “Development of balloon borne hard-x-ray telescopes using a multilayer supermirror,” In Grazing Incidence and Multilayer X-Ray Optical Systems, R. Hoover and A. B. Walker, eds., Proc. SPIE 3113, 285-292 (1997)
 26. X. S. Yang, “Introduction to Mathematical Optimization”, Introduction to Mathematical Optimization (2008).
 27. David Attwood, “Soft X-rays and Extreme Ultraviolet Radiation” (Cambridge University Press, 1999), Chap. 4.
 28. P. Pianetta and T. W. Barbee Jr., “Application of multilayers to synchrotron radiation” Nucl. Instrum. Methods in Phys. Res. A266, 441-446 (1988).
 29. W. H. Southwell and R. L. Hall, “Rugate filter sidelobe suppression using quintic and rugated quintic matching layers,” Appl. Opt. 28, 2949-2951 (1989).
 30. P. Baumeister, “Multilayer reflectors with suppressed higher-order reflectance peaks,” Appl. Opt. 31, 1568-1573 (1992).
 31. B. H. Ibrahim et al, “Correlation of sidelobe suppression between rugate filters and multilayer mirrors”, Appl. Opt. 46, 7776-7779 (2007).
 32. W. H. Southwell, “Gradient-index antireflection coatings”, Opt. Lett. 8, 584-586 (1983).
 33. K. Yamashita, “Development of Pt/C multilayer supermirrors for hard x-ray optics,” Nucl. Instrum. Methods in Phys. Res. A 529, 59-62 (2004).
 34. A. G. Michette, "Optical system for soft X-rays", Plenum Press, 1986
 35. M. Tolan, "X-ray scattering from soft-matter thin films", Springer, 1998
 36. G. W. Fraser, "X-ray detector in astronomy," Cambridge University Press, 1989
 37. C. Kittel, "Introduction to solid state physics, 7th ed," John Wiley & Sons, Inc., 1996.
 38. J. Tueller et al., "Internation focusing optics collaboration for uCrab sensitivity," Proposal for High Energy Astrophysics Supporting Research and Technology Program, 1996
 39. K. Yamashita, "Multilayer X-ray optics for future astronomy missions," UV and X-ray Spectroscopy of Astrophysical and Laboratory Plasma, Universal Academy Press, p.243 (1996)
 40. K. Yamashita, "Multilayer X-ray optics systems for future X-ray Astronomy missions", in workshop proceeding: The Next Generation of X-ray Observatories, p. 115(1997)
 41. T. T. Saha, "Image defects from surface and alignment errors in grazing incidence telescopes," Opt. Eng. 29(10), 1296(1990)
 42. B. Aschenbach, "X-ray Telescope", Rep. Prog. Phys. 48,579(1985)
 43. P. J. Serlemitsos et al., "The X-ray telescope on board ASCA", PASJ 47, 105(1995)

44. H. Kunidea et al., "Roughness Measurements of X-ray mirror surfaces", Jpn. J. Appl. Phys. 25, 1292 (1986)
45. P. Glenn and A. Slomba, "Derivation of requirements for surface quality and metrology instrumentation for AXAF/TMA," Proc. SPIE 597, 55 (1985)
46. N. J. Westergaard and P. L. Jensen, "A thin foil high throughput X-ray telescope", Proc.SPIE 597, 68(1985)
47. R. Petre and P. J. Serlemitsos, "Design and development of conical X-ray imaging mirrors," Proc. SPIE 640, 98 (1986)
48. M. P. Ulmer, "Replication of grazing incidence optics," Proc. SPIE 640, 149 (1986)
49. A. Furuzawa et al., "Replication of Multilayer supermirror," Proc. SPIE 3444, 576 (1998)
50. P. Gorenstein, "High throughput X-ray optics: an overview," Appl. Opt. 27, 1433 (1988)
51. P. A. J. de Korte, "High-throughput replica optics," Appl. Opt. 27, 1440 (1988)
52. Y. Soong et al., "Conical thin foil X-ray mirror fabrication via surface replication," Proc. SPIE 2515, 64 (1995)